NOTE TO USERS

Design and Optimization of a Silicon Base Micro Heat Exchanger

Siavash Sadri Lonbani

A Thesis

In

The Department

of

Mechanical and Industrial Engineering

Presented in Partial Fulfillment of the Requirements

For the Degree of Master of Applied Science (Mechanical Engineering) at

Concordia University

Montreal, Quebec, Canada

December 2004

Your file Votre référence
ISBN: 0-494-04428-4
Our file Notre référence
ISBN: 0-494-04428-4

ABSTRACT

Design and Optimization of a Silicon Base Micro Heat Exchanger

Siavash Sadri Lonbani

Micro heat exchangers are among the recent subjects of investigations aiming to achieve high heat dissipation rates from the heat sources such as compact electronic circuits and limit peak temperature levels. This work is an investigation directed towards the design and optimization of micro heat exchangers. Based on the optimization criteria established on scaled up models a micro-heat exchanger made of non-uniform array of silicon square micro pins is designed. The high thermal conductivity of silicon and its compatibility with electronic circuits makes it an excellent candidate used for designing and fabrication on these devices. Finite element models are built and calibrated against the experimental results obtained from tests on macro scale Aluminum specimens in contact with a heat source and facing flowing air at different velocities and different base temperatures in the wind tunnel. Further, the finite element models are extended to the micro level on various geometries and configurations of micro heat exchangers. It was found that square shape pins exhibit the higher heat transfer capability through the device in compare with circular pins in the case of similar hydraulic diameter. In addition for equal contact area between the solid and the fluid, smaller hydraulic diameter for the pins caused larger amount of heat transformation through the solid fluid border. Other important observation is that by using 45° attack angle with respect to the fluid direction, higher amount of heat is released by the pins. Also the amount of transferred thermal energy is increasing by diminishing the longitudinal distance between the pins in the direction of the flow.

ACKNOWLEDGMENT

I wish to express my deep sense of gratitude to my thesis supervisors Dr. Ion Stiharu from Mechanical and Industrial Department and Dr. Mojtaba Kahrizi from Electrical and Computer science Department for their valuable guidance, encouragement, precious time in giving me valuable ideas and an insight into this field of research. I am also extremely grateful to John Elliot, Danny Juras, Brad Luckhart, Robert Oliver and Jose Esteves who supported me in carrying out my experiments in the laboratory during the research.

It is an opportunity to thank my beloved parents Mr. Mortazagholi Sadri Lonbani and Mrs. Touran Zarghooni in providing me with honorable, emotional and monetary support from a long distance (my original country Iran) to do this research. My special thanks to my wife Mrs. Nogol Ghadarkhah who has supported me during the completion of the research. I also wish to express my sincere thanks to my brother and Sister Mr. Sohrab Sadri Lonbani and Mrs. Soheila Sadri Lonbani and friends who aroused me in this regard.

I am extremely thankful to all members and staff of Mechanical and Industrial Engineering Department and Electrical and Computer Science Department for giving me a chance to be a part in contributing to the technical world and supported me directly or indirectly to achieve this thesis and .

And thanks God who gave me patient and power to complete this project successfully.

TABLE OF CONTENTS

LIST OF FIGURES

LIST OF TABLES

CHAPTER 1

Introduction

In current electronic packaging designs of low power rated electronic components on printed circuit boards (PCB), specific considerations are given to achieve high heat dissipation rates and limit peak temperature levels. Also the desire to achieve greater computational power and speed led the designers to increase the circuit density and therefore, as a consequence, more heat will be generated from the electronic circuits. Conventional cooling methods may not be adequate to meet this challenge. This concern has generated motivation for research studies into the forced convection cooling of PCB electronic equipments using micro heat exchangers.

Another important application of micro heat exchangers can be found in vehicle manufacturing where complete combustion is necessary to reduce the high capacity emission of engines. The pre-evaporation of the fuel and the following injection of the vapor improve the homogenization of the fuel-air mixture and consequently, the quality of the combustion [1]. This process is started by super heating the walls of the fuel injection pipes (FIP) using evaporators in the initial point of FIP and helps to change the phase of the fuel from liquid to vapor. Then the fuel in vapor phase is injected to the following space and mixed with the injected air from outside. Clearly mixing two different material in the same phase (gas by gas or liquid by liquid) is much easier to get a homogenized mixture than mixing them with different phases such as liquid with gas.

The field of integrated micro-sensors and micro-actuators, called MEMS (Micro Electro Mechanical Systems), provides an important link between microelectronics and non-electronics applications, and a powerful enabling tool to realize such heat exchanger devices. By micro-fabrication techniques, designers are able to fabricate large number of small size, high precision channels in silicon or other suitable materials in extremely small volumes and thereby build extremely efficient and compact micro heat exchangers.

1.1. Literature Review

In one of the pioneering works, *Tuckerman and Pease (1981)* [4] showed that conventional liquid heat exchanger technology could be scaled down to micro scale dimensions and applied to silicon chips. They found that it is possible to extract 800 W/cm^2 from a chip with a $71\,^{\circ}C$ temperature rise. Since then, some scientists used the same techniques to remove larger amounts of heat from bigger chips with smaller temperature gradient and some scientists were working on solving this problem analytically and finding the approximate or exact equations for the temperature gradient both in the flowing liquid and the solid part of the micro heat exchangers with different fluids as coolants.

Vijay K. Samalam (1989) [5] presented the exact solutions for cooling silicon chips wherein water flows through micro-channels etched in the back of silicon wafers for fully developed hydrodynamic and thermal boundary layers in laminar flow. Some other assumptions were made to simplify the problem and evaluate analytically to obtain the optimum dimensions for the micro-channels.

Yutaka Asako and Mohammad Faghri (1989) [6] computed heat transfer characteristics for periodic fully developed region with the assumption of laminar flow through an array of heated square blocks deployed along one wall of a parallel plate channel. They have performed the calculations for a specific range of *Reynolds number* from 100 to 1000 and 0.7 for the *Prandtl number*. Their investigations were based on various geometries of heated area and for two different thermal conductivity ratios.

A. Weisberg, H. H. Bau and J. Zemel (1990) [7] presented theoretical investigation of heat transfer in devices with multiple channels employed for heat removal from uniformly distributed heat sources and solved numerically a conjugate heat transfer problem consisting of the evaluation of the temperature fields in both the solid substrate and the fluid for a fully developed thermal and hydrodynamic boundary conditions by the assumption of laminar flow. They concluded that under certain conditions for more simplification the solid can be assumed isothermal.

W. Bier, W. Keller, G. Linder, D. Seidel and K. Schubert (1990) [8] reported a mechanical method for manufacturing micro-structural bodies, which is based on shaping of foils by precision cutting with micro-tools to build compact cross-flow micro heat exchangers made of aluminum alloys, copper, stainless steel and titanium. Also they have used electron welding and laser welding as joining techniques for the micro heat exchangers. They have been able to transfer 20 kW/cm^3 thermal power at mean logarithmic differential temperature of about 60 K, which is equal to the difference between the temperature of the hot fluid and cold fluid at the entrance of mentioned product multiplied by a constant factor, in a cross-flow micro heat exchanger with water

to water as fluids for the maximum flow rate of approximately 12.5 l/min. This corresponds to volumetric heat transfer coefficient of more than 300 MW/m³.K.

J. H. Wang, H. Y. Yeh and R. J. Shyu (1991) [9] reported experimental results of thermal performance and hydraulic resistance of two micro heat exchangers in a hot/cold water test loop. They measured volumetric heat transfer coefficients of 7 MW/m³.K and concluded that the channel size and wall material have strong influence on the heat transfer capability of a micro heat exchanger.

A. Bejan and A. M. Morega (1993) [10] reported an optimal geometry of an array of fins that minimizes the thermal resistance between the substrate and the flow forced through the fins by assuming laminar flow. They considered two types of fins for their analytical work (Round pin fin and staggered parallel-plate fins). They concluded that the minimum thermal resistance of plate-fin array is approximately half of the minimum thermal resistance of heat sinks with continuous fins and fully developed laminar flow in the channels, *which indicates the existence of an optimal pin fin array for maximum thermal conductance.*

In 1994, *C. R. Fredrich and S. D. Kang* [11] reported a mechanical method for manufacturing micro-structural bodies, which is based on machining of thin metal foils with specially contoured diamond cutting tools. Vacuum diffusion process was used to bond the plates together to form a cross-flow, plate-type micro heat exchanger. This micro heat exchanger provided a volumetric heat transfer of nearly 45 MW/m³.K, which is nearly 20 times higher than the conventional heat exchangers.

X. Yin and H. H. Bau (1995) [12], evaluated the performance of micro heat exchangers fabricated in silicon wafers consisting of pin arrays and straight channels (theoretically using a three dimensional numerical simulations). They considered liquid nitrogen as the coolant liquid and found the results for both developed and periodic flows, which are subjected to a given pressure drop and volume, and finally concluded that in fully developed flow:

- Temperature inside each pin is almost uniform and is much higher than that in the flowing liquid.
- The heated surface temperature normal to the flow direction is almost uniform.
- For deep channels, the uniform channels have the lowest cross-sectional resistance.
- For shallow channels, thermal resistance of a channel with spaced pins is lower than the one with the straight channel.
- It may be desirable to use a non-uniform pin arrangement such as the cross sectional resistance increases by increasing the density of pins throughout the channel to minimize thermal resistance of heat exchanger.

Nelson Kuan (1996) [13] designed a micro heat exchanger and fabricated it on a silicon wafer. His main idea was to minimize heat interaction with the ambient and minimize the thermal resistance between the heat source and the heat exchanger. Finally he removed 50 W/cm^2 of heat with an average of 7.5°C from the heat source and concluded that experimental results were in reasonable agreement with the theoretical predictions and a better performance can be obtained through optimized geometry.

B. V. Antohe, J. L. Lage, D. C. Price and R. M. Weber (1996) [14], reported numerical simulation results for a micro heat exchanger using porous aluminum layers, which were compressed together to improve the heat transfer at the coolant/solid interface and to provide more uniform cooling. Results indicate that the proposed design is capable of achieving a maximum temperature difference of 2°C using polyalphaolephin as coolant.

T. Igarashi [19]-[24] carried out experimental investigations on the characteristics of the flow around rectangular cylinders for different ratios of 1 to 4 between the two edges of the rectangular section cylinders and found distinct changes of flow patterns at two critical ratios of 0.67 and 2.8. He also measured local heat transfer coefficient distribution around square and rectangular cylinders using thermocouples and found that heat transfer coefficients are closely related to the drag coefficients.

Also *S. Y. Yoo, Jong. H. Park, C. H. Chung and M. K. Chung* [19] have recently carried out investigations by using naphthalene sublimation technique to measure detailed local mass transfer rates from a rectangular cylinder by changing the inlet air velocity. Then the measured mass transfer data are converted to their counter part of heat transfer process by applying heat/mass transfer analogy. They compared the mass transfer data with those of heat transfer, which obtained by T. Igarashi [22] with the same geometries and flow conditions. As a result they found that:

- Heat and mass transfer are in good agreement with each other, but local rates of mass transfer are much higher than those of heat transfer when the separated flow reattaches to the side face of the cylinder.

- The variation trends of the heat transfer coefficient values are similar to mass transfer coefficient regardless of width and height ratio, but mass transfer coefficient are somewhat lower than those of heat transfer on the side and rear faces.
- Heat transfer coefficients in the constant heat flux boundary condition are higher than those in the constant temperature boundary condition [25].

A. Zukauskas and R. Ulinkas [30] reported lots of experimental investigations in concern with heat transfer from the banks of circular tubes in cross flow with different fluids for both staggered and in-line banks and they found out that:

- The amount of transferred heat from the tubes in the first row of the bank is lower than the inner rows. The cause of this phenomenon is that at low Re numbers when the laminar flow is hitting the first row, after which it becomes slightly turbulent and the heat transfer increases in the subsequent banks.
- For a specific tube arrangement in in-line banks, heat transfer of an inner row at low Re numbers is even less than heat transfer in the first row in view of shadowing phenomena.
- Starting with the third row of the banks, heat transfer in the following rows stabilizes and practically coincides with the heat transfer of the third row.
- Heat transfer of tubes in an inner row, as a rule, increases with decreasing longitudinal pitch.
- In-line banks of tubes with small longitudinal pitch are an exception, where a decrease in pitch can lead to a decrease in heat transfer.

- In steady state flow, heat transfer of a tube in a bank is significantly greater than heat transfer of a single tube. This is related to the small thickness of boundary layer on the surface of a tube in the bank and to the elevated turbulence of flow in the intertubular spacing.
- The staggered banks of tubes are more efficient in compare with the in-line banks of tubes because of relatively higher mean heat transfer coefficient as illustrated in figure 1-1.
- The staggered banks of tubes are recommended for design options because of flexibility changing the longitudinal pitch design.

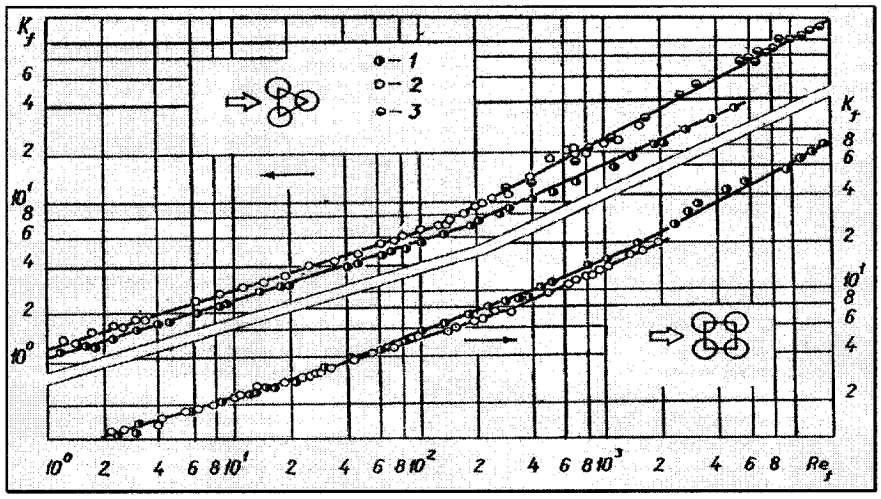

Figure 1-1.Mean heat transfer coefficient of tubes in different rows of staggered and in-line banks, 1) First row, 2) Forth row, 3) Third row. [30]

Christophe Marques and Kevin W. Kelly [46] reported heat transfer and pressure loss experimental results for a flat parallel plate pin fin *micro* heat exchanger with a staggered pin fin array, with height-to-diameter ratios of 1.0, with spacing-to-diameter ratios of 2.5 and for Reynolds numbers (based on the hydraulic diameter of the channel) from 4000 to 20,000. They compared the results with studies of larger scale, but geometrically similar,

pin fin heat exchangers. Also they did further research to describe an analytic model, which used the empirical results from the pin fin heat exchanger experiments to predict a cooling effectiveness exceeding 0.82 in a gas turbine blade cooling application and finally they demonstrated the feasibility of fabricating a relatively complex micro heat exchanger on a simple airfoil (a cylinder).

1.2. Scope of Thesis

In this work, the fundamental issues related to design of micro heat exchangers are presented. Based on these findings, a micro-heat exchanger by distributed non-uniform array of micro silicon pins is designed.

Silicon is the primary substrate material used for fabricating integrated circuits. The high thermal conductivity of silicon, good mechanical properties and its compatibility with printed circuit boards (PCB) makes this material an excellent candidate used for designing and fabrication of these devices.

The coolant fluid that was used in this design is air. Because fabrication and testing the micro scale models is very tedious and difficult to accomplish and costs a lot in comparison with ordinary macro models, Finite Element Modeling (FEM) is used to simulate the size and shape of silicon pins on a silicon surface. All the simulations have been made in the ANSYS software setting. The advantages of using ANSYS for engineers are:

- It is easy to use (user friendly).

- Ability to do more than one type of simulation on the same model (for example: Thermal and structural).

In the very beginning, it was investigated that by decreasing the size and scale of the pins how the efficiency of transferred thermal energy from a surface will change. As a result it was found that, when the same total contact area with the flowing fluid is applied, the rate of transferred heat from a pined surface with a specific area is higher when the pins are getting smaller in size. In these simulations, a 25.4mm×25.4mm pined silicon based surface have been modeled in the ANSYS software and specific boundary conditions have been applied on the contact surfaces of the model with the flowing fluid with the velocity of 10 m/s. Then the rate of transferred heat, which is absorbed by the flowing fluid through the pin, has been estimated.

On the next step the smaller pins by the same total contact area have been modeled with the same flowing fluid and the same boundary conditions. The simulations have been applied for different ratios of ***pin height/the base thickness*** (from 1 to 7) and the quantity of pins have been increased from 1 to 9 on the same base.

Results confirmed that decreasing the size of the pins on a surface with any specific solid-fluid contact area, increases the amount of transferred thermal energy. In addition it was found that the optimum ratios for the ***height of the pin/ thickness of the base*** **(L/t)** to get the highest amount of transferred thermal energy are 4 and 6. This was a good point to start reducing the size of pins to micro scales and design an efficient surface to transfer higher amount of thermal energy from the base through the pins to the flowing fluid.

The rationale of this work focused on the following issues:

- Low scale thermal measurements are very difficult to carry out. Because fabrication of micro pined surfaces is costly and takes long time fabrication process as well as a lot of limitations in detecting temperature distribution for the experimental part.
- To avoid these kinds of interactions it was decided to build realistic larger scale Aluminum models and perform those experiments on them.
- Finite element models were created and fine tuned (calibrated) to match the simulation results with those of the experiments.
- After verification of the relations between the experimental and simulation results, the models were extrapolated to the small scales and the results are compared.
- Further, the simulations have been carried out with the objective of designing and optimizing a micro heat exchanger.

This type of micro heat exchanger could be used in microelectronics applications and is compatible with the silicon based devices to transfer any thermal energy from one source to the other one.

1.3. Layout of Thesis

According to the above plan, the thesis is organized as the following chapters:

Chapter 2 covers the basic theories about the field of heat exchangers and heat transfer and present different categories of heat exchangers. In addition the basic Finite Element Method analysis and modeling are described in this chapter and finally details of experimental process are presented.

Chapter 3 shows some of the experimental and simulation results and compares them together to validate a perfect and exact method of simulation for design procedure.

Chapter 4 extends the simulations of Finite Element Method using ANSYS software to design and optimize a micro heat exchanger and then feasibility of practical fabrication methods on Micro Electro Mechanical Systems (MEMS) is investigated to fabricate these types of micro structures.

Chapter 5 summarizes the conclusions and suggested future works.

CHAPTER 2

Basic Theories of Heat Transfer, Mathematical and Experimental Modeling Procedures

2.1. Heat Exchangers

Heat exchangers are devices that provide the flow of thermal energy between two or more materials at different temperatures. Heat exchangers are used in a large variety of applications. These include power production; process; chemical and food industries; electronics; environmental engineering; waste heat recovery; manufacturing industry; air-conditioning; refrigeration and space applications.

Heat exchangers may be classified according to the following main criteria [2]:

1. Recuperator/Regenerator
2. Transfer processes: direct contact and indirect contact
3. Geometry: tubes, plates and extended surfaces
4. Heat transfer mechanisms: Single-phase and two-phase
5. Flow arrangements: Parallel-flows, Counter-flows, Cross-flows

All of the above criteria are illustrated in figure 2-1.

2.1.1. Recuperator/Regenerator

The above type of heat exchanger is called *recuperator* because a hot stream recovers (recuperates) some of the heat from another stream (figure 2-1a). In these heat exchangers, heat transfer occurs through a separating wall or through the interface

between the streams as in the case of the direct contact type of heat exchangers (figure 2-1c).

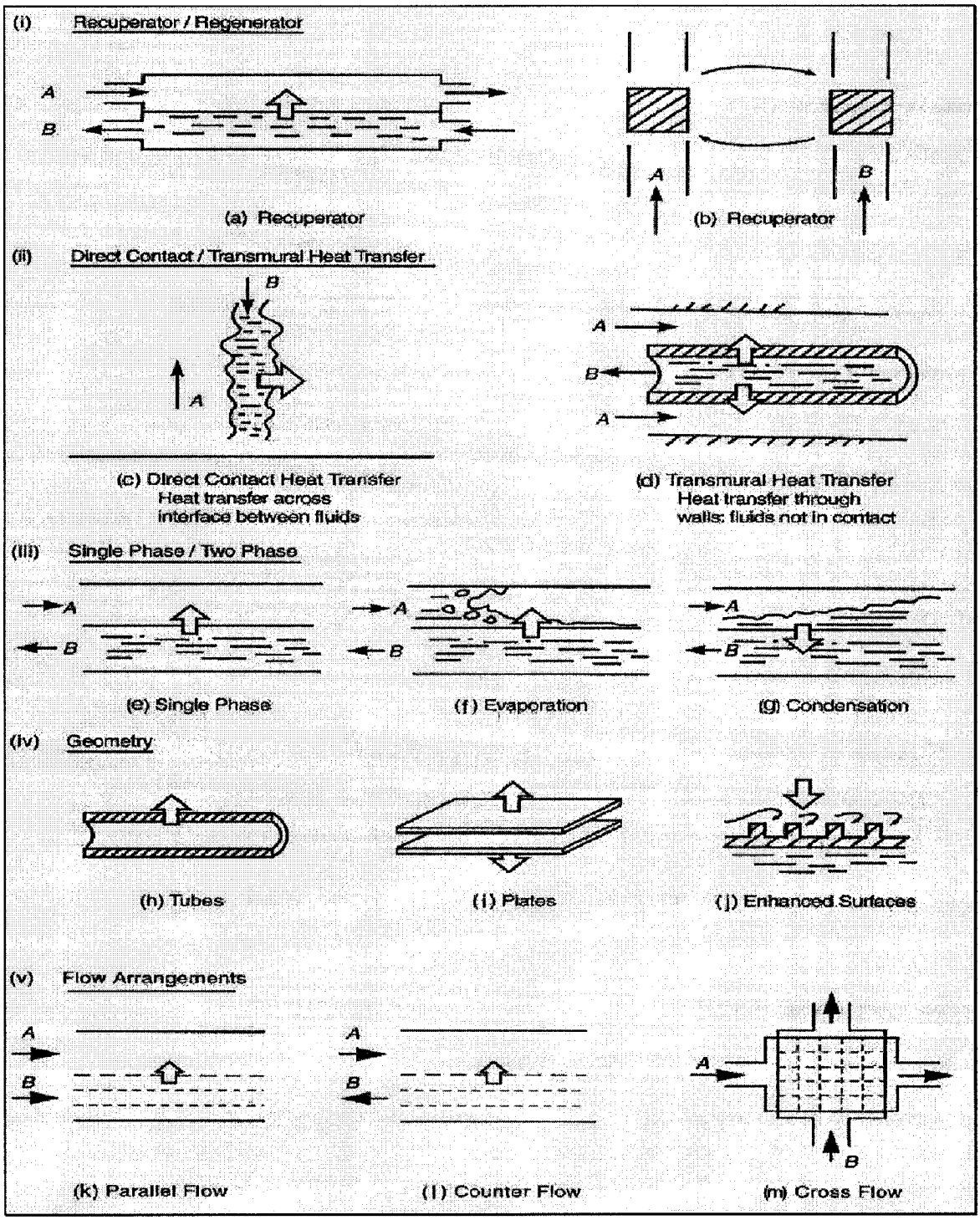

Figure 2-1. Criteria used in the classification of heat exchangers [2].

In *regenerators* or in storage type heat exchangers, the same flow passage (matrix) is alternatively occupied by one of the two fluids. The hot fluid stores the thermal energy in the matrix; during the cold fluid flow through the same passage at a later time, the stored energy will be extracted from the matrix to the cold fluid. Therefore, thermal energy is not transferred through the wall as in heat exchangers with direct transfer mechanism. The schematic of this mechanism is illustrated in figure 2-1b. While the solid is in the cold stream *A*, it loses heat and when it is in the hot stream *B*, it absorbs heat.

Regenerators can be classified as:

1. Rotary regenerators (disk-type or drum-type)
2. Fixed matrix regenerators

2.1.2. Transfer Processes

Upon this criterion, heat exchangers are classified as *direct contact* type and *indirect contact* type. In the *direct contact* type, there is not any wall between two cold and hot streams and heat is transferred between the cold and hot materials through a direct contact between them and occurs through the interface between them (figure 2-1c). In these types of heat exchangers, the streams are two immiscible liquids, a liquid and a gas, or a solid with fluid combination. Spray and tray condensers and cooling towers are good examples of such heat exchangers.

In the *indirect contact* heat exchangers, the cold and hot fluids flow separately while heat energy is transferred through a separating wall, as illustrated in (figure 2-1d). Shell-and-tube and double-pipe heat exchangers are examples of indirect contact heat exchangers.

2.1.3. Geometry of Construction

The major construction types are classified as *Tubular* heat exchangers; *Plate* heat exchangers and *Extended Surface* heat exchangers. These types of heat exchangers are explained in the following sections.

2.1.3.1. Tubular Heat Exchangers

Tubular heat exchangers are built of circular tubes. One fluid flows inside the tubes and the other flows outside of tubes. Tubular heat exchangers can be classified as:

1. Double-pipe heat exchangers
2. Shell-and-tube heat exchangers
3. Spiral-tube heat exchangers

A typical *Double-pipe heat exchanger* consists of one pipe, which is concentrically placed inside another pipe with larger diameter is shown in figure 2-2.

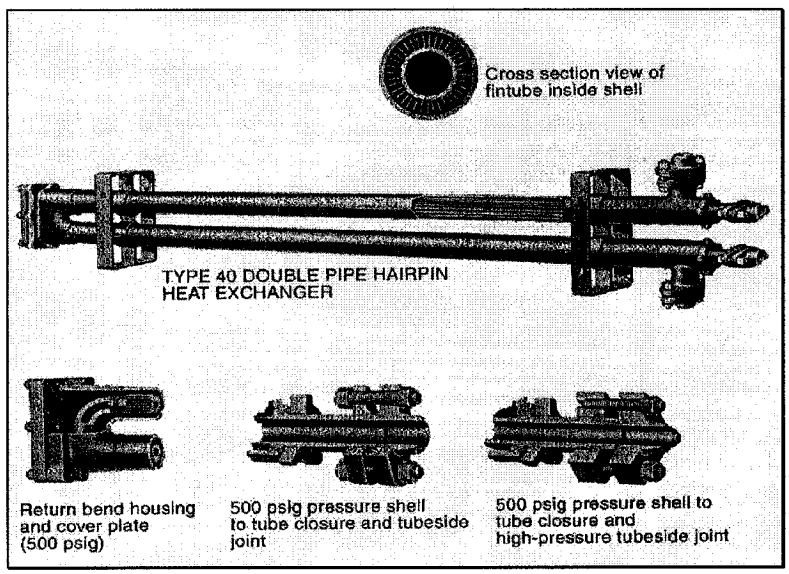

Figure 2-2. Double-pipe hair-pin heat exchanger [2].

Shell-and-tube heat exchangers are built of round tubes mounted in large cylindrical shells, which their axes are parallel. In these heat exchangers one fluid stream flows through the tubes while the other flows on the shell side, across or along the tubes (figure2-3).

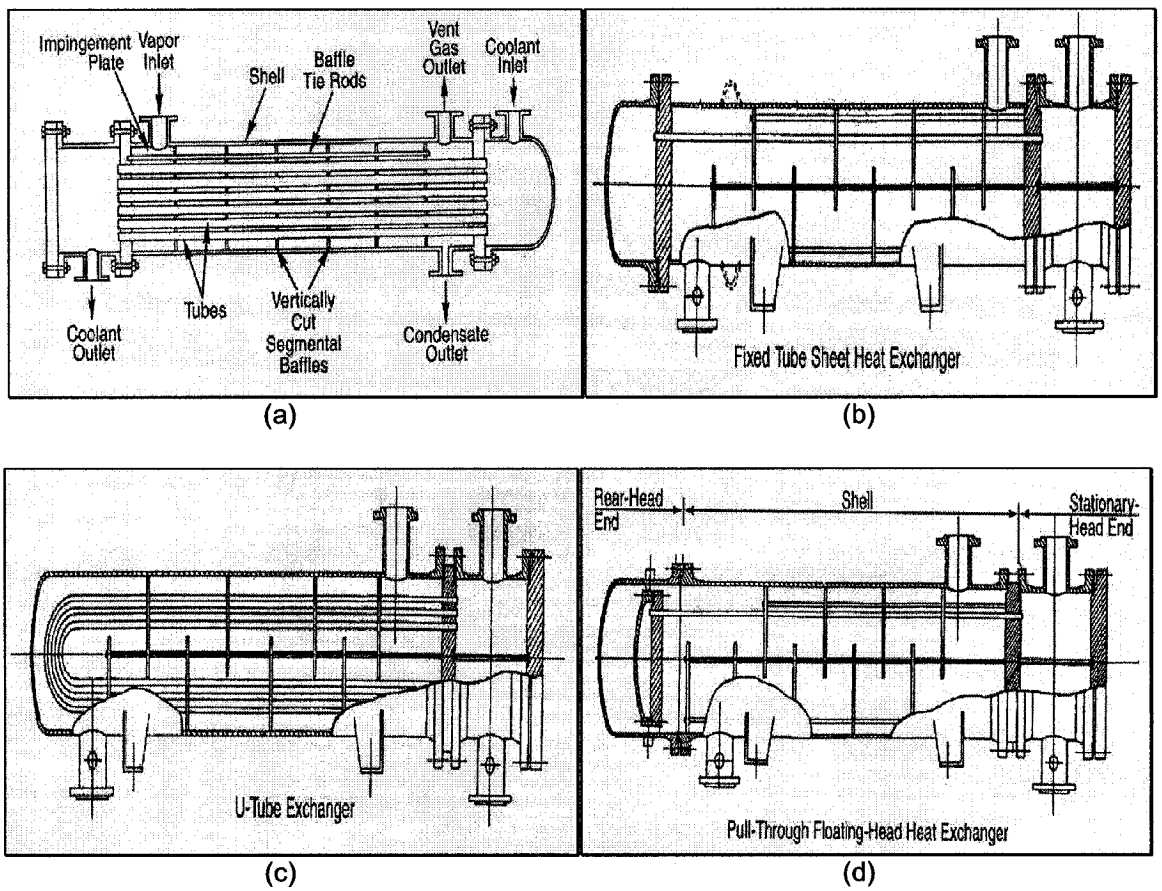

Figure 2-3. Shell-and-tube heat exchanger: (a) TEMA E-type shell with single tube side, (b) A two pass tube, baffled single-pass shell, (c) A U-tube, baffled single-pass shell, (d) Similar to U-tube with a pull-through floating- head [2].

Spiral-tube heat exchangers are built with spirally wound coils covered with a shell or designed as co-axial condensers or evaporators, which are used in refrigeration systems. Spiral-tube heat exchangers are suitable for thermal expansion and clean fluids, since

cleaning is almost impossible. The big advantage of these heat exchangers is higher heat transfer coefficient in comparison with the heat exchangers which contain straight tubes.

2.1.3.2. Plate Heat Exchangers

Plate heat exchangers are built of thin plates forming flow channels and used for transferring heat for any combination of gas, liquid and two-phase streams. These heat exchangers can be classified as *Gasketed plate*, *Spiral plate* or *Lamella*.

A *Gasketed plate heat exchanger* is built of a series of thin plates with wavy surface that separates the fluids as illustrated in figure 2-4. These types of heat exchangers are typically used for heat exchange between two liquid streams. They can be easily cleaned and sterilized because they can be completely disassembled; therefore they have a wide application in the food industries.

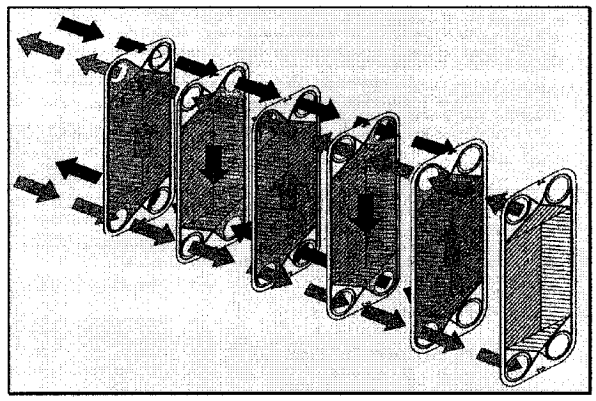

Figure 2-4. Schematic of the flow paths in a gasketed plate heat exchanger [2].

Spiral heat exchangers are formed by rolling of two long, parallel plates into a spiral using a mandrel and welding the edges of adjacent plates to form the channels (figure 2-5). These heat exchangers are quite compact and expensive due to their special manufacturing process.

Lamella heat exchangers are built of parallel, welded, thin plate channels or lamellae (flat tubes or rectangular channels) placed longitudinally in a shell (figure 2-6).

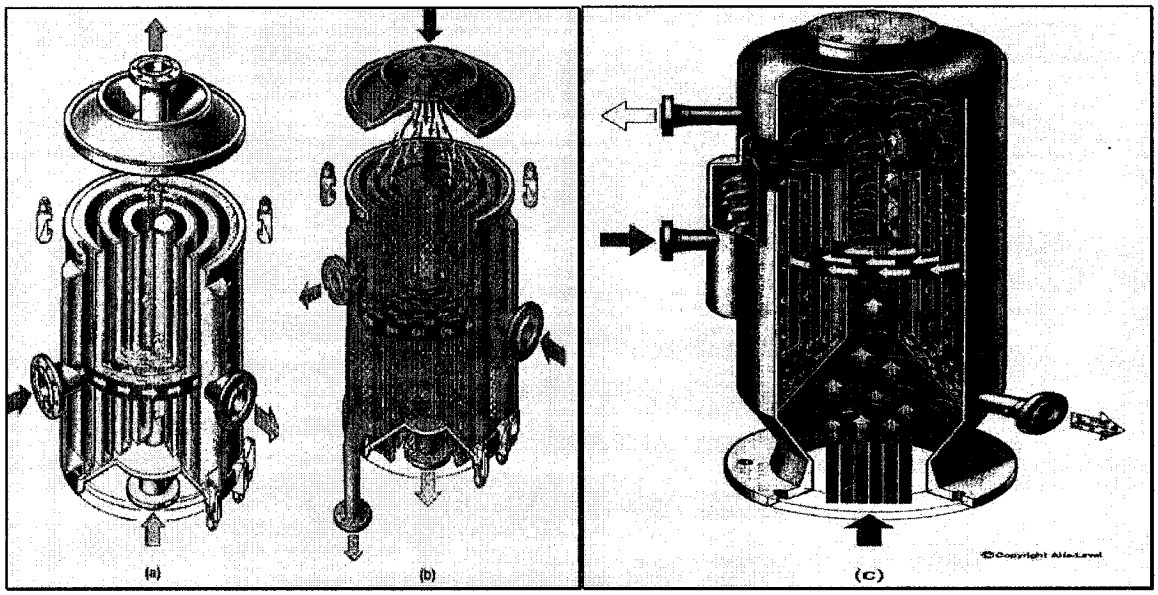

Figure 2-5. Spiral plate heat exchangers [2].

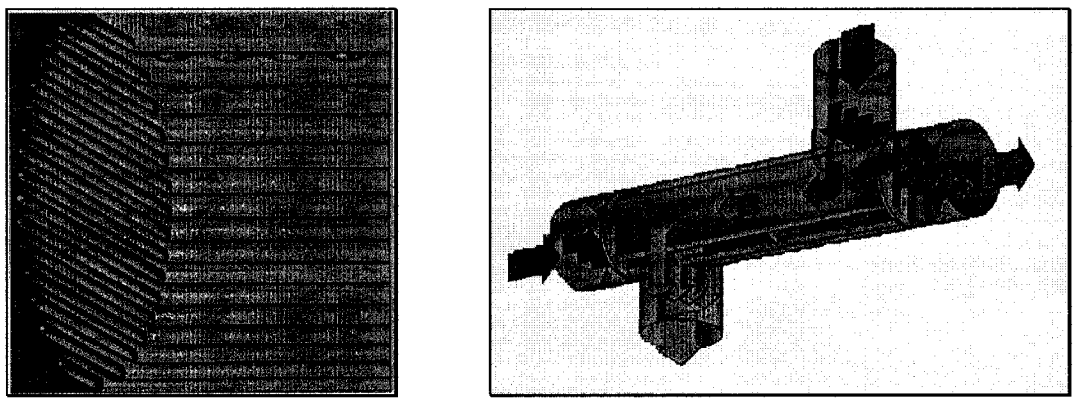

Figure 2-6. Lamella heat exchanger (a) A sort of thin plate channels, (b) Fluids' direction inside the heat exchanger with the thin plate channels in shape (a) inside a tube shell [2].

2.1.3.3. Extended Surface Heat Exchangers

As it is well known that the heat transfer coefficient on the gas side is much lower than on the liquid side, finned heat transfer surfaces are used on the gas side to increase the heat transfer area. Fins are widely used in gas-to-gas and gas-to-liquid heat exchangers whenever the heat transfer coefficient is low. *Extended surface heat exchangers* are devices with fins on the primary heat surface with the object of increasing heat transfer area. The most common types of such heat exchangers are *Plate-fin* and *Tube-fin* heat exchangers.

Plate-fin heat exchangers are used for gas-to-gas heat exchangers. Mass and volume reduction are particularly important in such heat exchanges. In addition fluid streams are separated by flat plates and a corrugated (wavy) plate fin, which is sandwiched between two flat plates (figure 2-7).

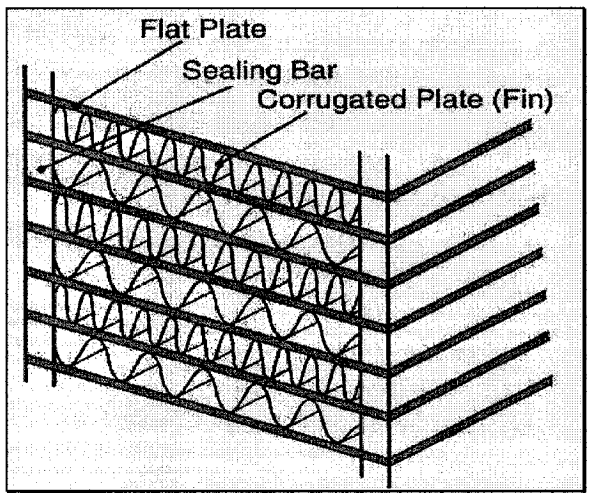

Figure 2-7. Basic construction of plate-fin exchanger [2].

Tube-fin heat exchangers are used in gas-to-liquid heat exchangers. Fins are required on the gas side because of the lower heat transfer coefficients on the gas side in comparison

with the liquid side. These types of heat exchangers include an array of tubes with fins, which are fabricated around the tubes (figure 2-8). The fins can be fabricated normal, transverse, helical or longitudinal to the tubes.

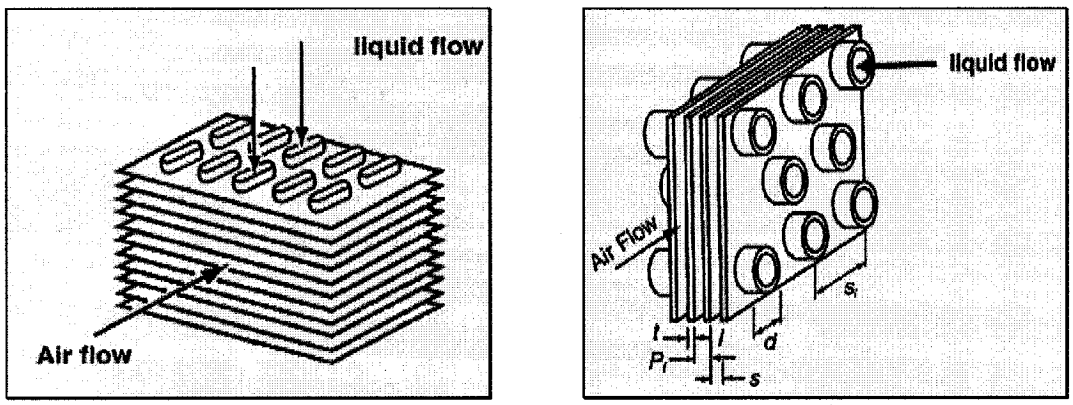

Figure 2-8. Tube-fin heat exchangers: (a) Flatted tube-fin; (b) Round tube-fin [2].

2.1.4. Heat Transfer Mechanism

Heat exchangers can be classified according to the mechanism of heat transfer as:

1. Single-phase convection on both sides
2. Single-phase convection on one side, two-phase convection on the other side
3. Two-phase convection on both sides

These classifications are shown in figures 2-1e to 2-1g. Two possible modes of two-phase flow are shown in figures 2-1f and 2-1g. In figure 2-1f fluid *A*, which is evaporated, receive heat from fluid *B* and in figure 2-1g fluid *A*, which is condensed, giving up heat to fluid *B*.

2.1.5. Flow Arrangements

Heat exchangers can be classified according to the fluid-flow pass through the heat exchanger as:

1. Parallel-flow heat exchangers
2. Counter-flow heat exchangers
3. Cross-flow heat exchangers

In *Parallel-flow heat exchangers*, the two fluid streams enter together at one end, flow in the same direction and leave the heat exchanger together at the other end. In *Counter-flow heat exchangers*, two fluid streams flow in opposite directions and in *Cross-flow heat exchangers*, one fluid flows through the heat transfer surface at a defined angle with the flow path of the other fluid (figure 2-9).

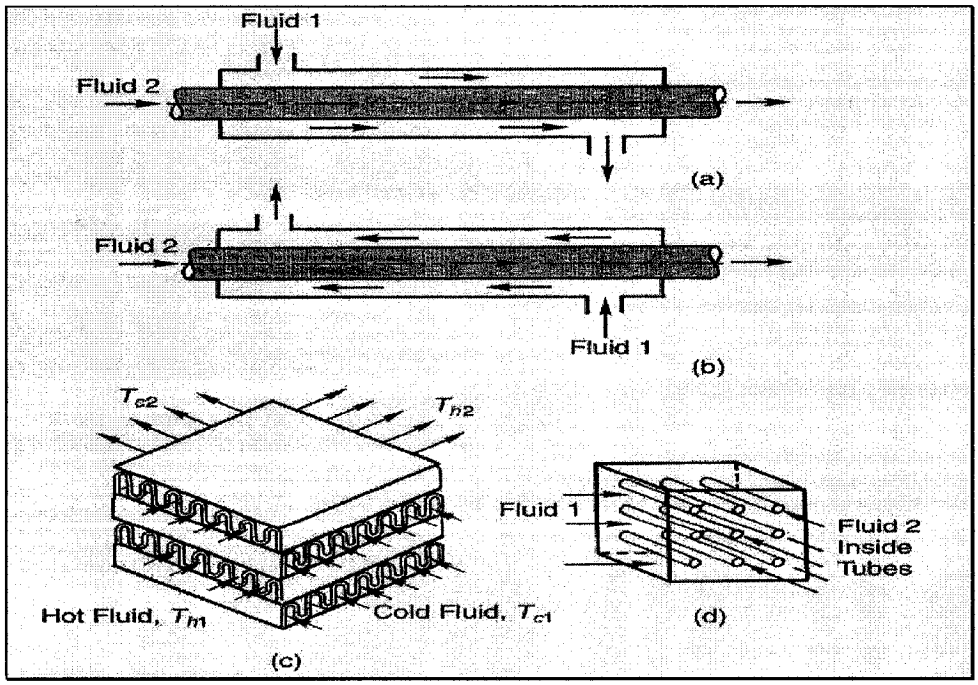

Figure 2-9.Flow arrangement classifications: (a) Parallel-flow; (b) Counter-flow; (c) Cross-flow, both fluids unmixed; (d) Cross-flow, fluid1 mixed and fluid 2 unmixed [2].

In the *Cross-flow* arrangement, the flow can be classified as:

1. Mixed-flow
2. Unmixed-flow

In the m*ixed-flow*, one fluid flows through its individual channel while the other fluid flows freely around the channels of the first flow. In the u*nmixed-flow*, both of the fluids flow through individual channels.

2.2. Basic Models for Heat Transfer

Conduction is one of the forms of heat transfer. A simple model for conduction is illustrated in figure 2-10 (a).

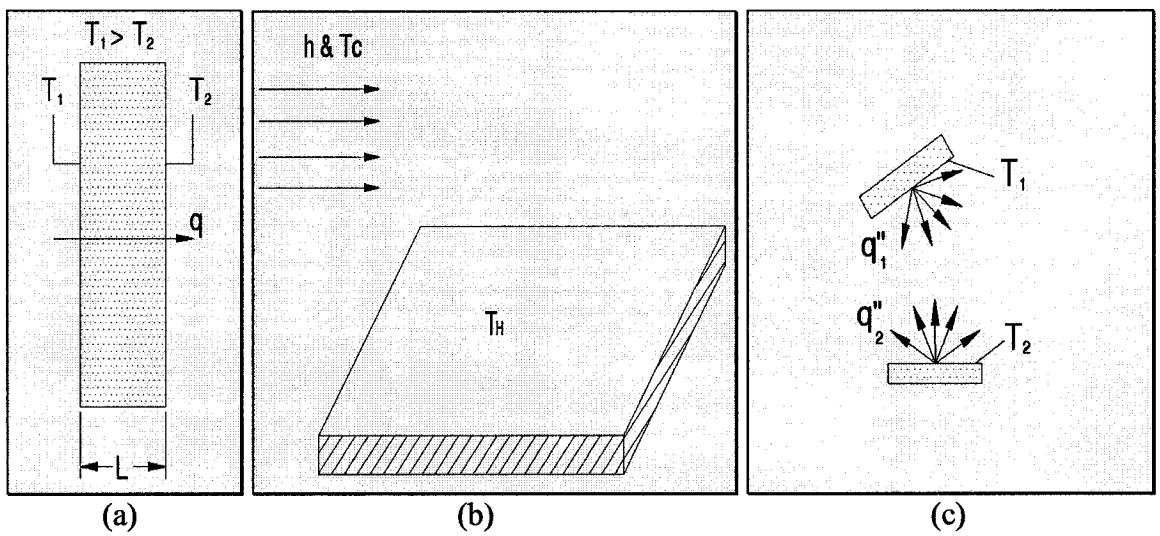

Figure 2-10. Basic models of heat transfer (a) Conduction, (b) Convection, (c) Radiation.

The flow of heat by conduction occurs via collisions between atoms and molecules in the substance and the subsequent transfer of kinetic energy. Consider two substances at

different temperatures separated by a barrier which is subsequently removed, as in the figure 2-11.

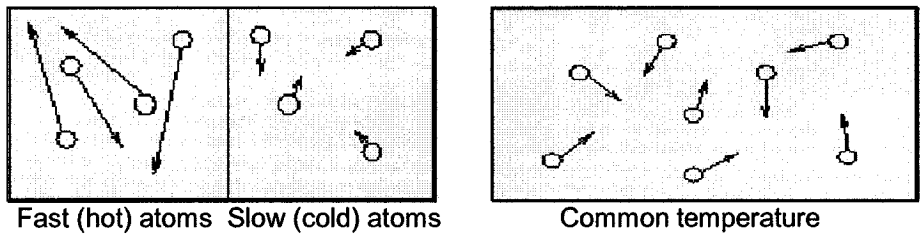

Figure 2-11. Heat transfer by conduction

When the barrier is removed, the fast (hot) atoms collide with the slow (cold) ones. In such collisions the faster atoms lose some speed and the slower ones gain speed; thus, the fast ones transfer some of their kinetic energy to the slow ones. This transfer of kinetic energy from the hot to the cold side is called a flow of heat through conduction.

Different materials transfer heat by conduction at different rates - this is measured by the material's thermal conductivity. For a given temperature difference between two surfaces, materials with a large thermal conductivity will transfer large amounts of heat over time - such materials, like copper, are good thermal conductors. Conversely, materials with low thermal conductivities will transfer small amounts of heat over time - these materials, like concrete, are poor thermal conductors. This is why if you throw a piece of copper and a piece of concrete into a campfire, the copper will heat up much more quickly than the concrete. It is also why fiberglass insulation, and also feathers and fur, have air pockets - dead air is a poor thermal conductor, and so the air pockets aid in cutting back on the heat loss through the material.

The amount of transferred heat from the hot surface to the cold surface can be considered from equation 2-1 [3]:

$$q = -k \cdot A \frac{(T_2 - T_1)}{L} \tag{2-1}$$

In equation 2-1, q is the transferred heat from the hot surface to the cold surface (W), k is the thermal conductivity of the solid material (W/m.K), T_1 and T_2 are respectively the temperature of the hot surface and the temperature cold surface (K), A is the area of the surface that heat is transferred through it (m^2) and L is the distance between the hot and the cold surfaces. According to this equation the dissipated heat is proportional to the area, the temperature difference, and thermal conductivity of the solid and is related to the distance between the hot and the cold surfaces. A higher dissipated heat would be achieved through increasing any of the above mentioned parameters except for L, which by decreasing this distance higher dissipated heat would be achieved.

Another form of heat transfer is convection. A simple model for the forced convection heat transfer is illustrated in figure 2-10 (b).

Convection is the flow of heat through a bulk, macroscopic movement of material from a hot region to a cool region, as opposed to the microscopic transfer of heat between atoms involved with conduction. Consider heating up a local region of air. As this air heats, the molecules spread out, causing this region to become less dense than the surrounding, unheated air. For reasons discussed in the previous section, being less dense than the surrounding cooler air, the hot air will subsequently rise due to buoyant forces - this movement of hot air into a cooler region is then said to transfer heat by convection.

Heating a pot of water on a stove is a good example of the transfer of heat by convection. When the stove is first turned on heat is transferred first by conduction between the element through the bottom of the pot to the water. However, eventually the water starts bubbling. These bubbles are actually local regions of hot water rising to the surface, thereby transferring heat from the hot water at the bottom to the cooler water at the top by convection. At the same time, the cooler, more dense water at the top will sink to the bottom, where it is subsequently heated. These convection currents are illustrated in figure 2-12.

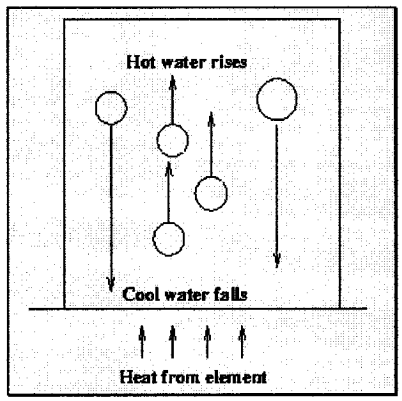

Figure 2-12. Convection currents in boiling water

Now consider two regions separated by a barrier, one at a higher pressure relative to the other, and subsequently remove the barrier, as in figure 2-13.

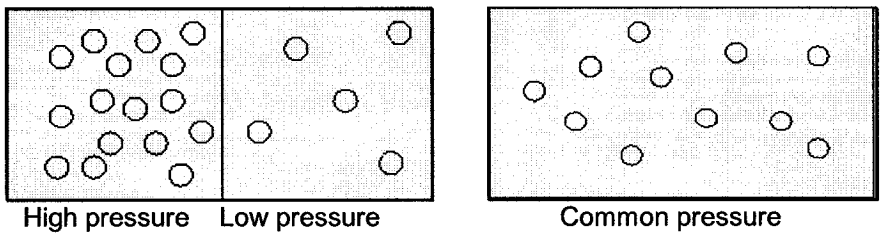

Figure 2-13. Flow of material through a pressure difference

When the barrier is removed, material in the high pressure (high density) area will flow to the low pressure (low density) area. If the low pressure region was originally created by heating of the material, one sees that movement of material in this way is an example of heat flow by convection.

The amount of transferred heat from the higher temperature surface to the flowing fluid with lower temperature can be considered from equation 2-2 [3]:

$$q = h \cdot A(T_H - T_C) \tag{2-2}$$

In equation 2-2, q is the transferred heat from the high temperature surface to the coolant fluid (W), h is the film coefficient of the flowing fluid (W/m².K), T_H and T_C are respectively the temperature of the hot surface and the temperature of the flowing fluid (K) and A is the contact surface area between the hot surface and the flowing fluid (m²). According to this equation the dissipated heat is proportional to the contact area, the temperature difference and film coefficient. A higher dissipated heat would be achieved through increasing any of the above mentioned parameters.

The third and last form of heat transfer is radiation. A simple model for radiation is illustrated in figure 2-10 (c). This is the means by which heat is transferred, for example, from the sun to the earth through mostly empty space. Such a transfer cannot occur via convection or conduction, which require the movement of material from one place to another or the collisions of molecules within the material. Often the energy of heat can go into making light, such as that coming from a hot campfire. This light, being a wave, carries energy, and so can move from one place to another without requiring an

intervening medium. When this light reaches you, part of the energy of the wave gets converted back into heat, which is why you feel warm, sitting beside a campfire. Some of the light can be in the form of visible light that we can see, but a great deal of the light emitted is infrared light, whose longer wavelength is detectable only with special infrared detectors. The hotter the object is, the less infrared light is emitted, and the more visible light. For example, human beings, at a temperature of about 37° Celsius, emit almost exclusively infrared light, which is why we don't see each other glowing in the dark. On the other hand, the hot filament of a light bulb emits considerably more visible light.

The maximum net amount of heat flux that can be transferred from a body can be expressed from Stefan-Boltzman law (equation 2-3) [3]:

$$q'' = \frac{q}{A} = \varepsilon \cdot \sigma \cdot T_s^{\,4} \qquad (2\text{-}3)$$

In equation 2-3, q'' is the transferred heat flux from a surface to surrounding space (W/m^2), σ is the Stefan-Boltzman constant (σ = 5.67 × 10^{-8} $W/m^2.K^4$), T_S is the temperature of the surface (K), ε is the emissivity (a constant factor between 0 to 1 and is related to the surface type) and A is the surface area of the object (m^2). According to this equation the dissipated heat is proportional to the contact area, the temperature of the surface and emissivity.

Bodies that emit less thermal radiation than a blackbody have surface emissivities less than 1. If the surface emissivity is independent of wavelength, then the body is called a "gray" body, in that no particular wavelength (or color) is favored.

The net heat transfer q (W) from a small gray body at absolute temperature T_S (K) with surface emissivity ε and total area of A to a much larger enclosing gray (or black) body at absolute temperature T_{Sur} (K) is given by equation 2-4 [3]:

$$q = \varepsilon \cdot A \cdot \sigma \cdot (T_s^{\,4} - T_{sur}^{\,4}) \qquad (2\text{-}4)$$

A higher dissipated heat flux would be achieved through increasing the surface temperature and area and decreasing the absolute temperature of the larger enclosing body.

2.2.1. Experimental Analysis

The schematic of aluminum specimens, which have been used for the experimental process are illustrated on figure 2-14.

In the first experimental specimen, the height of rectangular pin is 4″ and the thickness of the square base is 1″. A ¼ ″ hole is drilled inside the model to the depth of 4.72″. One of the LM35 temperature sensors (figure 2-15) is installed on the bottom of this hole to detect the temperature inside the base of the model.

The second experimental specimen is considered half the scale of the first one in every dimension except the dimension of the hole in diameter, which is the same as the first one because of limitations on the size of LM35 temperature sensors.

The third experimental specimen is considered with the same dimensions of the first specimen except in the height of the rectangular pin, which is equal to 3″, and without any hole inside of it.

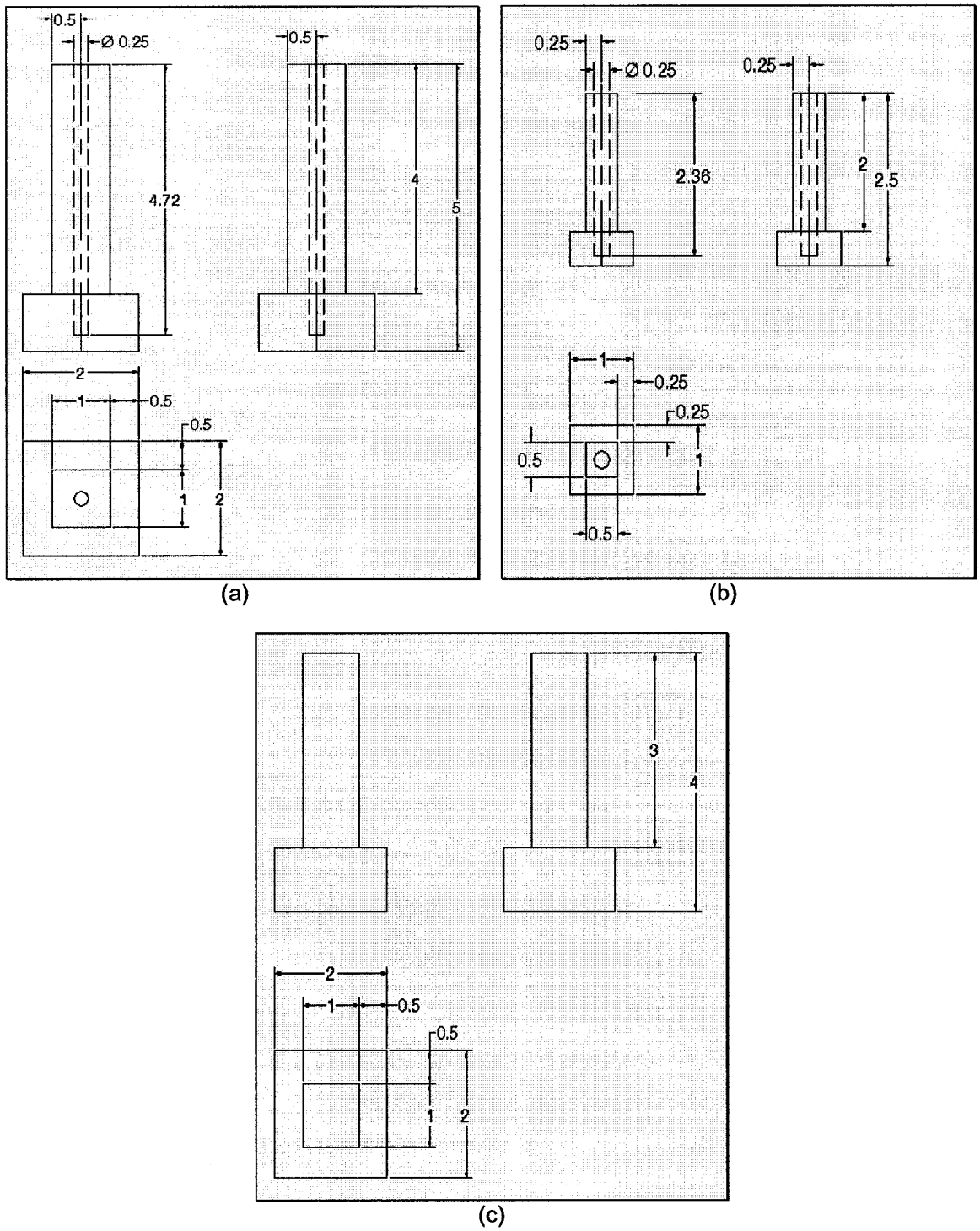

Figure 2-14.Schematic dimensions of aluminum specimens, (a) Specimen1, (b) Specimen 2, (c) Specimen 3 (dimensions are in Inches)

All the models were considered based on the following reasons:

- To find out the influence of two different scales on the temperature distribution.
- To find out the influence of different heights of the pins on the temperature distribution.
- Size limitation on the temperature sensors (illustrated on figure 2-15), pointed towards to make such size specimens.
- Each design should be in conformity with available experimental instruments (wind tunnel height, as illustrated in figure 2-16).

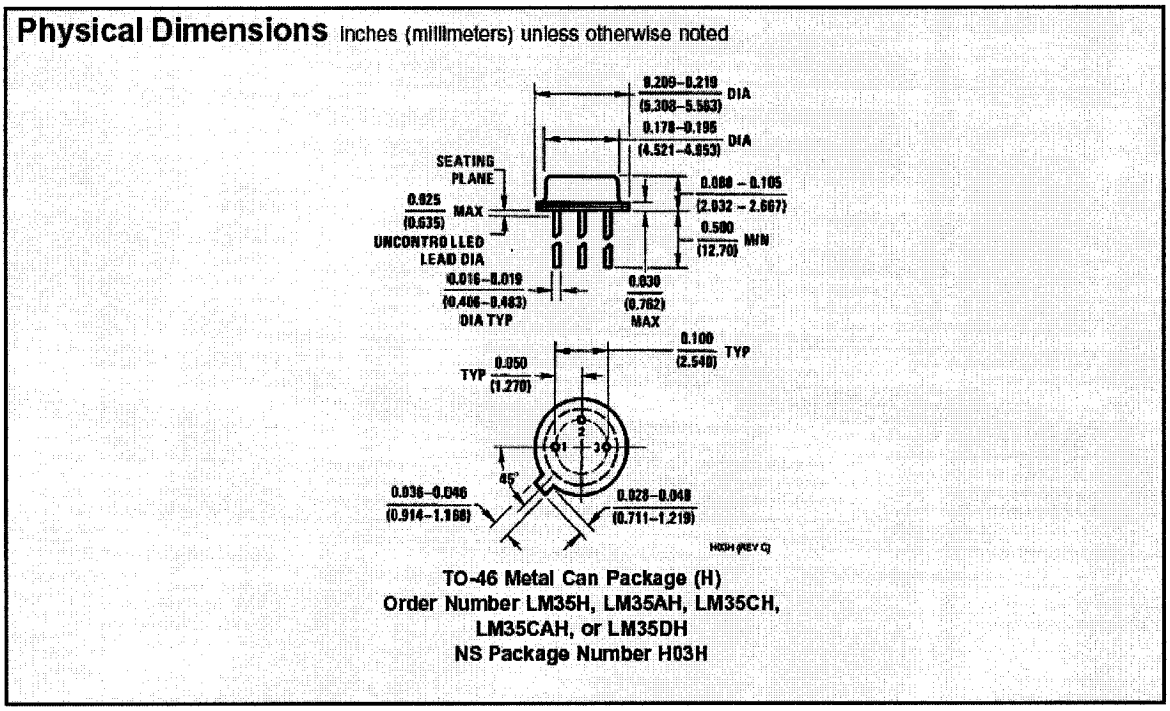

Figure 2-15. Dimensions of LM 35 temperature sensors [16]

In all the experiments a 450mm distance has been considered from the beginning of the wind tunnel to the position of the models to reach a uniform velocity profile through the wind tunnel and around the models for any value of the velocity.

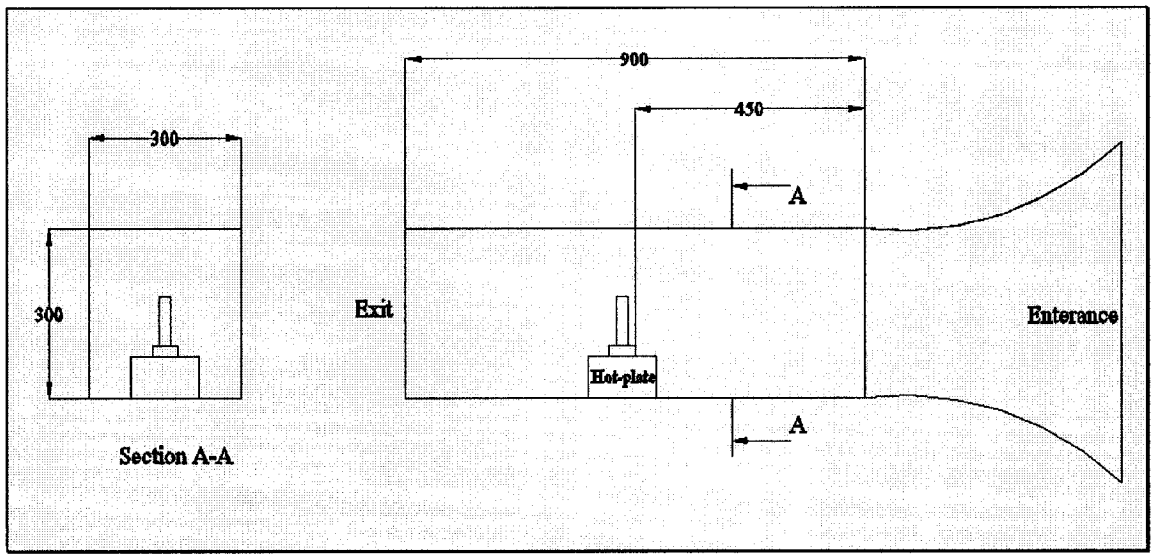

Figure 2-16. Schematic of wind tunnel (dimensions in mm)

2.2.2. ANSYS Modeling

This section covers the modeling procedure of each aluminum specimen (discussed in previous part) in ANSYS area and application of boundary conditions.

The following steps have been applied to create and solve a model in the ANSYS environment:

- Definition of 3-Dimensional Tetrahedral thermal solid (element 87), 10 nodes from the thermal mass solid (This thermal element is recommended by ANSYS and is compatible to any three dimensional and non uniform shape).
- Definition of the conductivity of Aluminum (237W/m.K by less than 0.01% diversity in the range of -73°C to 227°C), [26]-[29].
- Create 3-dimensional models on the ANSYS area, using modeling commands.
- Meshing the models and applying the boundary conditions.
- Solving the problems and get the output result.

2.2.3. Defining Boundary Conditions

This segment covers analytical procedure to find thermal boundary conditions. The analyses are based on the following assumptions:

- The flowing fluid inside the wind tunnel (illustrated in figure 2-13), is air at constant temperature of 23°C (average room temperature at the time).
- The velocity profile is uniform around the models (The models are located at a distance of 450mm from the entrance of the wind tunnel to have more uniform velocity profile for any velocity).
- Solid elements have been modeled with no interaction with solid fluid elements.

Thermo-physical properties of air, which are used for the analyses in this section, are adapted from tables of the "Heat Transfer Handbook" [17] and theoretical equations for estimating the value of the local heat transfer coefficient at each surface of the specimens are adapted from the investigations in concern with the cross flow around rectangular tubes [18]-[24].

T. Igarashi [19] carried out experimental investigations on the characteristics of the flow around rectangular cylinders for different ratios of 1 to 4 between the two edges of the rectangular section cylinders and found distinct changes of flow patterns at two critical ratios of 0.67 and 2.8. He also measured local heat transfer coefficient distribution around a square cylinder and rectangular cylinders using thermocouples and found that heat transfer coefficients are closely related to the drag coefficients [19]-[24].

Also S. Y. Yoo, Jong. H. Park, C. H. Chung and M. K. Chung [18] have recently carried out some investigations by using naphthalene sublimation technique to measure detailed local mass transfer rates from a rectangular cylinder by changing the inlet air velocity, then the measured mass transfer data are converted to their counter part of heat transfer process by applying heat/mass transfer analogy. They compared the mass transfer data with those of heat transfer, which obtained by T. Igarashi [22] with the same geometries and flow conditions. As a result they found that:

- Heat and mass transfer are in good agreement with each other but local rates of mass transfer are much higher than those of heat transfer when the separated flow reattaches to the side face of the cylinder.
- The variation trend and values of Nusselt number are similar for all cases.
- Heat transfer coefficients in the constant heat flux boundary condition are higher than those in the constant temperature boundary condition [25].

Therefore the heat transfer coefficients can be obtained from the experimental results of T. Igarashi [20], which evaluated the average heat transfer coefficients from the distributions of the local heat transfer coefficients for different angles of attack (α) from 0° to 45° in the range of $5.6\times10^{3} \leq \mathrm{Re} \leq 5.6\times10^{4}$, as the boundary conditions for the ANSYS simulations. He found that the average heat transfer coefficient for a square prism at a constant wall temperature to an air stream can be expressed by the following equations:

$$\alpha = 0^{\circ}; \qquad Nu_{m} = 0.14\ \mathrm{Re}^{0.66} \tag{2-5}$$

$$\alpha = 45^{\circ}; \quad Nu_{m} = 0.27\ \mathrm{Re}^{0.59} \tag{2-6}$$

Reynolds number and the average heat transfer coefficient can be obtained from the following equations:

$$\mathrm{Re} = \frac{V \cdot d}{\nu} \tag{2-7}$$

$$h_{m} = \frac{Nu_{m} \cdot K}{d} \tag{2-8}$$

By substituting the equations 2-7 and 2-8 in equations 2-5 and 2-6, one will obtain:

$$\alpha = 0^{\circ}; \quad h_{m} = 0.14 \cdot \left(\frac{V \cdot d}{\nu}\right)^{0.66} \cdot K / d \tag{2-9}$$

$$\alpha = 45^{\circ}; \quad h_{m} = 0.27 \cdot \left(\frac{V \cdot d}{\nu}\right)^{0.59} \cdot K / d \tag{2-10}$$

In the above equations, V (m/s) and ν (m^2/s) are velocity and kinematic viscosity of the flowing air respectively, d (m) is the edge dimension of the square prism, Re (Reynolds number) is the ratio of (Inertial-terms/Viscous-terms) in the flow, Nu (Nusselt number) is the ratio of (Convection heat transfer/Conduction heat transfer) on a system, h_m ($W/m^2.K$) is average heat transfer coefficient of the flowing air on the contact surface with the models, K (W/m.K) is the thermal conductivity of the flowing air and α is the angle of attack.

Physical properties of the flowing fluid are applied as boundary conditions at the film temperature. From the imposed requirement of the model, to represent as appropriate as

possible the experimental results, the film temperature on the specimen was calculated based on the following simple relationship:

$$t_{film} = N \cdot T_{hp} + t_f / 2 \qquad (2\text{-}11)$$

In equation 2-11, t_{film} (°C) is the film temperature, T_{hp} (°C) is the hot plate temperature, t_f (°C) is the fluid temperature and N is temperature coefficient factor.

In specimens 1 and 2, N is equal to 0.5 and 0.4 respectively for $Re<5.6\times10^3$ and $Re\geq5.6\times10^3$. In specimen 3, N can be found from figures 2-17, 2-18 and 2-19 and for $Re<5.6\times10^3$, N is equal to 0.5. These values for N are based on a lot of trial and errors, which have been applied to find the exact solution results with the minimum different error between the experimental and simulation results.

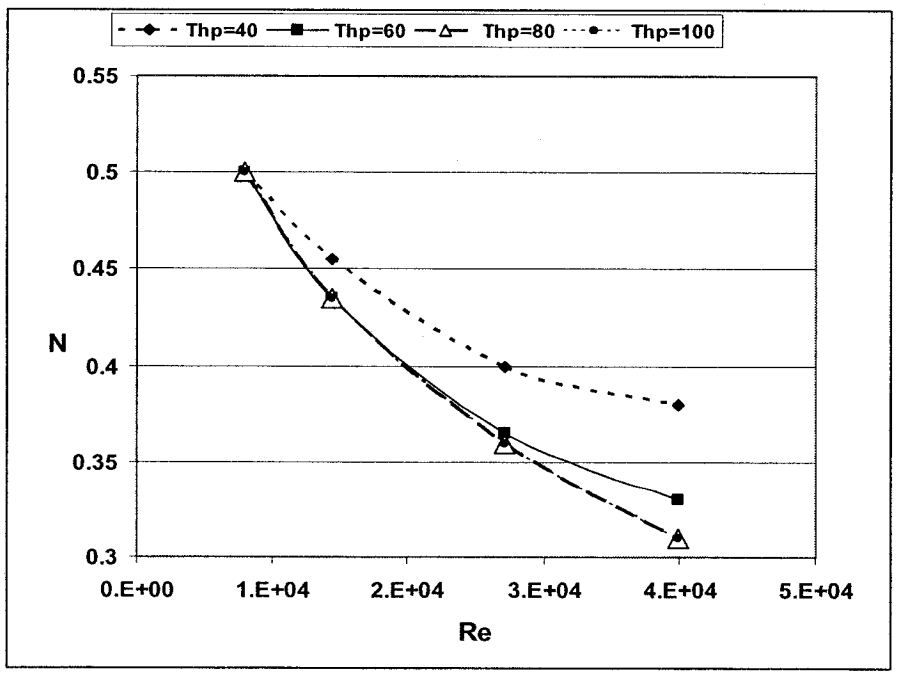

Figure 2-17. Relation between N and Re at different hot plate temperatures and α=0°

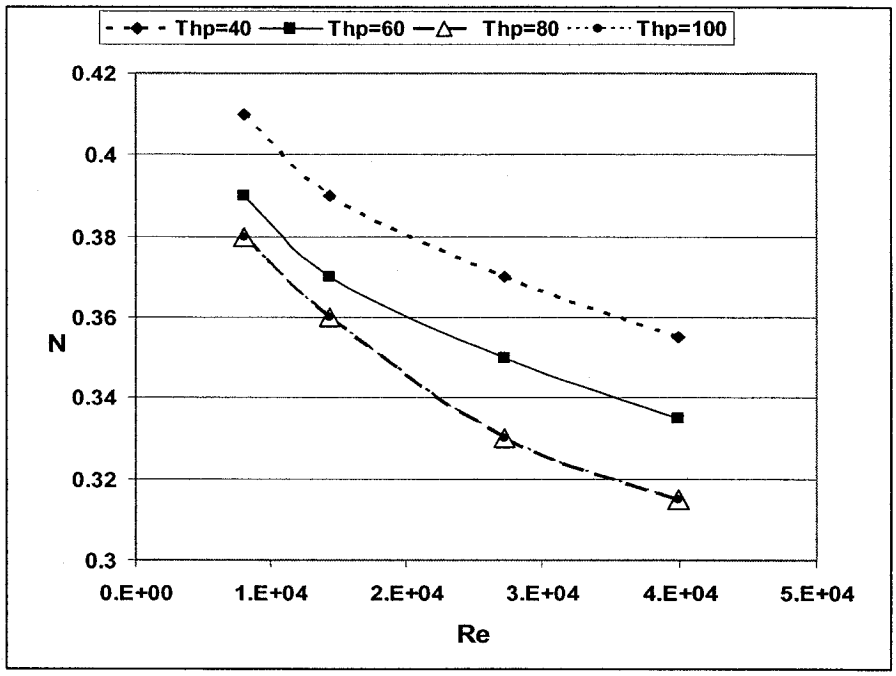

Figure 2-18. Relation between N and Re at different hot plate temperatures and α=45°

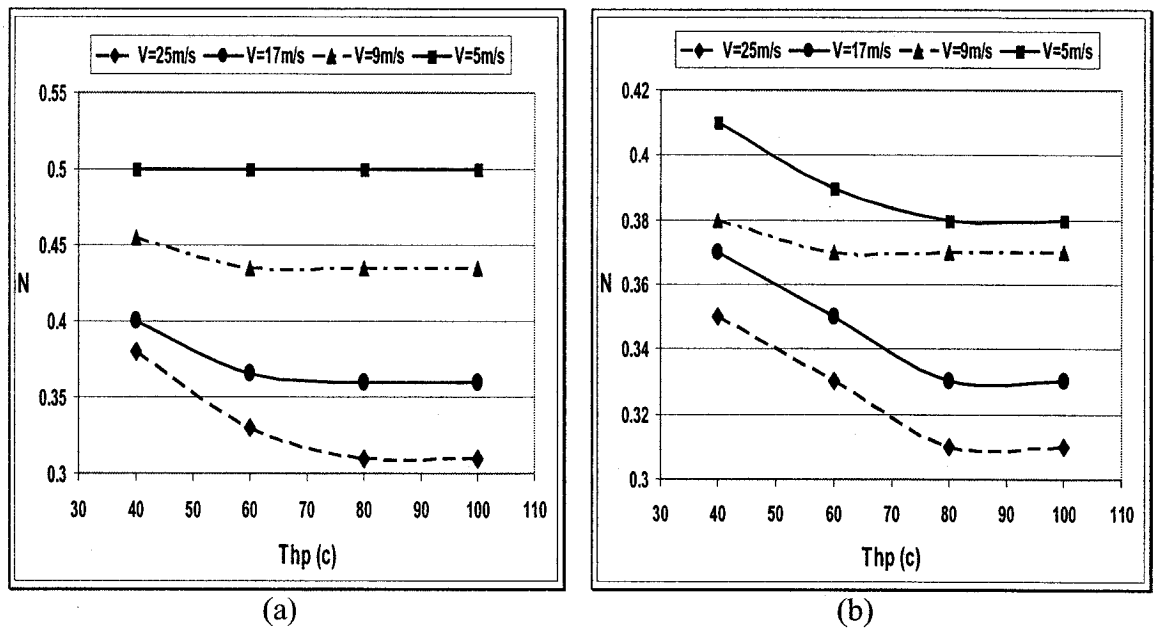

Figure 2-19. Relation between N and Thp at different flow velocities for
(a) α=0°, (b) α=45°

It can be seen that at any specific temperature of the hot plate:

- By increasing the Reynolds number and consequently the velocity of the flowing fluid, the amount of temperature coefficient factor (N) is decreasing.
- Film temperature is decreasing by increasing the velocity of the flowing fluid.
- Whatever happens in reality shows that the amount of film temperature is less than its considered value for analytical estimations (average of the fluid and surface temperatures), especially for high velocities of the flowing fluid.
- By increasing the orientation angle, the amount of temperature coefficient factor (N) is decreasing and consequently the film temperature is decreasing.

Also at any constant velocity for the flowing fluid:

- At any orientation angle, by increasing the hot plate temperature, temperature coefficient factor (N) is decreasing and as a result film temperature is decreasing.
- By increasing the orientation angle, N is decreasing.

Finally it can be concluded that increasing the velocity of the flowing fluid and orientation angle up to 45° cause up to 38% decrease in the amount of temperature coefficient factor (N) and up to 30% decrease in the amount of film temperature and consequently in compare with the analytical estimations it has a significant effect on the transferred heat from the specimens to the flowing fluid.

2.3. Experimental Setup and Procedure

The schematic of the experimental setup is illustrated on figure 2-20.

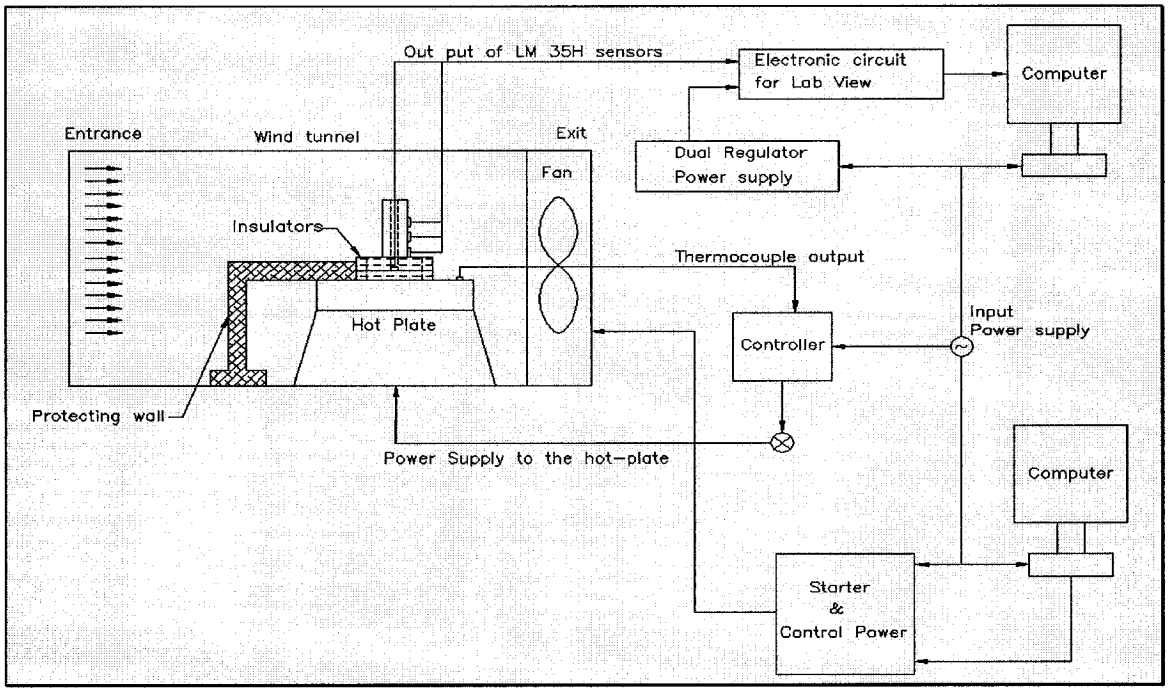

Figure 2-20. Schematic of experimental setup

The experimental apparatus are:

- $310\ mm \times 310\ mm \times 900\ mm$ wind tunnel with the ability of producing up to 30 m/s velocity of the flowing air (figure 2-21).
- 4"×4" hotplate.
- LM 35H temperature sensors, figure 2-15 [16].
- E5CN temperature controller [15].
- Aluminum specimens, figures 2-14 and 2-21.
- T-type thermocouple for controlling the surface temperature of the hotplate.
- Computers and electrical connections.

- Lab View software and its electronic circuit (Data Acquisition System, DAS).
- Dual regulator power supply (in case of necessity).
- A velocity meter (not shown), used to measure and re-check the velocity of the flowing air.
- Protecting wall, used to protect the hotplate and its operation from the influence of the flowing air.

(a)

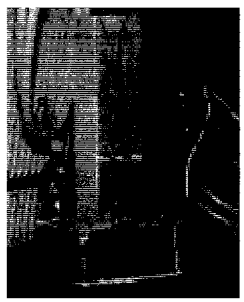

(b)

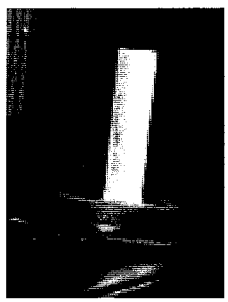

(c)

Figure 2-21. Photos of (a) Wind tunnel with the hotplate and aluminum specimen inside it, (b) Specimen 1, (c) Specimen 2

Each specimen is clamped on the surface of the hotplate and the hotplate is clamped inside the wind tunnel. A protecting wall is installed in front of the hotplate, which protects the surface of the hotplate from the flowing fluid and having less influence on the surface temperature of the hotplate and its operation. Four LM 35H temperature

sensors have been installed on different locations of the first specimen as well as the second specimen and three sensors for the third specimen. The T-type thermocouple is positioned between the bottom of Aluminum specimens and the surface of the hotplate to detect the temperature of the hotplate at the same time with other sensors.

The output of the LM 35H temperature sensors are connected to a Lab View electronic circuit/terminal (DAS), which is connected directly to the computer and the results are transferred into the Lab View software, which is able to save and plot the measured data in time domain. The output of the T-type thermocouple is connected to the E5CN temperature controller, which is controlling the input power supply of the hotplate to keep the surface temperature of the hotplate in a defined constant set point temperature.

2.3.1. Installation and Adjustment of the Experimental Setup

This section demonstrates the procedure of installation and adjustment of experimental setup. This procedure includes the following two major steps:

Step 1: This step contains the installation of a T-type thermocouple with the temperature controller and setting them on a specific temperature. This procedure is explained briefly in the "Instruction manual" of the E5CN temperature controller [15].

Schematic view of connections from the temperature controller to the hot-plate and T-type thermocouple is illustrated in figure 2-22. Terminal numbers 4 and 5 get the input signal from the T-type thermocouple. Then the controller, which has been set up on a specific set point temperature, is sending an out put signal through terminal numbers 1 and 2 to the hotplate. In this case one of the output terminals (number 2) is directly

connected to the hotplate and the other output is passing through terminal number 9, which is one of the input power bridges for the controller itself and acts as an on and off key for this process. Terminal number 10 is the other input power bridge for both the controller and the hotplate. So in this way the controller will turn off the supply power to the hotplate in case of reaching the surface temperature to the set point temperature.

Step 2: This step covers the installation of LM 35H temperature sensors and their characterization. This step includes the following processes:

A. Soldering compatible wires to the pins on the end of each sensor.

B. Testing and calibration of the sensors.

C. Installation of sensors at their positions on the aluminum models.

D. Installation of "soldier terminals" on the models and soldering the out put wires of sensors to these terminals.

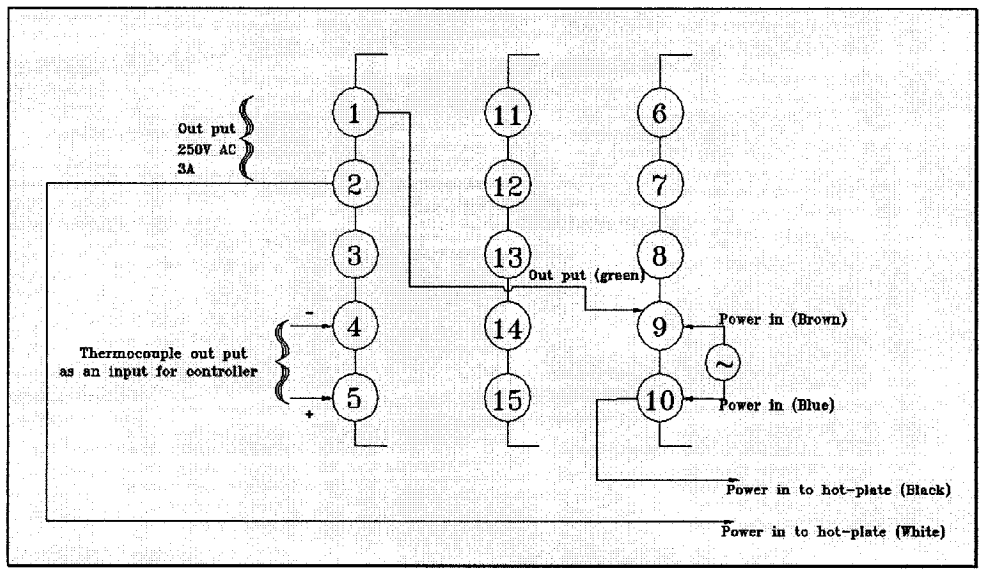

Figure 2-22. Connections of E5CN temperature controller to the hotplate and T-type thermocouple

Process A; at first the compatible wires with the sensors were soldered to three pins of each sensor. The pin, which is on the right side (figure 2-15), is called the reference (as the ground) and the left side pin is called the opposite pin (as positive pole) and the middle one is called the middle pin (as negative pole). The existed currents on each pin are; 0 for the reference pin, 4.9 mA for the opposite pin and 43 kA for middle pin.

Process B; each sensor was tested to certify their ability to operate perfectly. Meanwhile they were calibrated with a calibrated thermometer inside the laboratory. The process contains the following procedures and the results are presented on table 2-1:

1. The input voltage was set on 10 Volts in the tester, which represents the operation voltage (ranging between -2 to 35 volts) [16].
2. The reference pin was connected to the ground.
3. The opposite pin was connected to the supply voltage.
4. The middle pin was connected to the out-put monitor.
5. The ambient temperature was read from the output monitor and compared with the output of the local calibrated thermometer. This monitor shows the output of the sensors by the scale of 1°C/10mA. As an example if 0.213 is shown on the output, then the temperature is equal to:

$$T = 273\ .15 + \frac{0.213}{10 \times 10^{-3}} = 294\ .45\ K$$

6. The sensors were heated and their output signal have been checked and compared with the output results shown by the calibrated thermometer.

Table 2-1. Results of process B

Sensor	1	2	3	4	5	6	7	8	9	10	11
Ambient temperature	293.9	294.95	294.86	295.03	295.08	295.03	295.1	294.98	295.26	294.79	294.98
Sensor output	294.45	295.45	295.25	296.05	295.35	296.05	296.15	295.95	295.45	296.35	296.25
Increasing temperature	Done										
Error %	0.19	0.17	0.13	0.35	0.09	0.35	0.36	0.33	0.06	0.53	0.43
Average Error %	0.27										

As it is shown in table 2-1, all the sensors have errors less than 0.6%, which is less than indicated accuracy of the sensors (±1 in 298.15 K or 0.67%) on the LM35 manual [16].

Process C; this process contains the following procedures:

1. Cleaning the surfaces, which are the locations of the sensors on the aluminum models (the position of each sensor is illustrated on table 2-2 and figure 2-23).

Table 2-2.Position of sensors on the aluminum specimens (Dimensions in mm)

	Model 1	Model 2	Model 3	Model 1	Model 2	Model 3
	Dimensions from the bottom of the model			Dimensions from thetop of the model		
Top sensor	76.2	38.1	76.2	50.8	25.4	25.4
Middle sensor	50.8	25.4	50.8	76.2	38.1	50.8
Bottom sensor	27.94	15.24	27.94	99.06	48.26	27.94
Inside sensor	7.11	3.81		119.89	59.69	

2. Mixing 10 percent of catalyst with 100 percent of resin (OMEGABOND "200"), which is used to stick the sensors on any surface.
3. Applying the mixed compound on the surface of the sensors and putting them on their specific positions on the models.

4. Baking the mixed thermal conductive compounds by maintaining the models inside an oven at temperature of 125°C for at least 6 hours to permanently stabilize the sensors on their position.

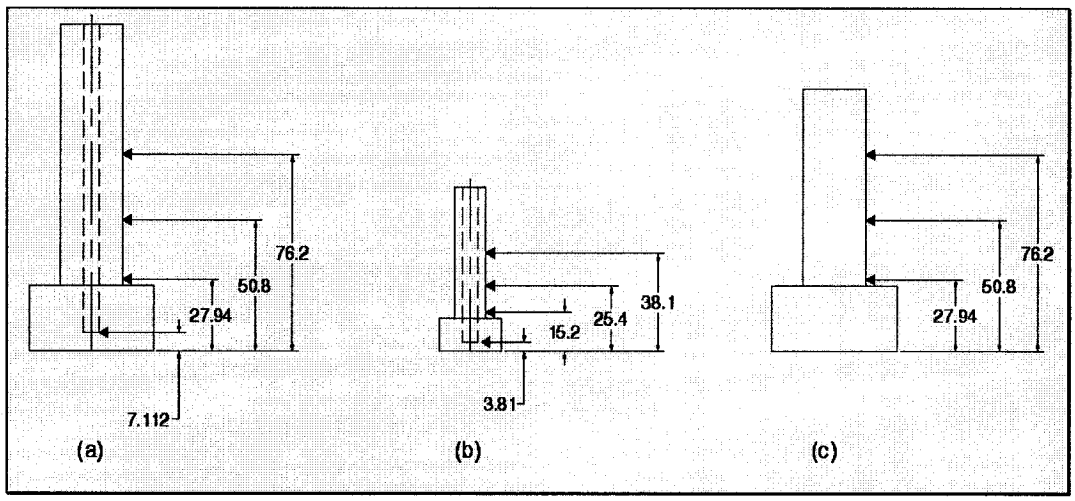

Figure 2-23. Position of sensors in the aluminum specimens (a) Specimen 1, (b) Specimen 2, (c) Specimen 3 (Dimensions in mm)

Process D; this process contains the following procedures:

1. Cleaning the surface of the models.
2. Applying the "200 Catalyst-C", which used with certified M-Bond adhesive, to enable the adhesion of the cement to the aluminum surface.
3. Applying the "Cyanoacrylate Adhesive" on the surface (this is a special adhesive for sticking the Soldier terminals on any surface).
4. Putting the "Soldier terminal" on the adhesive compound.
5. Soldiering the output wires of each sensor to the terminal and connecting the other side of the wires from the soldier terminals to the Lab View software terminal (Data Acquisition System). The amount of soldered terminals is equal to the number of sensors plus two terminals for the opposite and reference

connections. A schematic of the soldiering terminals for three sensors is illustrated on figure 2-24.

The colors of the connection wires from the models to the Lab View terminal are used to identify that which output is from which sensors. These colors are illustrated on table 2-3.

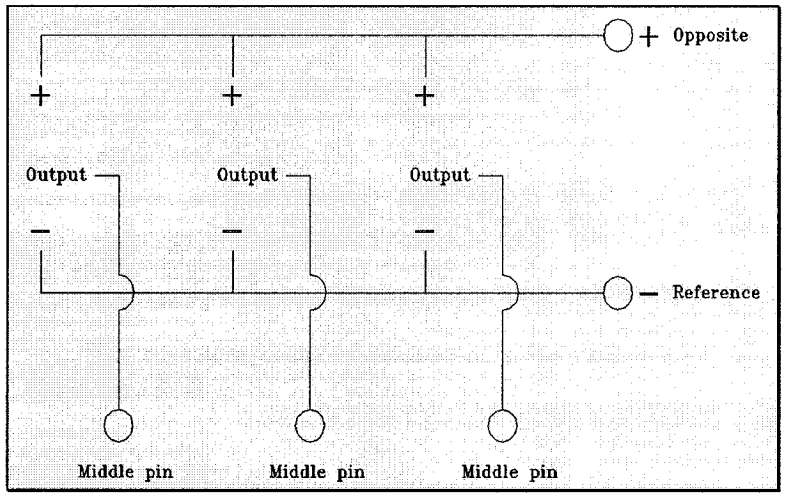

Figure 2-24. Schematic of soldering terminals for three sensors

Table 2-3. Colors of the output connections from the "solder terminals" to the Lab View terminal

Red	Black	White	Blue	Green	Brown
Opposite	Reference	Top sensor	Middle sensor	Bottom sensor	Inside sensor
		0	1	2	3
Positive	Reference	Out put channel in Lab View software			

2.3.2. Experimental Process

The experiments started with initiating the wind tunnel. Meanwhile, the flow velocity is fixed to the required value for the test (in these experiments, the set points for the flow velocity are 5, 9, 17 and 25m/s). After a while, the hotplate is plugged into the power supply and the set point of the temperature controller is fixed to a set value (set points are

40, 60, 80 and 100°C). The surface temperature of the hotplate is increasing until its temperature reaches the set-point value. Further, the power supply is automatically turning on and off to keep the surface temperature uniform and constant through the experiments. The output signals of the sensors are transferred to the Lab-View software every three seconds (which is dependent on the setting of the Lab-View software one is able to change the recording time). These results are saved for different flow velocities and two different orientations of the models (0° and 45° with respect to the direction of the flow) on different surface temperatures of the hotplate. The experimental results are divided into 8 different alternatives for each model. In each alternative, four different velocities of 5, 9, 17 and 25 m/s are applied on the flowing air. This means that for each alternative there are four categories of results on each specific surface temperature of the hotplate. The matrix of experiments is described in table 2-4.

Table 2-4. The alternatives for experimental results

Model 1*	Model 2*	Model 3*
Th=40°C, α=0°	Th=40°C, α=0°	Th=40°C, α=0°
Th=60°C, α=0°	Th=60°C, α=0°	Th=60°C, α=0°
Th=80°C, α=0°	Th=80°C, α=0°	Th=80°C, α=0°
Th=100°C, α=0°	Th=100°C, α=0°	Th=100°C, α=0°
Th=40°C, α=45°	Th=40°C, α=45°	Th=40°C, α=45°
Th=60°C, α=45°	Th=60°C, α=45°	Th=60°C, α=45°
Th=80°C, α=45°	Th=80°C, α=45°	Th=80°C, α=45°
Th=100°C, α=45°	Th=100°C, α=45°	Th=100°C, α=45°

*a is the orientation angle of models in compare with the flow

In each experiment, the results are saved from the beginning of the cycle when the temperature of the hot plate is starting from a temperature less than the set point and increase to the set point and kept for more than 7 minutes, which the absolute temperature does not have more than 0.1% variation and the steady state condition begins. Then after

each experiment, the power supply into the hotplate is disconnected manually until the surface of the hotplate is cooled down to a temperature less than the set point temperature. After changing the velocity of the flowing air, the hotplate is again connected to the power supply for the next experiment. This is the reason that for each experiment, the temperature is starting from some specific points for each sensor and increase to reach their steady state condition.

2.4. Summary

According to the investigations in this chapter, it can be concluded that:

- For $Re<5.6\times10^3$, the value of N in equation 2.8 is equal to 0.5 and consequently the film temperature is equal to the average of base temperature adding with the temperature of flowing fluid for low Reynolds numbers.
- For $Re\geq5.6\times10^3$, the value of N in equation 2.8 is found from figures 2-14, 2-15 and 2-16 for air as the flowing fluid.
- For low Reynolds numbers ($Re<5.6\times10^3$) the average of flowing fluid temperature adding with the base temperature is a conservative value as an input for boundary conditions in the ANSYS simulations to get less than 10% error in compare with experiments.

CHAPTER 3

Experimental and FEM Calibration

3.1. Experimental Results

In this section the experimental results of three aluminum specimens, which are built in three different scales and described in chapter two are presented. In each experiment the aluminum models are installed on the surface of a hotplate. The power supply is controlled by an E5CN temperature controller [15]. This controller controls the surface temperature of the hotplate and adjusts it with the set point value. The bases of the models are insulated by wrapping an insulator around each base and the rest of the models are in contact with the flowing air with different velocities inside a wind tunnel.

The temperature distribution is sensed by LM35 temperature sensors [16] on different locations of each model. The results are based on applying different velocities of the flowing air at different constant temperatures of the hotplate.

After any experiment the power supply was disconnected until the temperature of the hotplate cooled down and reached to the room temperature. Then the next experiment starts from this point by connecting the power supply until the output results reach to a steady state value (after 7 minutes), where absolute temperature variation is less than 0.1%.

Some of the experimental results are illustrated in figures 3-1 through 3-6. In these results the y-axis represents the normalized temperature ratio (θ), which is described in equation 3-1:

$$\theta = \frac{T_o - T_f}{T_h - T_f} \tag{3-1}$$

In this equation;

T_o (°C) is the output temperature of each sensor, T_f (°C) is the temperature of the flowing fluid, T_h (°C) is the temperature of the hot plate and θ is the normalized temperature ratio.

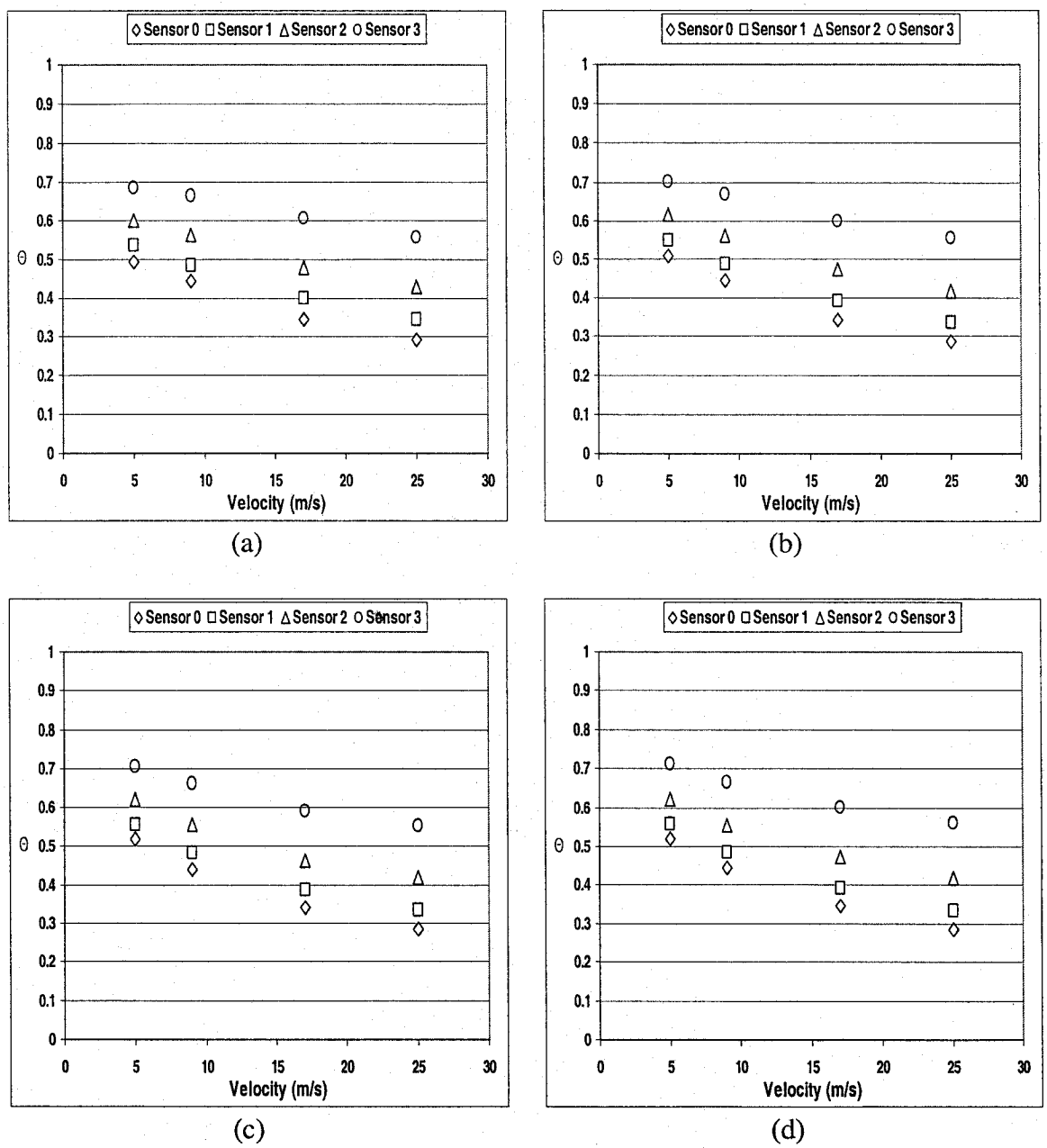

Figure 3-1. Normalized temperature ratio versus velocity in specimen 1 for zero orientation angle (α=0°) at (a) T_h=40°C, (b) T_h=60°C, (c) T_h=80°C, (d) T_h=100°C

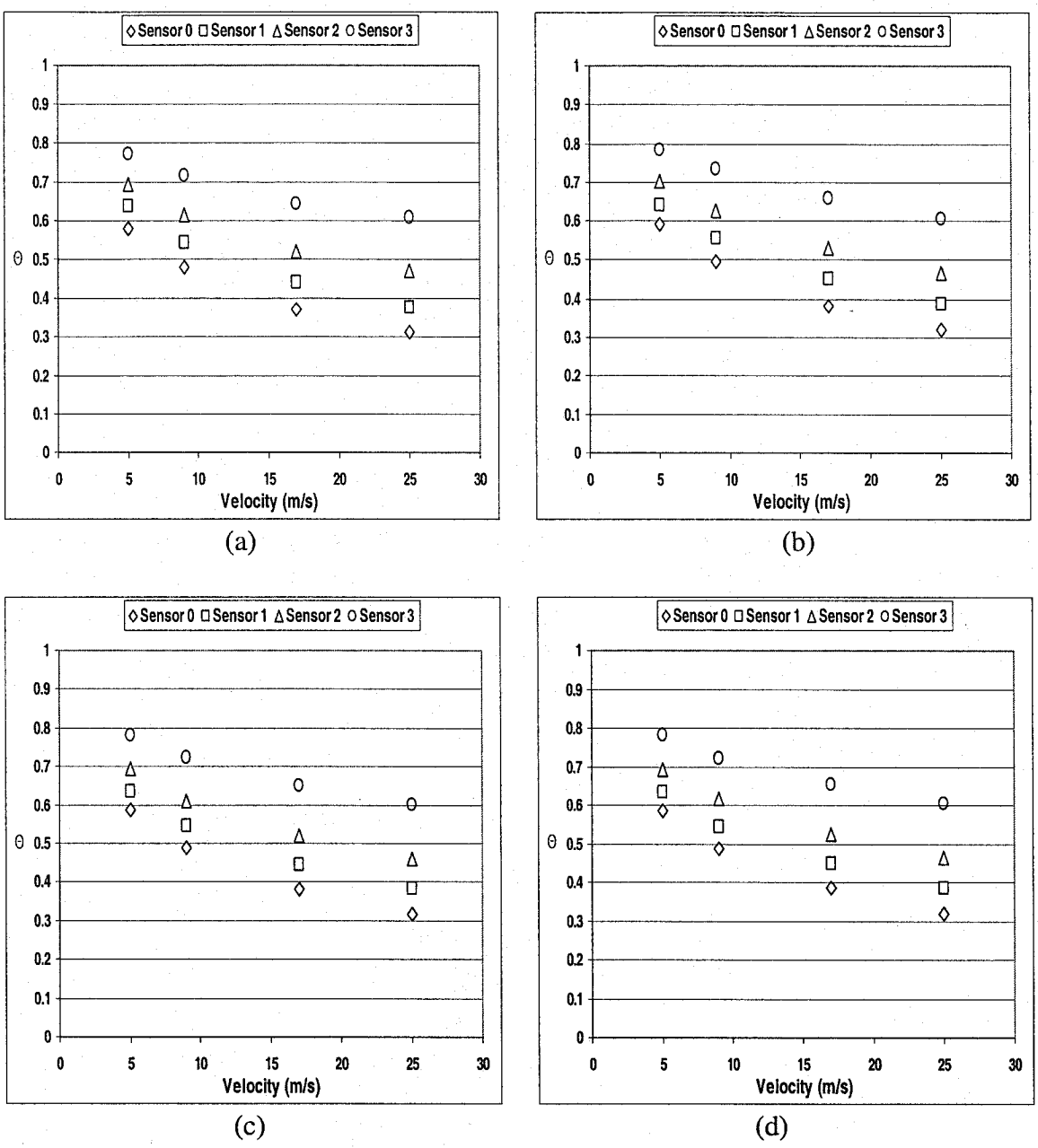

Figure 3-2. Normalized temperature ratio versus velocity in specimen 1 for 45° orientation angle (α=45°) at (a) T_h =40°C, (b) T_h =60°C, (c) T_h =80°C, (d) T_h =100°C

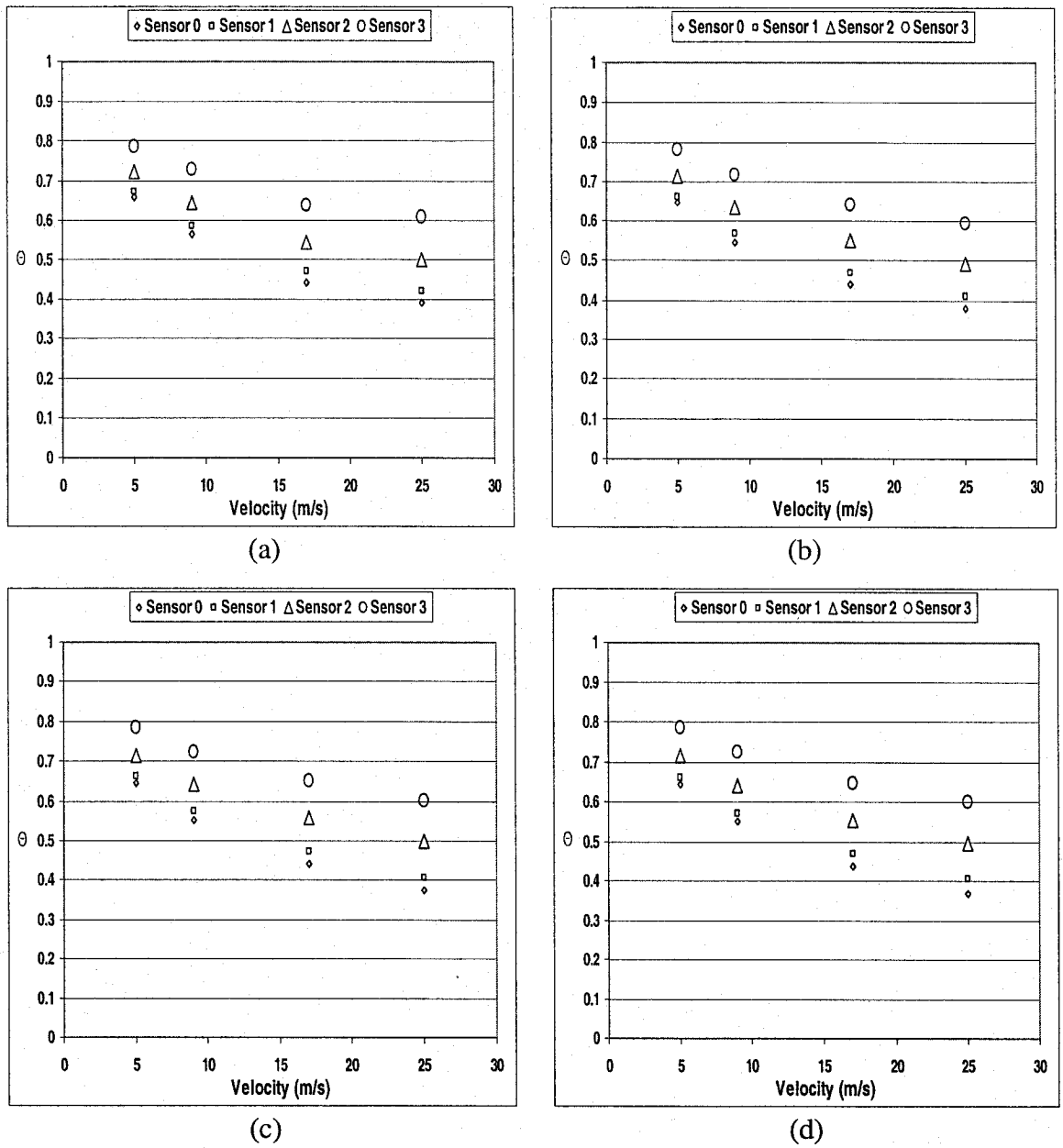

Figure 3-3. Normalized temperature ratio versus velocity in specimen 2 for zero orientation angle (α=0°) at (a) T_h=40°C, (b) T_h=60°C, (c) T_h=80°C, (d) T_h=100°C

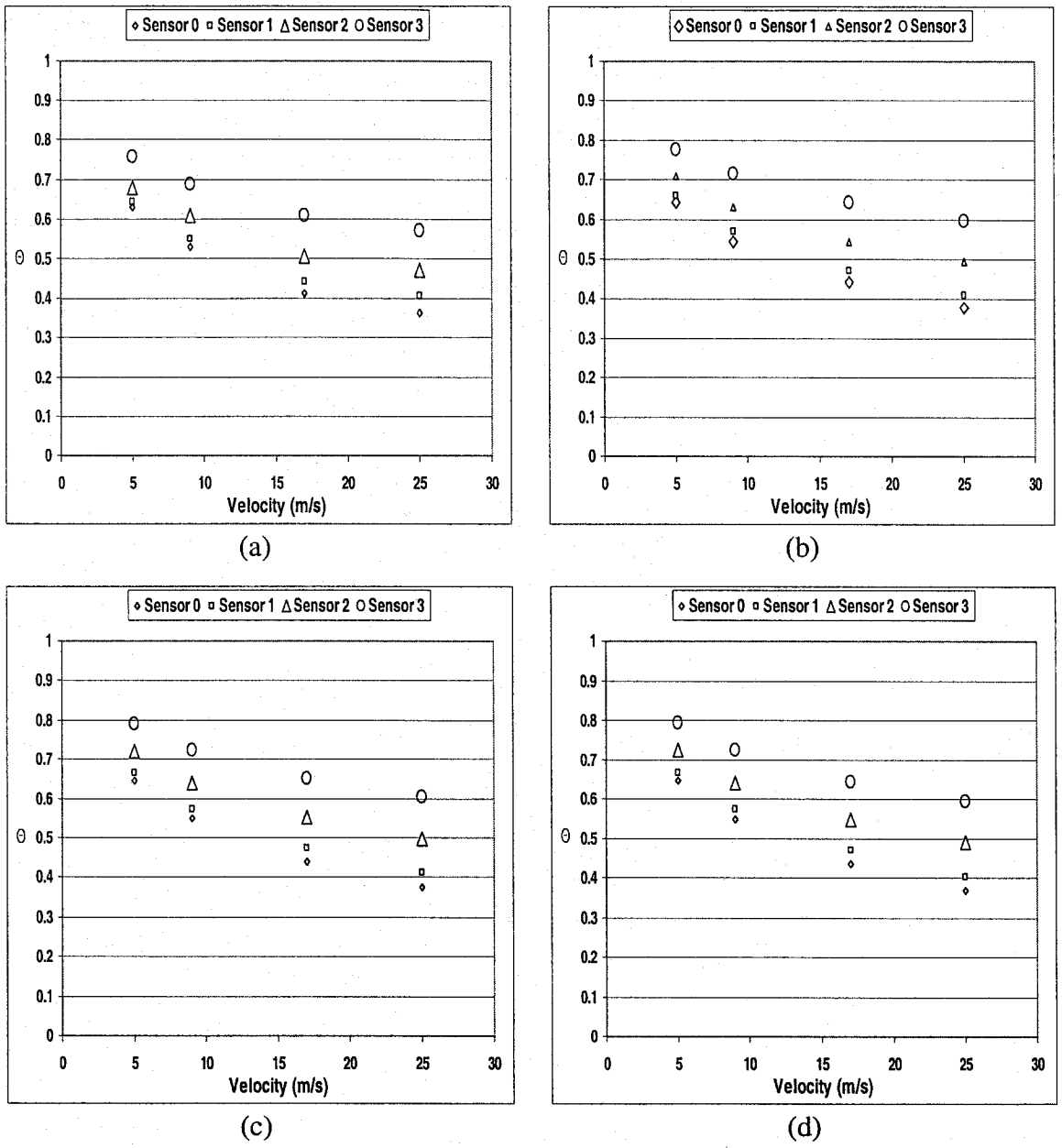

Figure 3-4. Normalized temperature ratio versus velocity in specimen 2 for 45° orientation angle (α=45°) at (a) T_h=40°C, (b) T_h=60°C, (c) T_h=80°C, (d) T_h=100°C

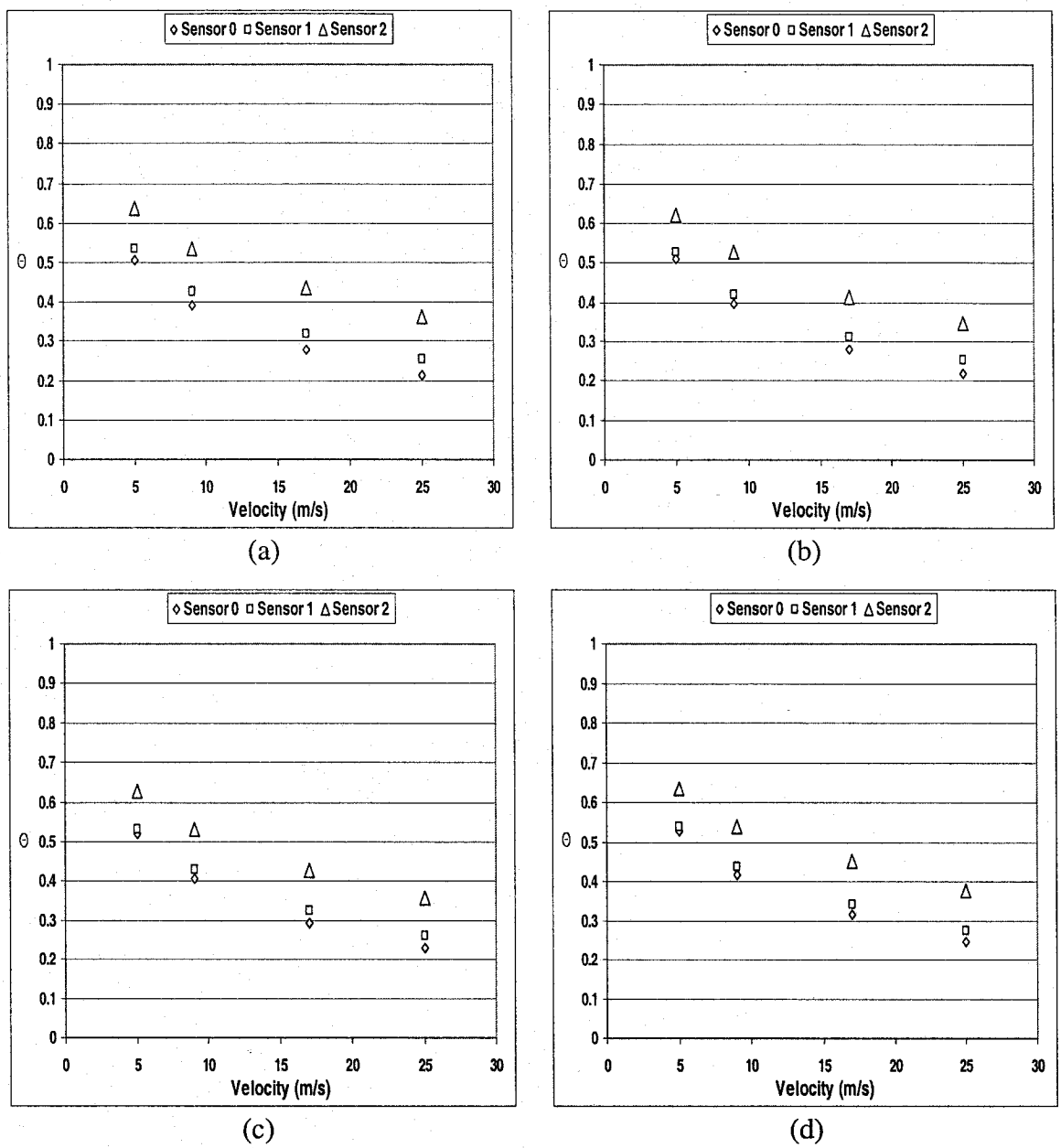

Figure 3-5. Normalized temperature ratio versus velocity in specimen 3 for zero orientation angle (α=0°) at (a) T_h=40°C, (b) T_h=60°C, (c) T_h=80°C, (d) T_h=100°C

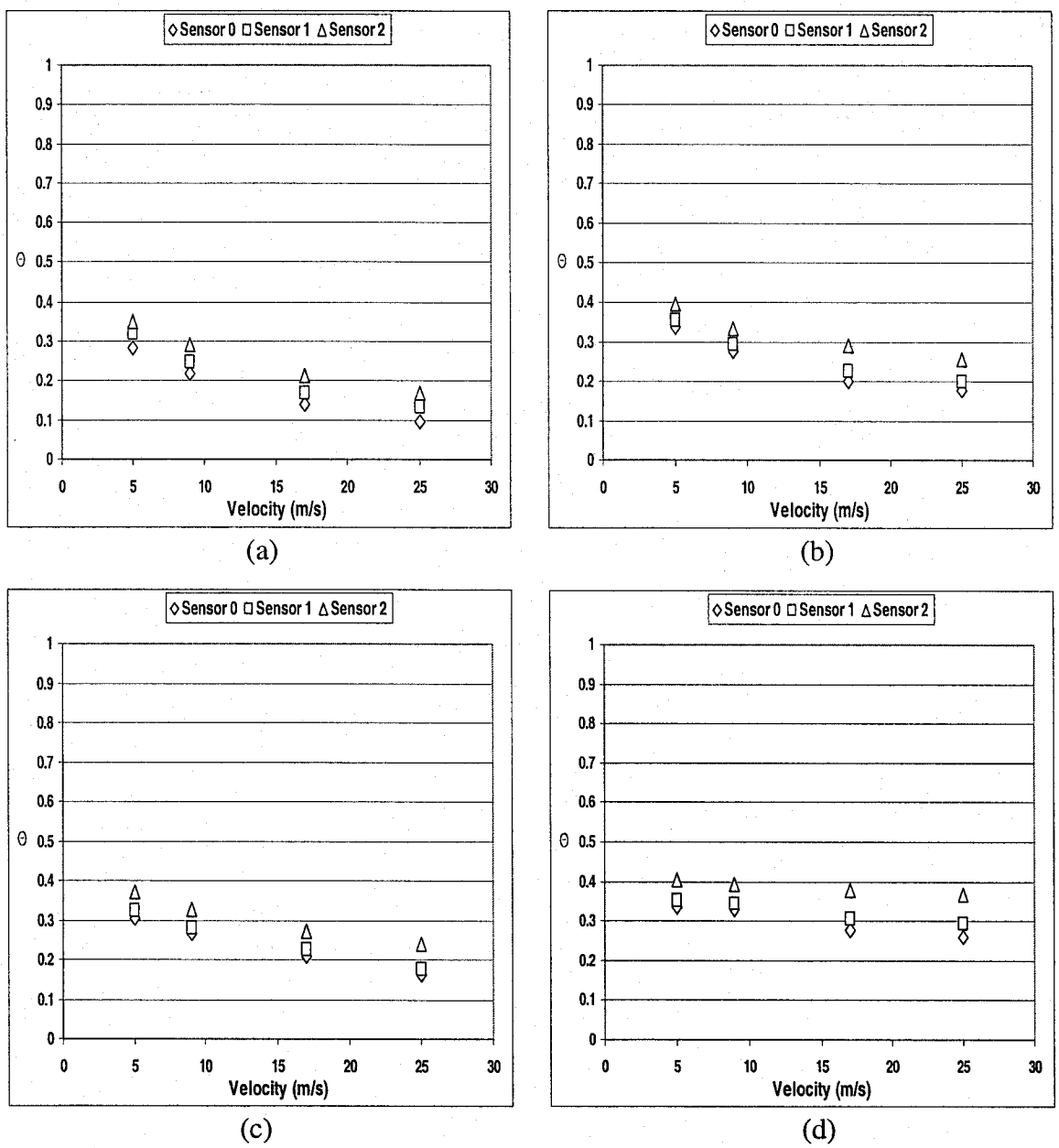

Figure 3-6. Normalized temperature ratio versus velocity in specimen 3 for 45° orientation angle (α=45°) at (a) T_h =40°C, (b) T_h =60°C, (c) T_h =80°C, (d) T_h =100°C

3.2. ANSYS Simulation Results

In this section thermal ANSYS simulation results of three aluminum specimens described in chapter two, are presented.

The advantages of ANSYS are:

- Engineers are able to synthesize any device with good accuracy and perform optimization before the product is fabricated.
- This software is user friendly and flexible.
- The software enables to perform both structural and heat transfer simulations within the same model.

The ANSYS results for all models are illustrated on figures 3-7 through 3-12. In the first and second models, the Normalized temperature ratio versus velocity for some velocities is too close together. The reason is that the temperature coefficient factor (N), which is introduced in part 2.2.3 and used for these simulations, is equal to 0.5 for conditions with $Re<5.6\times10^3$ and consequently the film temperatures (calculated from equation 2-11) has the same value for these cases as a boundary condition. The same story is happening for situations with $Re\geq5.6\times10^3$ by considering temperature coefficient factor (N) equal to 0.4. In the third model the temperature coefficient factor (N) is considered from the graphs in figures 2-17 through 2-19 for $Re\geq5.6\times10^3$ and for $Re<5.6\times10^3$, is considered equal to 0.5. The reason for these considerations is to get more precise result from ANSYS to get less than 10% variation between the simulations and experimental results.

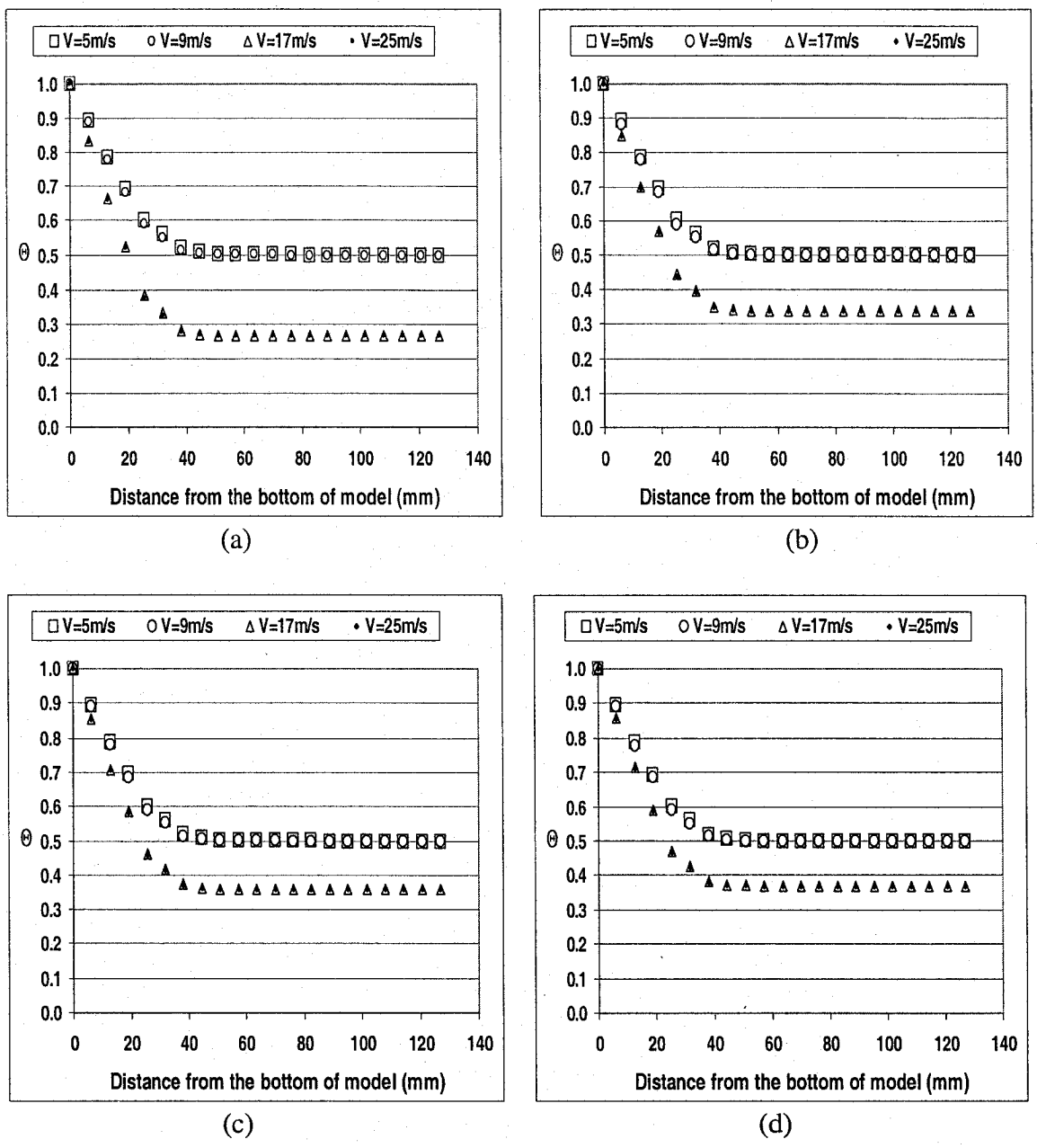

Figure 3-7. Normalized temperature ratio distribution in model 1 for α=0° at V=5, 9, 17 and 25m/s
(a) Th=40°C, (b) Th=60°C, (c) Th=80°C, (d) Th=100°C

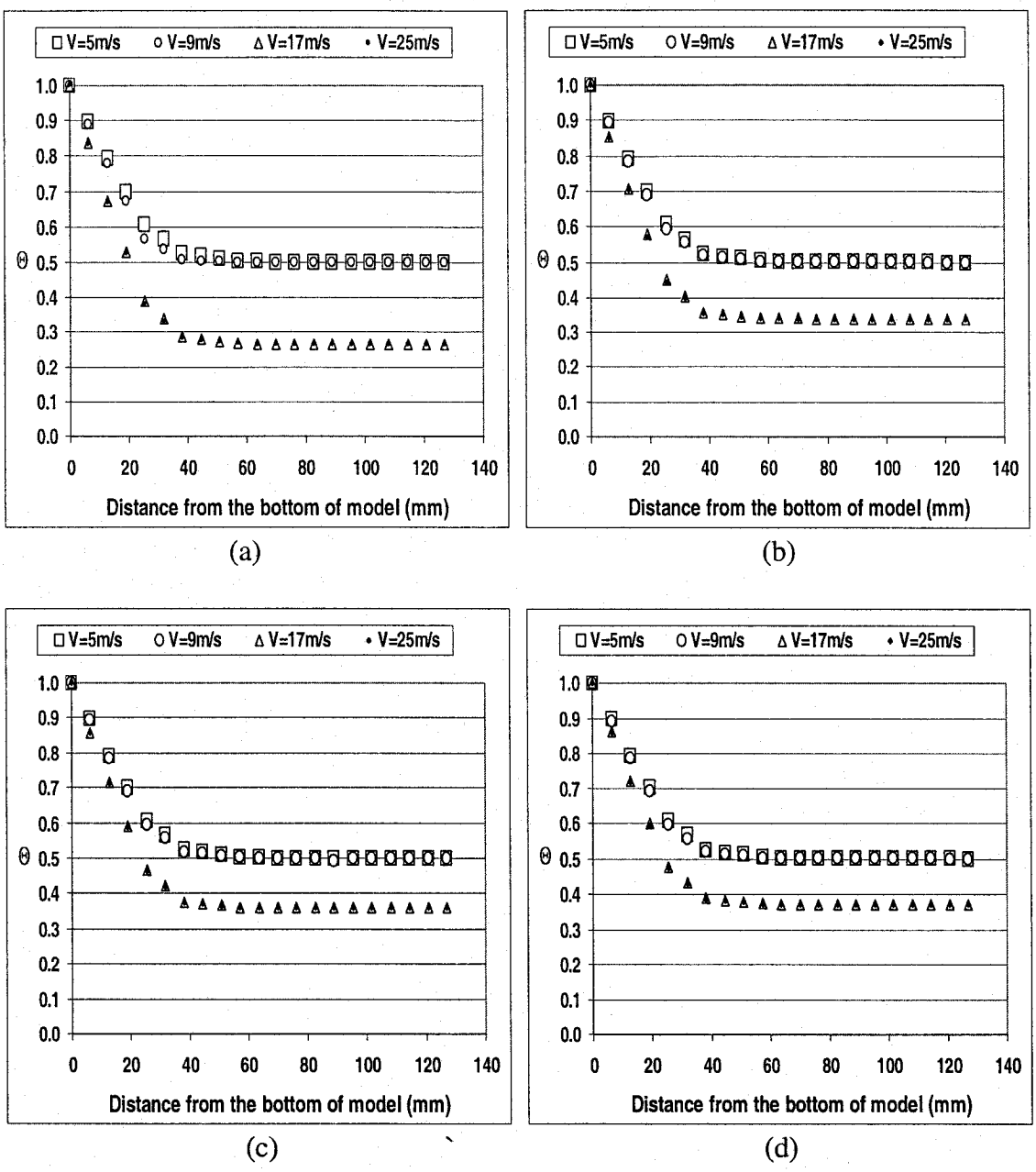

Figure 3-8. Normalized temperature ratio distribution in model 1 for α=45° at V=5, 9, 17 and 25m/s (a) Th=40°C, (b) Th=60°C, (c) Th=80°C, (d) Th=100°C

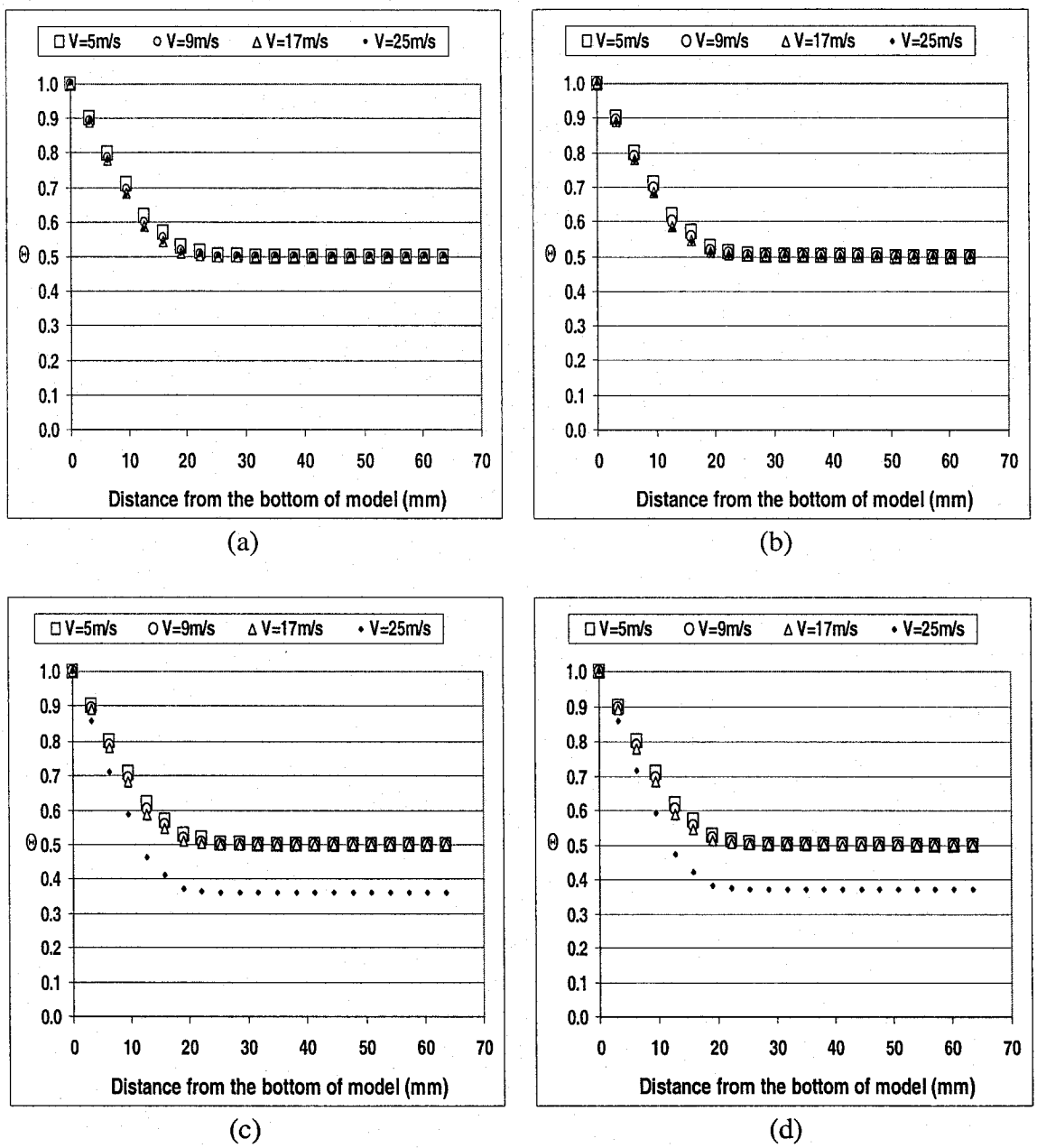

Figure 3-9. Normalized temperature ratio distribution in model 2 for α=0° at V=5, 9, 17 and 25m/s
(a) Th=40°C, (b) Th=60°C, (c) Th=80°C, (d) Th=100°C

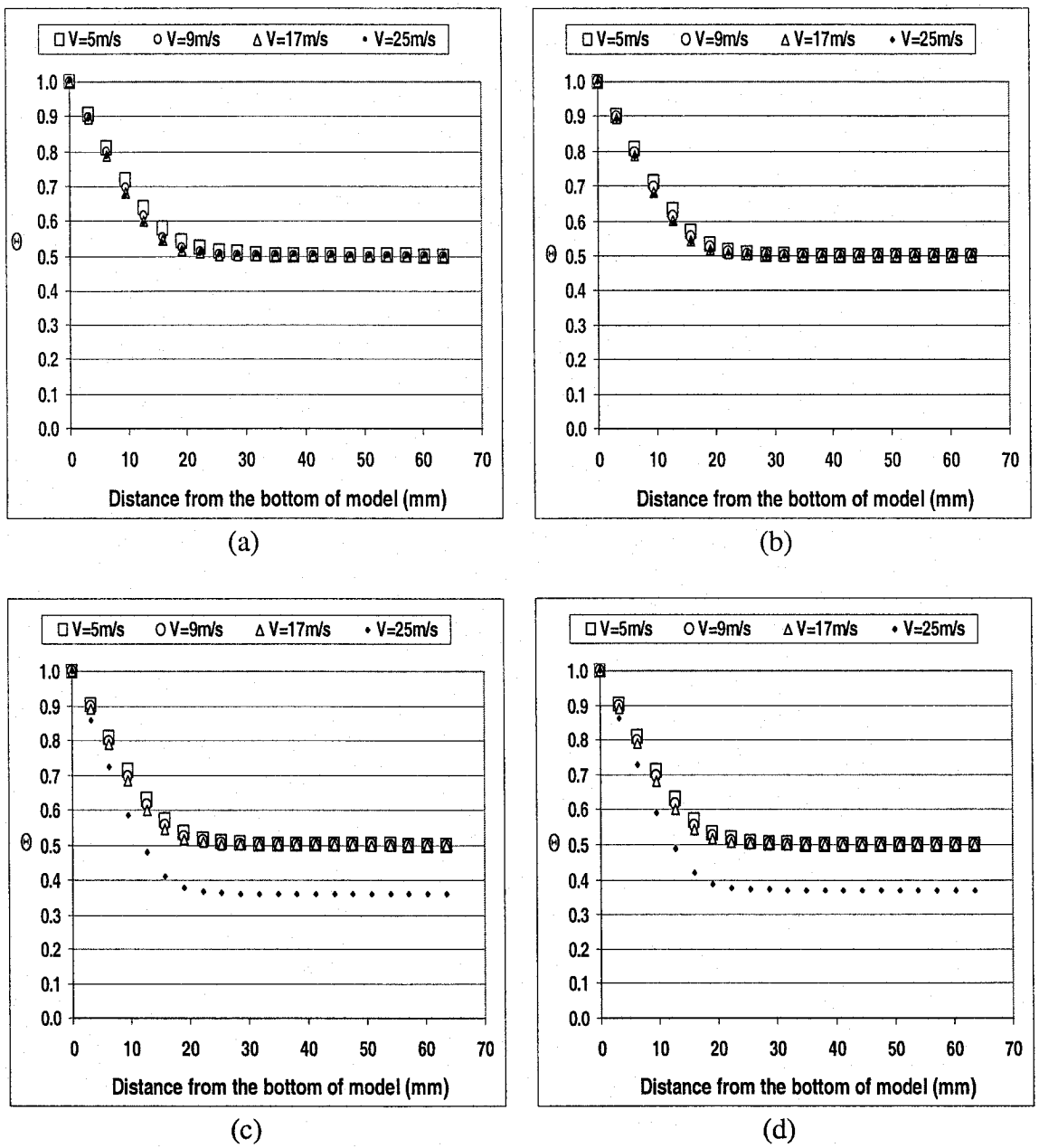

Figure 3-10. Normalized temperature ratio distribution in model 2 for α=45° at V=5, 9, 17 and 25m/s (a) Th=40°C, (b) Th=60°C, (c) Th=80°C, (d) Th=100°C

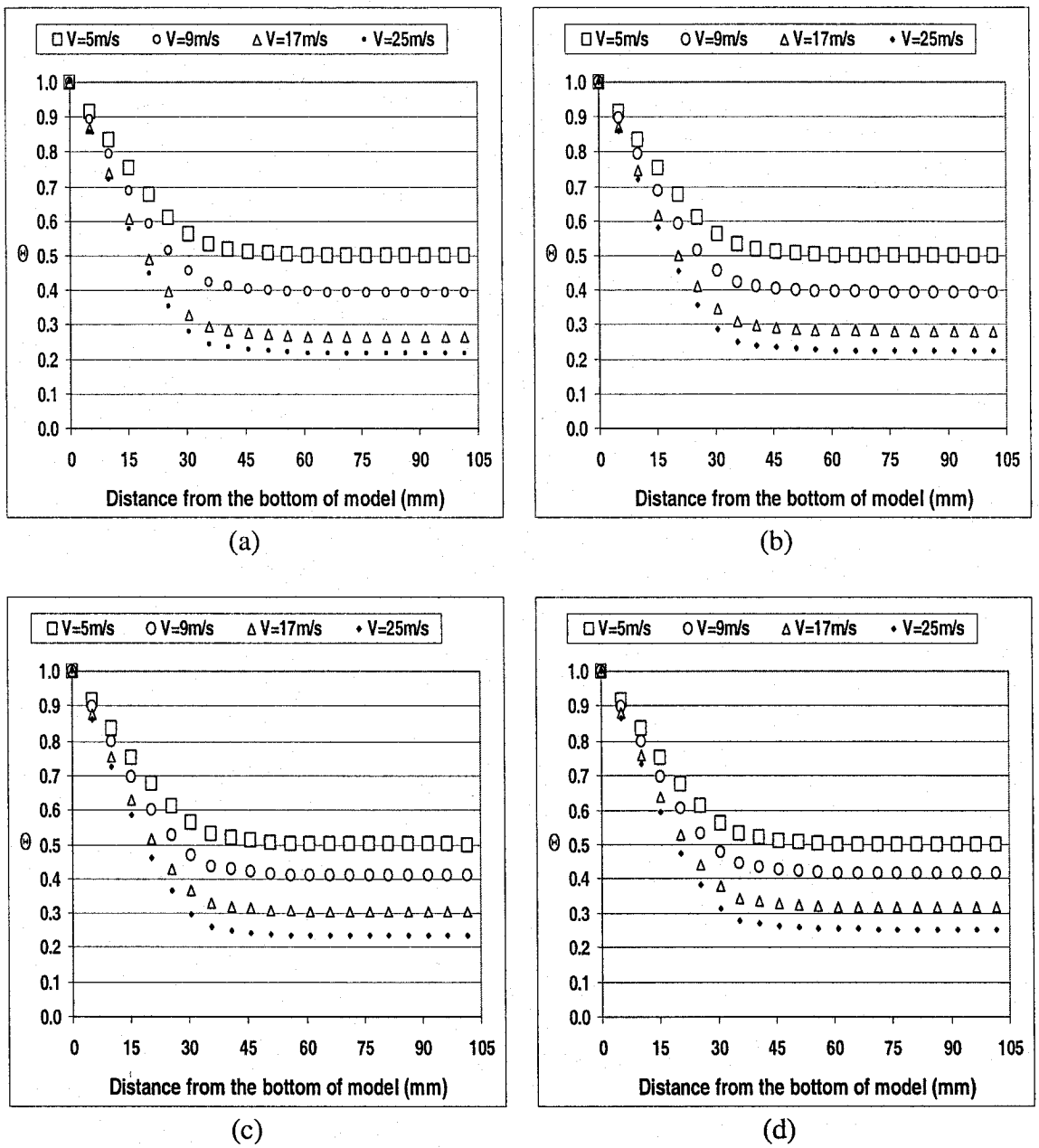

Figure 3-11. Normalized temperature ratio distribution in model 3 for α=0° at V=5, 9, 17 and 25m/s (a) Th=40°C, (b) Th=60°C, (c) Th=80°C, (d) Th=100°C

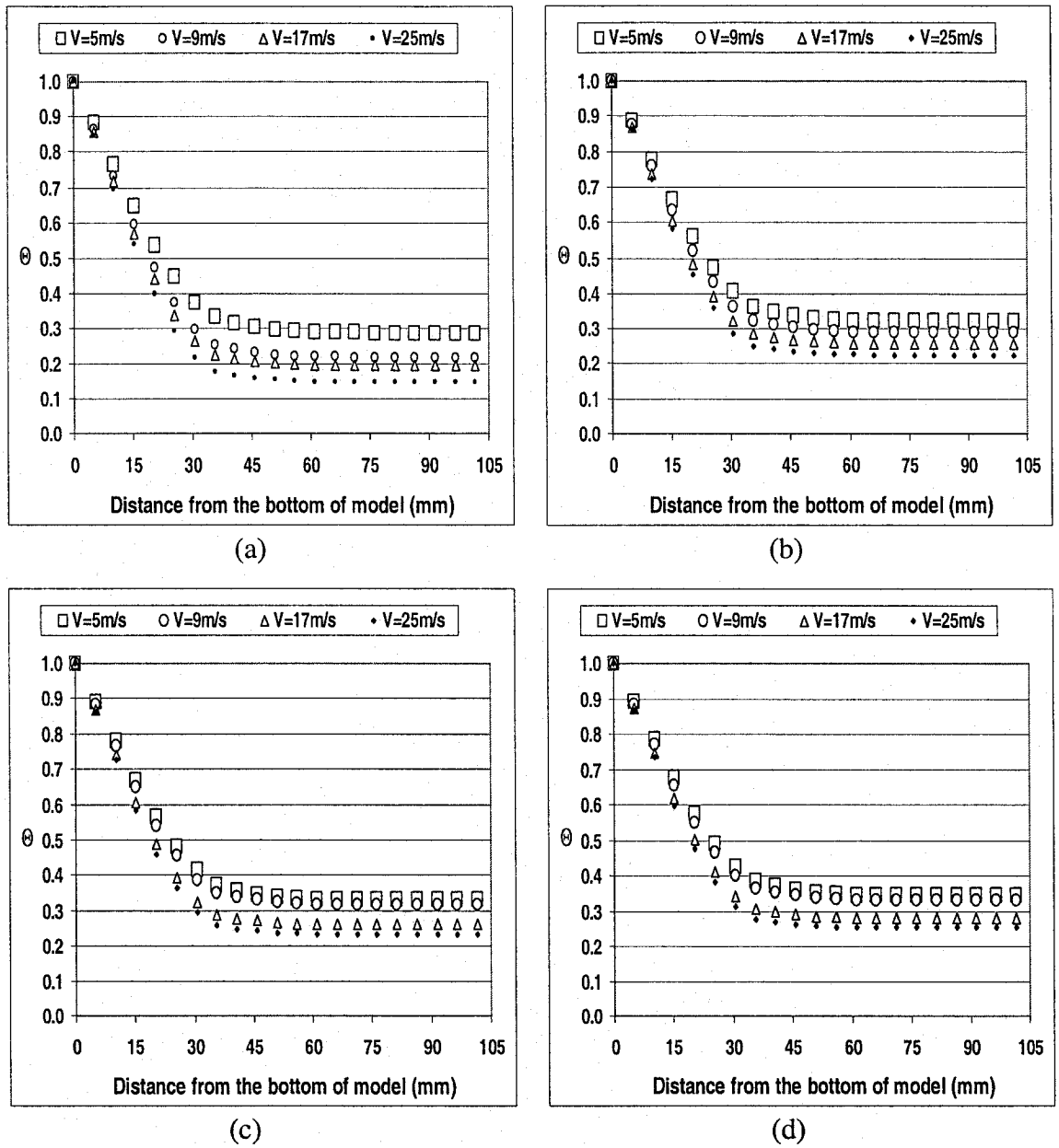

Figure 3-12. Normalized temperature ratio distribution in model 3 for α=45° at V=5, 9, 17 and 25m/s (a) Th=40°C, (b) Th=60°C, (c) Th=80°C, (d) Th=100°C

Experimental and simulation results are compared on the same graphs from figures 3-12 through 3-18 on the locations that sensors have been installed on the models. In these results the y-axis represents the normalized ratio (Ψ), which is described in equation 3-2:

$$\psi = \frac{T_s}{T_h} \tag{3-2}$$

In this equation; T_s (°C) is the temperature based on simulation result, T_h (°C) is the temperature of the hot plate and Ψ is the normalized ratio.

The amount of transferred thermal energy by conduction from the base of any specimen can be calculated from equation 3-3:

$$Q = k \cdot A \cdot \frac{T_h - T_o}{x} \tag{3-3}$$

By mixing this equation and equation 3-1, the relation between the transferred thermal energy by conduction with the normalized temperature ratio (θ) can be found as:

$$Q = k \cdot A \cdot \frac{(T_h - T_f) \cdot (1 - \theta)}{x} \tag{3-4}$$

In this equation;

T_f (°C) is the temperature of the flowing fluid, T_h (°C) is the temperature of the base on each specimen, k (W/m.K) is the conduction coefficient of the aluminum specimens, A (m^2) is the cross area of each pin on the specimens, x (m) is the distance from the base to

the position of the sensors and Q (W) is the amount of transferred thermal energy by conduction through each specimen. This equation will be later used in part 3.3.

In the following graphs, "Exp." and "Sim.", are representative of "Experimental" and "Simulation".

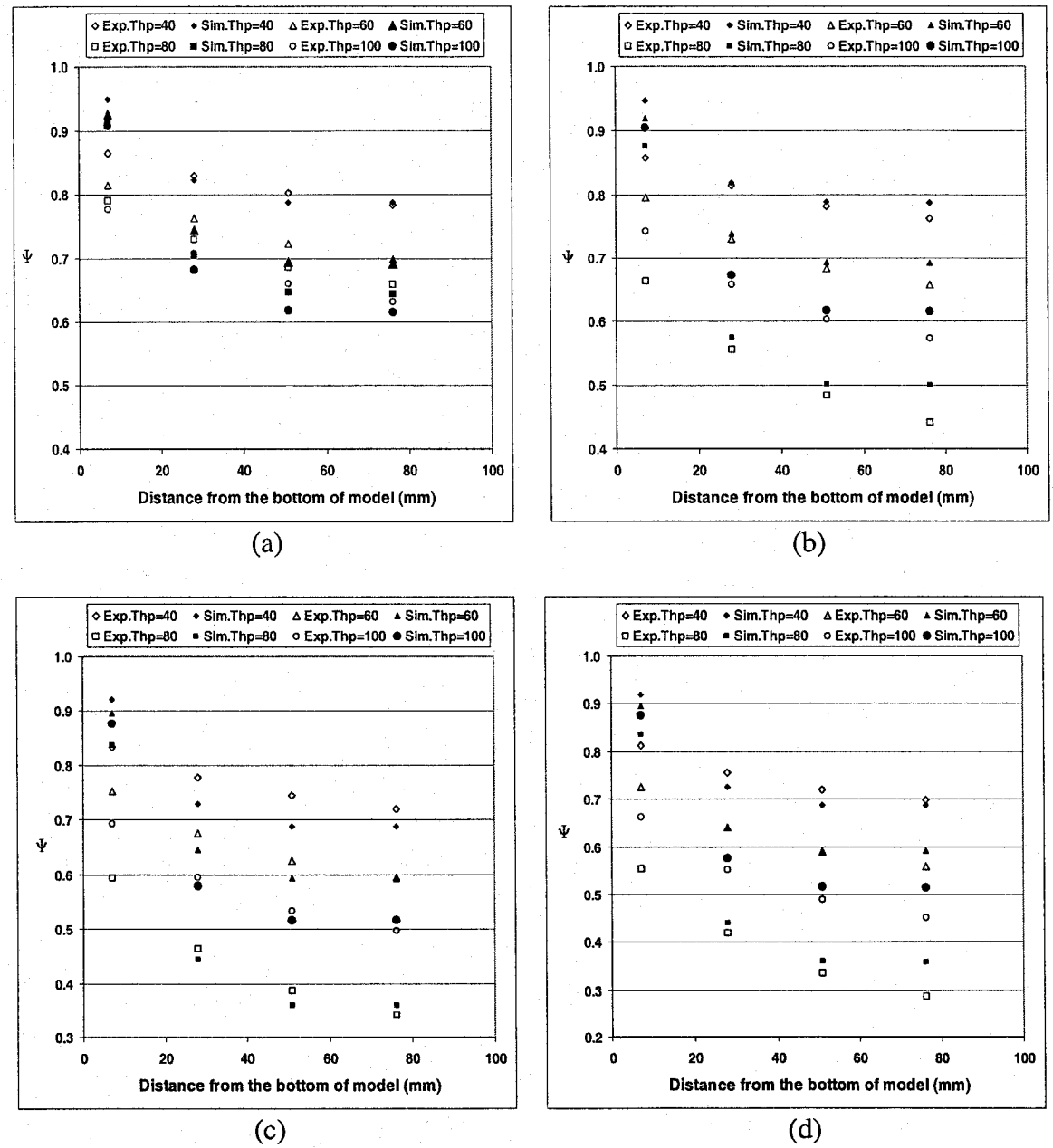

Figure 3-13. Comparison of the experimental results with the simulation results at different temperatures of hot plate in model 1 for α=0° (a) V=5 m/s, (b) V=9m/s, (c) V=17m/s, (d) V=25m/s

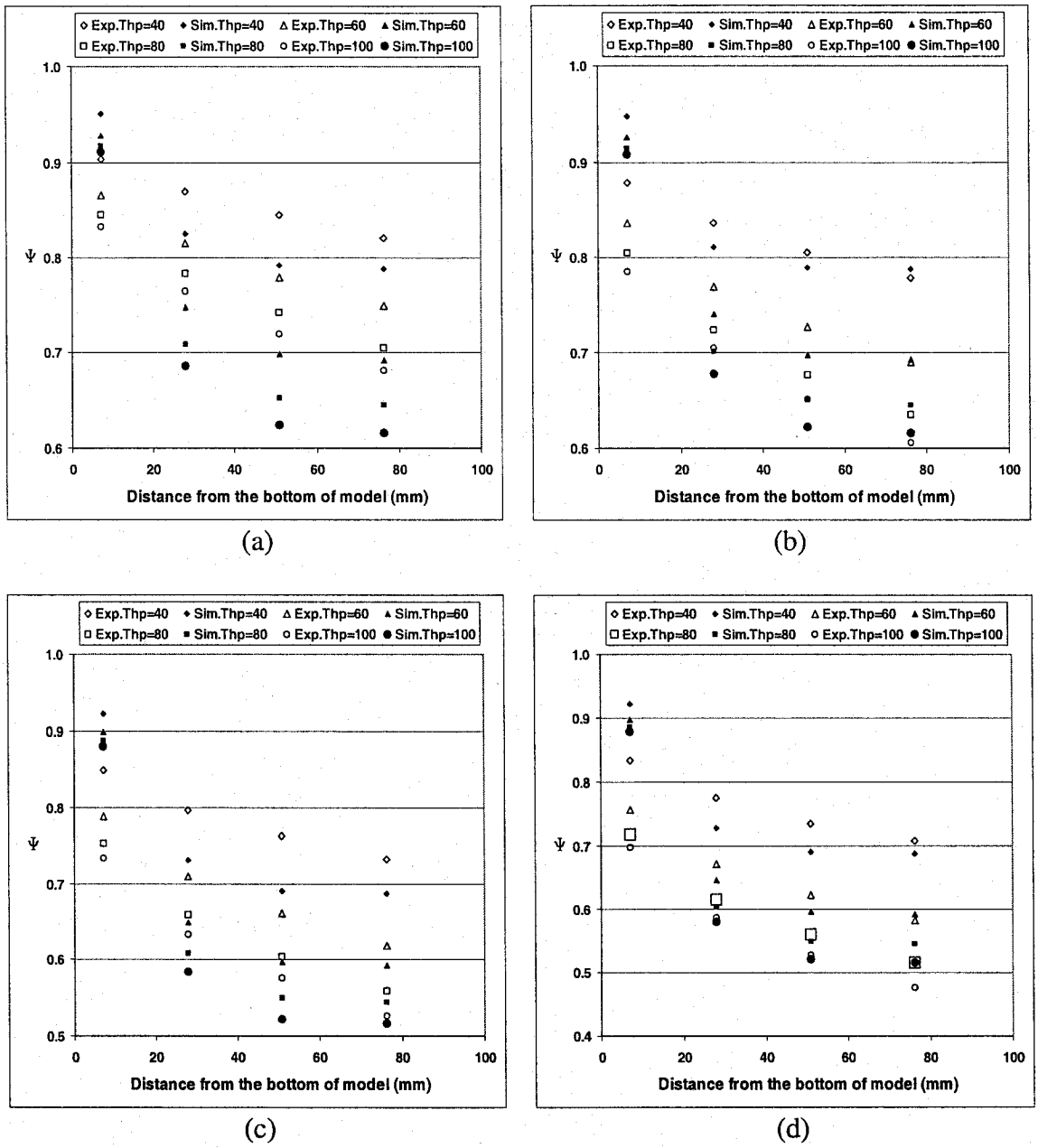

Figure 3-14. Comparison of the experimental results with the simulation results at different temperatures of hot plate in model 1 for α=45° (a) V=5 m/s, (b) V=9m/s, (c) V=17m/s, (d) V=25m/s

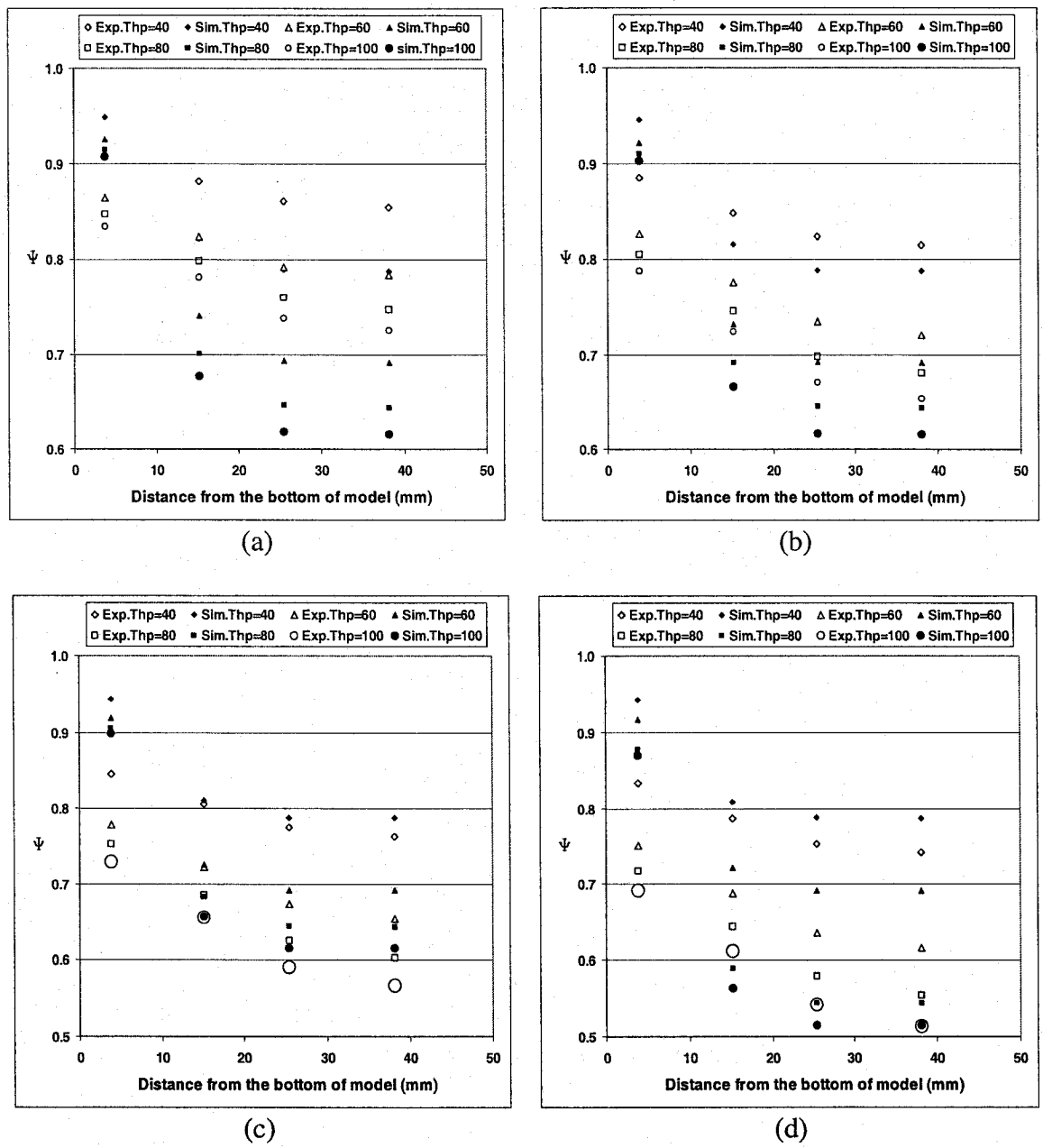

Figure 3-15. Comparison of the experimental results with the simulation results at different temperatures of hot plate in model 2 for α=0° (a) V=5 m/s, (b) V=9m/s, (c) V=17m/s, (d) V=25m/s

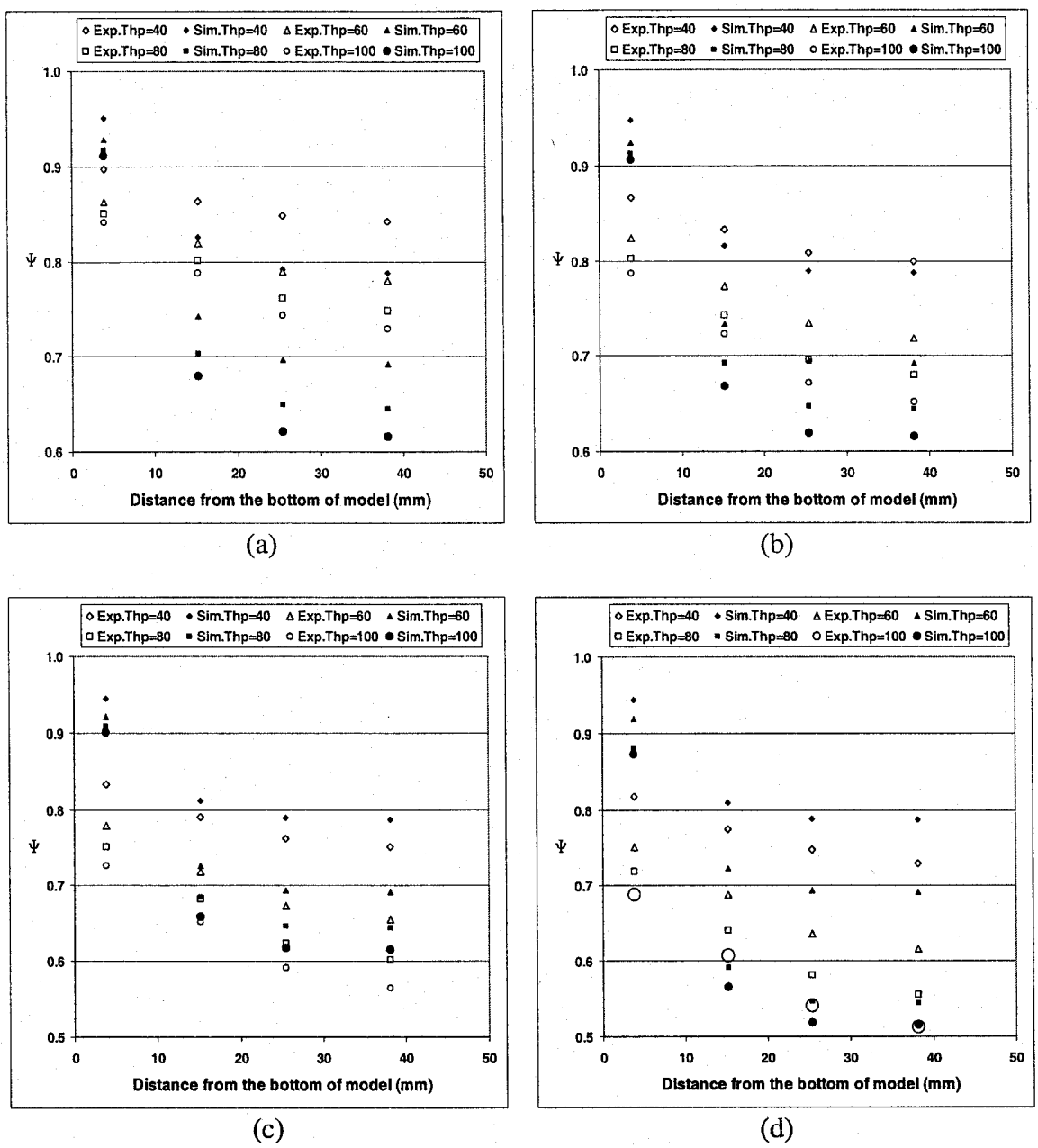

Figure 3-16. Comparison of the experimental results with the simulation results at different temperatures of hot plate in model 2 for α=45° (a) V=5 m/s, (b) V=9m/s, (c) V=17m/s, (d) V=25m/s

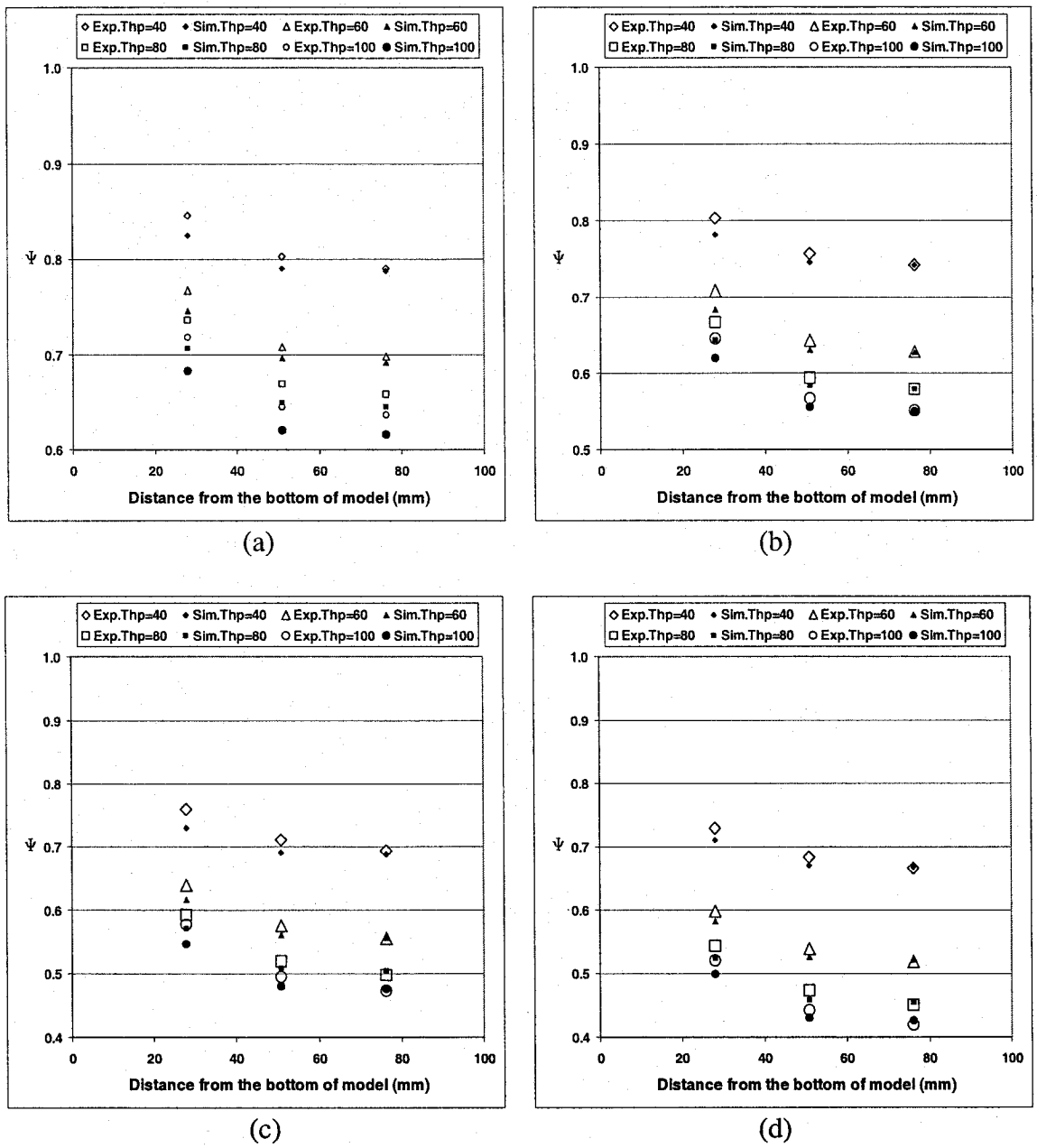

Figure 3-17. Comparison of the experimental results with the simulation results at different temperatures of hot plate in model 3 for α=0° (a) V=5 m/s, (b) V=9m/s, (c) V=17m/s, (d) V=25m/s

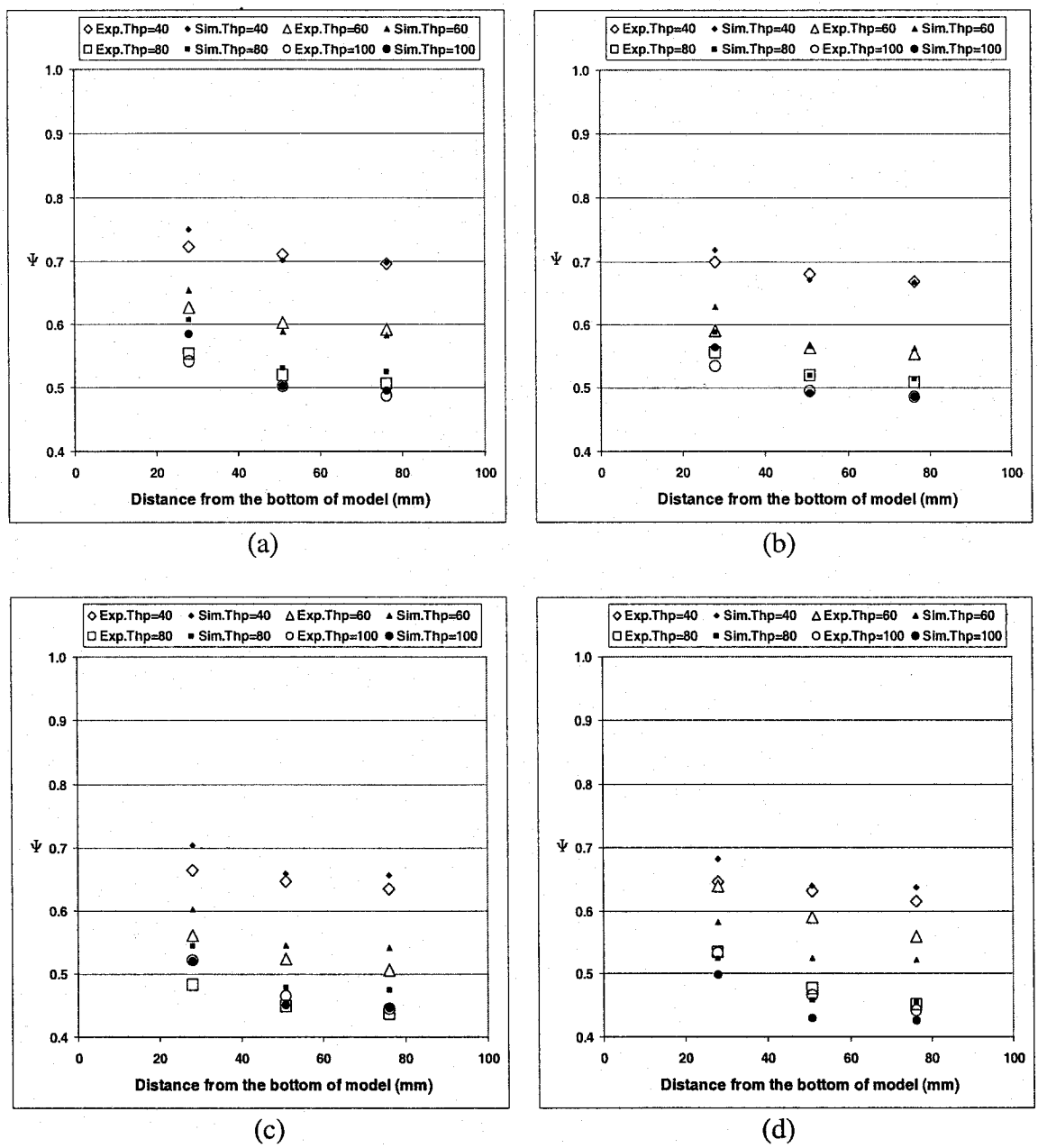

Figure 3-18. Comparison of the experimental results with the simulation results at different temperatures of hot plate in model 3 for α=45° (a) V=5 m/s, (b) V=9m/s, (c) V=17m/s, (d) V=25m/s

3.3. Comparison of the Results

By studying the experimental results of the first specimen (figures 3-1 and 3-2) at different orientation angles, the following observations can be stated:

- By increasing the velocity the amount of normalized temperature ratio (θ) is decreasing linearly on each sensor for both orientation angles of α=0° and α=45°.
- The rate of this linear reduction for α=45° is higher than α=0°.
- For velocity of 5m/s and all temperatures of the hotplate and α=45°, the detected temperature in all of the sensors is 6-10% higher than α=0°.
- For velocity of 9m/s and all temperatures of the hotplate and α=45°, the detected temperature in all of the sensors is 4-7% higher than α=0°.
- For velocity of 17m/s and all temperatures of the hotplate and α=45°, the detected temperature in all of the sensors is 3-6% higher than α=0°.
- For velocity of 25m/s and all temperatures of the hotplate and α=45°, the detected temperature in all of the sensors is 2-5% higher than α=0°.
- Lower the flow speed and the temperature of the hotplate, higher is the variation of the normalized temperature ratio (θ) between α=0° and α=45°.
- The amount of transferred thermal energy (can be estimated by equation 3-4) through specimen 1 in the case of α=0°, which is proportional to the normalized temperature ratio (1-θ), for velocities of 5, 9, 17 and 25m/s is 46%, 56%, 58% and 56% respectively higher than the case of α=45° in average.

The experimental results, which are illustrated in figures 3-3 and 3-4 above, show the following observations for the second specimen at different orientation angles:

- By increasing the velocity the amount of normalized temperature ratio (θ) is decreasing linearly by the same rate on each sensor for both orientation angles of α=0° and α=45°.
- For all the velocities and 40°C for the temperatures of the hotplate at α=45°, the detected temperature in all of the sensors is 1-4% less than α=0°.
- For all the velocities and temperatures of the hotplate higher than 40°C at α=45°, the detected temperature in all of the sensors is 0-1% less than α=0°.
- Lower the flow speed and the temperature of the hotplate, higher is the variation of the normalized temperature ratio (θ) between α=0° and α=45°.
- The amount of transferred thermal energy (can be estimated by equation 3-4) from specimen 2 to the flowing fluid in the case of α=0°, which is proportional to the normalized temperature ratio (1-θ), for velocities of 5, 9, 17 and 25m/s is 73%, 71%, 67% and 59% respectively less than the case of α=45° in average.

The experimental results, which are illustrated in figures 3-5 and 3-6 above, show the following observations for the third specimen at different orientation angles:

- By increasing the velocity the amount of normalized temperature ratio (θ) is decreasing linearly on each sensor for both orientation angles of α=0° and α=45°.
- The rate of this linear reduction for α=0° is higher than α=45°.
- For velocity of 5m/s and all temperatures of the hotplate and α=45°, the detected temperature in all of the sensors is 17-29% less than α=0°.

- For velocity of 9m/s and all temperatures of the hotplate and α=45°, the detected temperature in all of the sensors is 9-24% less than α=0°.
- For velocity of 17m/s and all temperatures of the hotplate and α=45°, the detected temperature in all of the sensors is 4-22% less than α=0°.
- For velocity of 25m/s and all temperatures of the hotplate and α=45°, the detected temperature in all of the sensors is 1-19% less than α=0°.
- Lower the flow speed and the temperature of the hotplate, higher is the variation of the normalized temperature ratio (θ) between α=0° and α=45°.
- The amount of transferred thermal energy (can be estimated by equation 3-4) from specimen 3 to the flowing fluid in the case of α=0°, which is proportional to the normalized temperature ratio (1-θ), for velocities of 5, 9, 17 and 25m/s is 28%, 22%, 14% and 10% respectively less than the case of α=45° in average.

The experimental results, which are illustrated in figures 3-1 to 3-4 above, show the following observations between the first and second specimens:

- Increasing the velocity shows a steeper decrease in the amount of normalized temperature ratio (θ) in specimen 2 in comparison with specimen 1 at α=0°and all the selected temperatures for the hotplate.
- Increasing the velocity shows the same decrease in the amount of normalized temperature ratio (θ) in specimen 2 in comparison with specimen 1 at α=45°and all the selected temperatures for the hotplate.

The experimental results for the first specimen (figures 3-1 and 3-2) and third specimen (figure 3-5 and 3-6) show the following observations:

- Increasing the velocity shows a steeper decrease in the amount of normalized temperature ratio (θ) in specimen 3 in comparison with specimen 1 at α=0°and all the selected temperatures for the hotplate.
- Increasing the velocity shows a steeper decrease in the amount of normalized temperature ratio (θ) in specimen 1 in comparison with specimen 3 at α=45°and all the selected temperatures for the hotplate.
- The amount of normalized temperature ratio (θ) in specimen 3 considered lower values in comparison with specimen 1 at both orientation angles and all the velocities for the flowing fluid.

The experimental results for the second specimen and third specimen (figure 3-3 and 3-6) show the following observations:

- Increasing the velocity shows a steeper decrease in the amount of normalized temperature ratio (θ) in specimen 3 in comparison with specimen 2 at α=0°and all the selected temperatures for the hotplate.
- Increasing the velocity shows a steeper decrease in the amount of normalized temperature ratio (θ) in specimen 2 in comparison with specimen 3 at α=45°and all the selected temperatures for the hotplate.
- The amount of normalized temperature ratio (θ) in specimen 3 considered lower values in comparison with specimen 2 at both orientation angles and all the velocities for the flowing fluid.

By studying the simulation results of all the models (figures 3-7 to 3-12) for different orientation angles, it can be observed that:

- There is a less than 5% variation between the results for two different orientation angles at any specific velocity and hot plate temperature for each model.
- In some of the results there is a jump between the results for different velocities, which the reason was described before in the beginning of part 3.2.

In the 3rd model:

- The considered values for the normalized temperature ratio (θ) at α=45° are lower than the case of α=0° (to get less than 10% variation between the experimental and simulation results).
- Results show that by changing the orientation angle from 0° to 45°, the temperature distribution and the normalized temperature ratio (θ) on each specific point will be decreased.

In the previous parts models of the same geometries with the experimental specimens are built in ANSYS software and the program was run for each one to evaluate what would be the temperature distribution inside each model within the experiments. Further the applied thermal boundary conditions inside the ANSYS tuned to get as close as possible results with the experimental results (explained in part 2.2.3). Although the errors were minimized, one will still encounter errors. The results of these errors are given below.

By comparing the experimental and simulation results (figures 3-13 to 3-18), one can see that:

- All of the simulation results have less than 10% error in compare with their individual experimental results.

3.4. Summary

It can be concluded that:

- In orientation angles of 45° for the square pins, the amount of transferred heat is 10-40% higher for the same boundary conditions versus 0° orientation angle.
- The simulation process, which carried out in chapter 2, can be used to design heat exchangers based on forced convection mechanism (the expected results are as accurate as 10% with respect to the experiment).

CHAPTER 4

Design and Optimization of a Micro Heat Exchanger

This chapter presents the design and optimization process of a micro heat exchanger (the extended surface type of heat exchangers) and discusses the feasibility of the micro fabrication methods that can be used to fabricate such type of devices.

After the calibration of the ANSYS models to match the results of the experimental work as presented in chapter three, the models were extrapolated to the micro scale models considering geometrical low scaling. Two important expressions for analyzing fluidics in the micro domain are the Reynolds number and friction factor [49]. The Reynolds number characterizes fluid flow as laminar or turbulent and includes fluid properties ρ, μ, characteristic length (L) and average velocity (U):

$$\mathrm{Re} = \frac{\rho UL}{\mu} \tag{4-1}$$

Characteristic length, is the length which best represents the body under construction. The friction factor is given by:

$$f = \frac{\Delta pL}{2\rho U^2 l} \tag{4-2}$$

In this equation, l is the length of the tube. The relation between two dimensionless groups is defined by:

$$f = F(\mathrm{Re}) \tag{4-3}$$

According to this equation the friction factor for smooth pipe flow of all incompressible Newtonian fluids is thus a unique function of the Reynolds number. This is very insight. Only two groups of variables need to be studied experimentally to obtain a relation that is universally valid for a wide class of fluids:

- Geometries
- Flow parameters

Simple calculations show that the Reynolds number is so low in Microsystems and turbulence flow is not likely to be observed even with large values of roughness inside the system [49]. Consequently, formulations for laminar fluid flow could be used to derive the scaling law for liquid flow in micro scale [50].

Heat conduction in solids is governed by Fourier law, which for one dimensional heat conduction along the x coordinates, we have [50]:

$$Q_x = -kA\frac{\Delta T}{\Delta x} \qquad (4\text{-}4)$$

In this equation, Q_x (W) is the amount of conducted heat through the x coordinate of the solid, k (W/m.K) is the thermal conductivity of the solid, A (m^2) is the surface that conduction is going through, ΔT (K) is the temperature gradient trough the length Δx (m). It is readily seen from equation 4-4 that the scaling law for heat conduction for solids in micro scales is $Q_x \propto (l^2)(l^{-1}) = l$. It is easy to see from this simple scaling law that reduction in size leads to the decrease of total heat flow in a solid [50].

Heat convection is governed by Newton's cooling law or in more generic form as [50]:

$$Q = hA\Delta T \tag{4-5}$$

In this equation, Q (W) is the total heat flow between two points in the fluid, h (W/m².K) is the heat transfer coefficient, A (m²) is the cross sectional area for the heat flow and ΔT (K) is the temperature difference between the two points. The heat transfer coefficient (h) depends primarily on the velocity of the fluid, which does not play a significant role in the scaling of the heat flow. Consequently, the total heat flow primarily depends on the cross sectional area (A), which is of the order (l^2). Thus we have the scaling of heat transfer in convection to be $Q \propto (l^2)$ for fluids in micro regimes [50].

The dimensionless number which characterizes the magnitude of the established thermal gradient is the Biot number (Bi):

$$Bi = \frac{hL}{k} \tag{4-6}$$

In this equation h (W/m².K) is the surface heat transfer coefficient, k (W/m.K) is the thermal conductivity of the surface and L (m) is the characteristic dimension. As L becomes smaller, the Biot number goes down. For Bi<<1, internal temperature gradient become small and the body can be treated as having a uniform temperature. Consequently, with small devices (micro devices) there is less worry about thermal stresses inducted by thermal gradients and systems with larger heat generation capacity by volume can be built [49].

At the very beginning, it was found that the square shape pins are able to transfer more heat to the flowing fluid than the circular pins of the same height and hydraulic diameter D_h (greater volumetric geometries for the square pins as a consequence). Further, square shape pins were used for simulations in ANSYS to find an optimized value for the ratio of the *height of the pin/ thickness of the base* (L/t) at a specific constant temperature of the base in contact with air as a flowing fluid. The simulations have been performed for different ratios of L/t and for different number of square pins of equal total contact area with the flowing fluid. Subsequently a micro heat exchanger with three different arrays of pins at the same surface is presented as one possible design. Because of existing limitations in applying the boundary conditions in ANSYS, it was assumed that the velocity of the flowing fluid has a uniform profile around the models especially in the solid-fluid borders. This assumption is an underestimation of the performance of the design and is directed toward the higher safety factors for the design.

At the next step, an optimized array is introduced for the design and finally the final proposed design is introduced.

The micro heat exchanger is assumed to be made of silicon, which is a compatible material for electronic circuits. The flowing fluid is assumed to be air at the temperature of 17°C (290K). The availability and the accessibility as well as its thermo physical properties recommend air as an alternative of cooling fluid in this design.

4.1. The Optimized Shapes for the Pins

This part contains the basic analyzes for the optimum shape of pins, which are further used in the design with the objective to transfer the maximum heat through the contact face with a coolant fluid.

The analyses include the evaluation of the transferred heat from the total area of a pin in contact with the cooling fluid for two different types of pins of the same height and same Hydrodynamic Diameter D_h.

One of the most practical properties for the comparison of the different type of pins in contact with a cooling fluid flowing around them is the Hydrodynamic Diameter, which is described as:

$$D_h = \frac{4V_f}{A_f} \tag{4-7}$$

In equation 4-7, V_f (m^3) is the wetted volume and A_f (m^2) is the contact area with the flowing coolant. By using D_h (m), one can find the relationship between the total amount of transferred heat and the different shapes. The following assumptions are used in the analyses:

- Equal height for the pins (L).
- The same surface temperature (T_s, °C) for the pins.
- A source of heat generation (q″, W/m^2) is on the bottom of the pins.
- Physical specifications of the coolant are constant.

4.1.1. Pin with Circular Section

Assume a pin illustrated in figure 4-1-a with a circular section in contact with a flowing fluid with the velocity of U_∞ (m/s). The hydrodynamic diameter and the transferred heat from the pin to the coolant are expressed by:

$$(D_h)_{Circular} = \frac{4V_f}{A_f} = \frac{4(\pi D^2/4)L}{\pi DL} \Rightarrow (D_h)_{Circular} = D \tag{4-8}$$

$$q_{Circular} = h_f \pi (D_h)_{Circular} L(T_s - T_\infty) + h_f \pi \frac{D^2}{4}(T_s - T_\infty) \tag{4-9}$$

In equations 4-7 and 4-9, D (m) is the diameter of the circular pin, L (m) is the height of the circular pin, T_s (°C) is the surface temperature of the pin, T_∞ (°C) is the temperature of flowing fluid, $(D_h)_{Circular}$ (m) is the hydrodynamic diameter of the circular pin, $q_{Circular}$ (W) is the amount of transferred heat from the pin to the coolant and h_f (W/m².K) is the heat transfer coefficient of the flowing fluid.

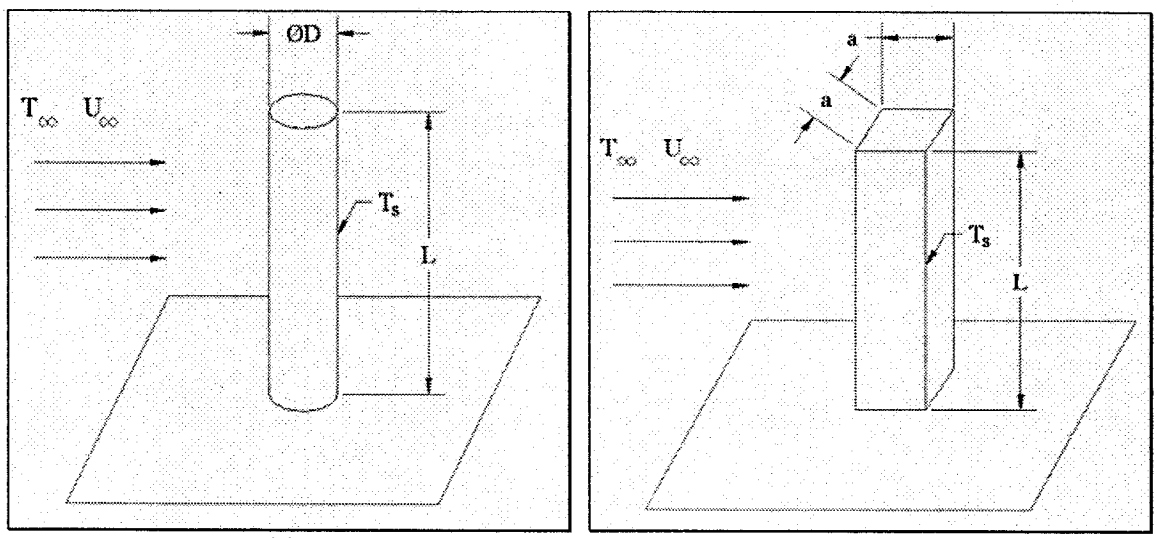

Figure 4-1. Schematic of pins, (a) Circular pin, (b) Square pin

4.1.2. Pin with Square Section

Consider a square section pin with side ***a*** (m), which is assumed to be equal to the diameter of the circular pin described on part 4.1.1 and the same height of L and surface temperature T_s in contact with the same cooling fluid (figure 4-1-b). The hydrodynamic diameter for this pin and the transferred heat from the pin to the coolant are expressed by:

$$(D_h)_{Square} = \frac{4V_f}{A_f} = \frac{4a^2L}{4aL} \Rightarrow (D_h)_{Squarer} = a \qquad (4\text{-}10)$$

$$q_{Square} = h_f 4(D_h)_{Square} L(T_s - T_\infty) + h_f a^2 (T_s - T_\infty) \qquad (4\text{-}11)$$

In equations 4-10 and 4-11, a (m) is the edge of the square pin, L (m) is the height of the square pin, T_s (°C) is the surface temperature of the pin, T_∞ (°C) is the temperature of flowing fluid, $(D_h)_{Square}$ (m) is the hydrodynamic diameter of the square pin, q_{Square} (W) is the amount of transferred heat from the pin to the coolant and h_f (W/m².K) is the heat transfer coefficient of the flowing fluid.

By comparing equations 4-9 and 4-11, one can notice that:

- For two pins with different geometries namely square and circular, and of equal hydraulic diameter and height in contact with the same flowing fluid, the amount of transferred heat from the square pin to the flowing fluid is higher than for the circular pin.

As a result, the pins with square sections are more efficient in comparison to the circular section pins of same height and hydraulic diameter D_h (greater volumetric geometries for the square pins as a consequence). Therefore square pins are used in the presented design.

4.2. Simulation of a Pined Silicon Base for Different Ratios of Height of the Pin/ Thickness of the Base (*L/t*)

In this part, macro scale models were considered for simulations using ANSYS finite element analysis (FEA) to identify an optimized value for the ratio of the *height of the pin/ thickness of the base* (*L/t*) (figure 4-2) with equal total contact surface at the border of the solid-fluid. The base temperature is considered 60°C (high temperature encountered in the electronic circuits) in contact with air as a flowing fluid at 27°C (considering the worst environmental case). The bottom of this model is assumed to be a (25.4mm×25.4mm×12.7mm) silicon based material among a (11.43mm×11.43mm×12.7mm) pin on it. Models have analyzed by increasing the ratio *L/t* from 1 to 7.

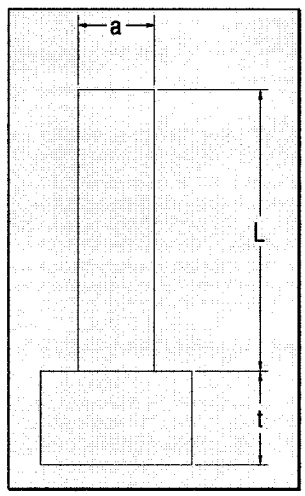

Figure 4-2. Parametric dimensions on a square pin

The simulations have been done for each specific ratio of L/t by increasing the number of pins from 1 to 2,4,6,8 and 9 on the same surface, as illustrated in figure 4-3. At this point the important factor is that the total contact area with the flowing fluid (air) is equal for all the situations, which means that the size of the pins were decreased by increasing their number on the base.

Figures 4-4 and 4-5 illustrate the amount of the transferred heat flux from a surface, the pins on it and the total transferred heat flux to the flowing air for the base temperature of T_{hp} =60°c and air velocity of V=10m/s. The amounts of Q''_{total} (W/m²) can be calculated from the following equation:

$$Q''_{total} = Q''_{Surface} + Q''_{Pin} \times n \qquad (4\text{-}12)$$

In this equation, Q''_{total} (W/m²) is the total thermal transferred heat flux from a pined surface, $Q''_{Surface}$ (W/m²) is the thermal transferred heat flux from the pined surface except those areas under the pins, Q''_{Pin} (W/m²) is the thermal transferred heat flux from one pin and n is the number of the pins on a surface.

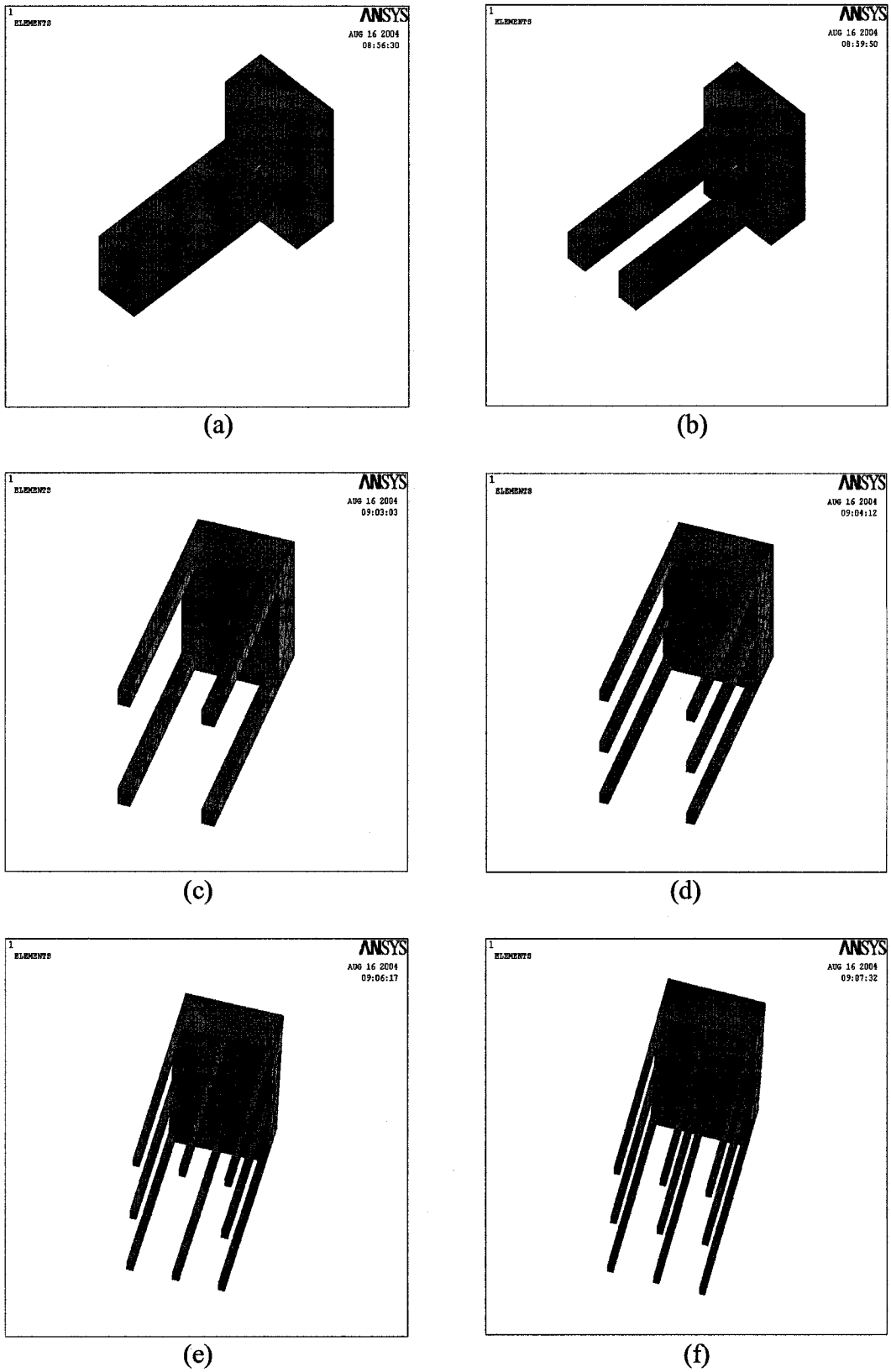

Figure 4-3. Schematic of 25.4x25.4 mm² models with different number of pins, (a) N=1, (b) N=2, (c) N=4, (d) N=6, (e) N=8, (f) N=9.

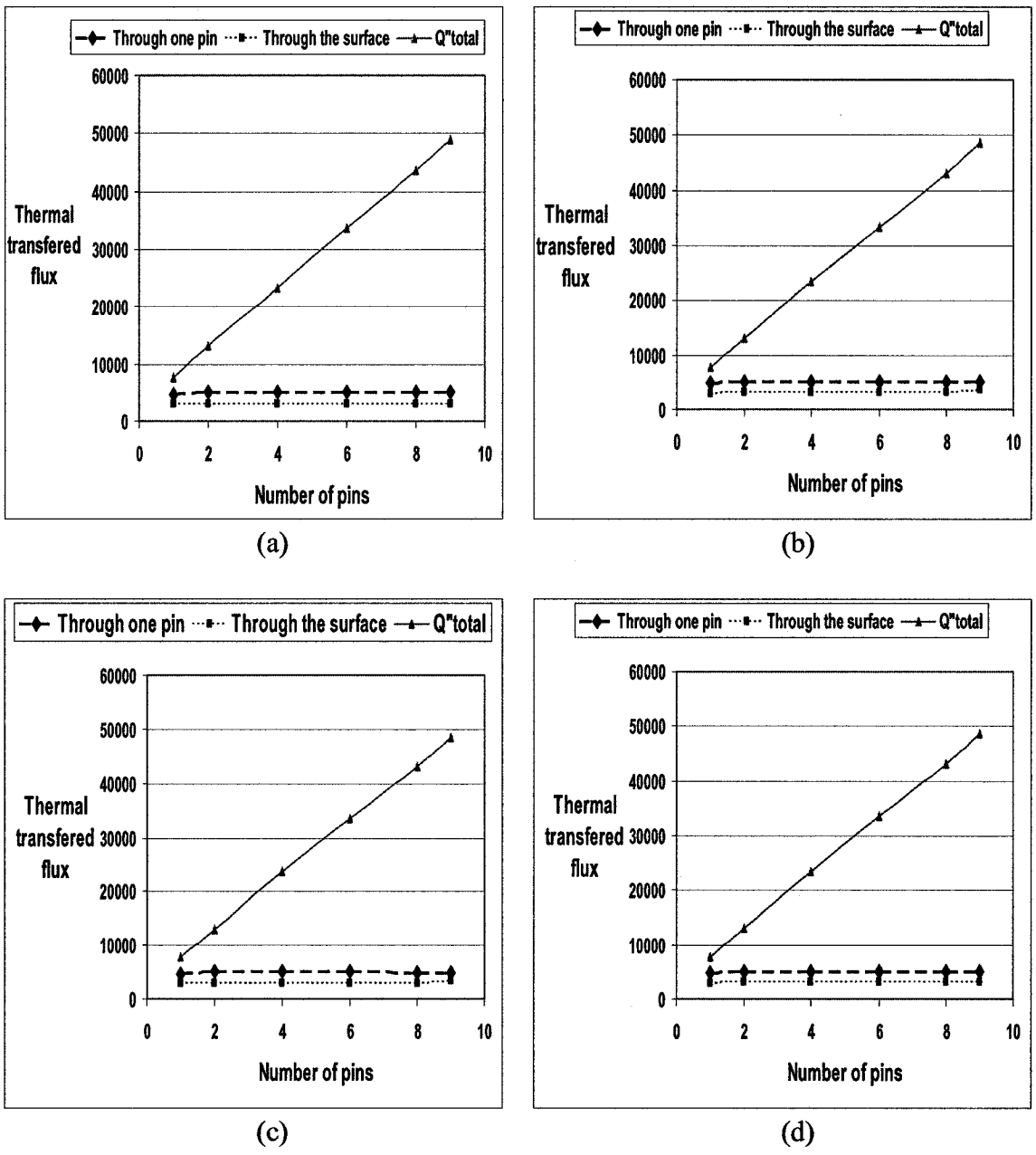

Note: The units in the y axis is w/m²

Figure 4-4. Results of transferred thermal heat flux from the base of 25.4x25.4 mm² area with the temperature of 60°C to the flowing air, (a) L/t=1, (b) L/t=2, (c) L/t=3, (d) L/t=4.

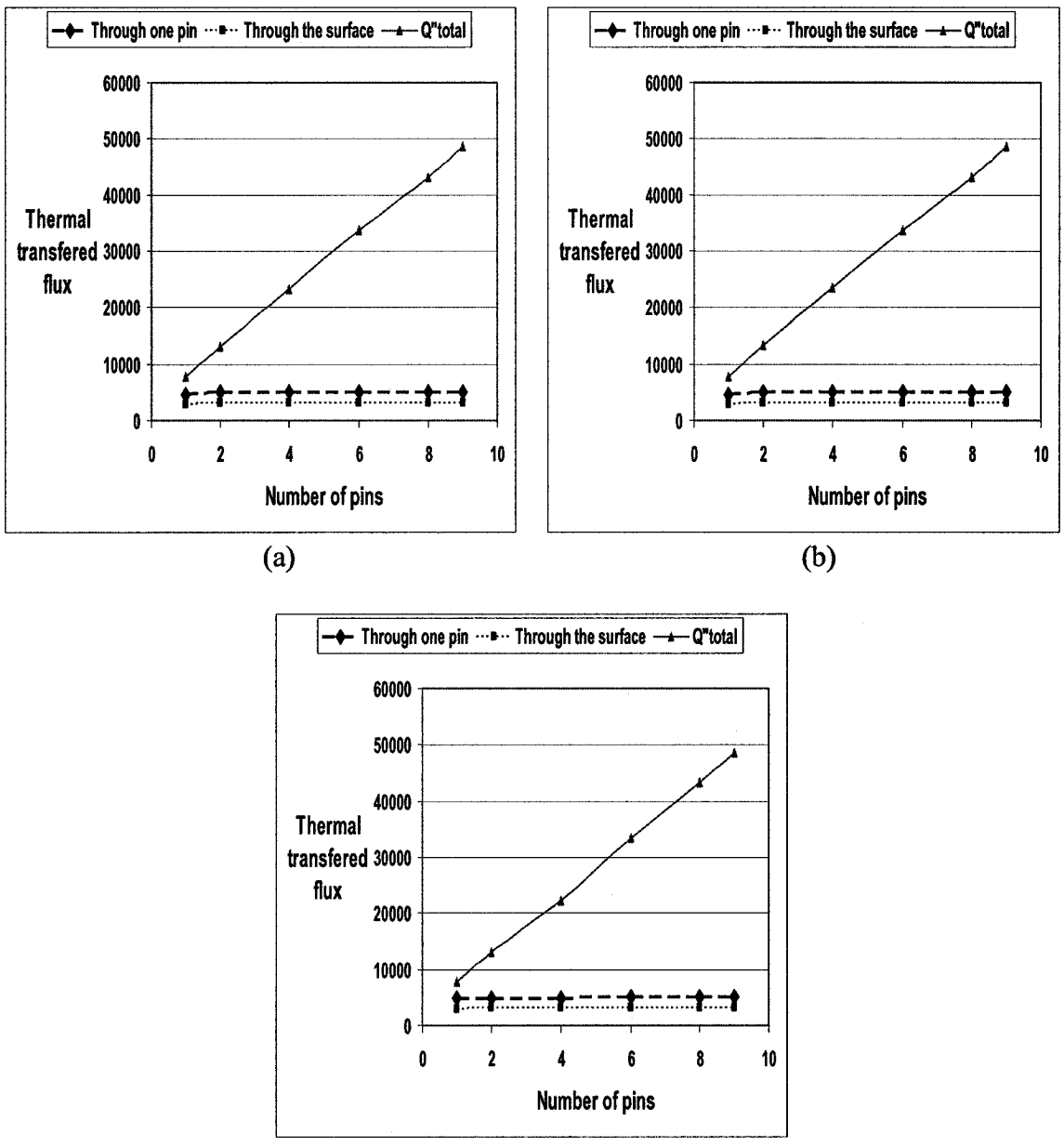

Note: The units in the y axis is w/m²

Figure 4-5. Results of transferred thermal heat flux from the base of 25.4x25.4 mm² area with the temperature of 60°C to the flowing air, (a) L/t=5, (b) L/t=6, (c) L/t=7.

These results are compared and illustrated in figure 4-6.

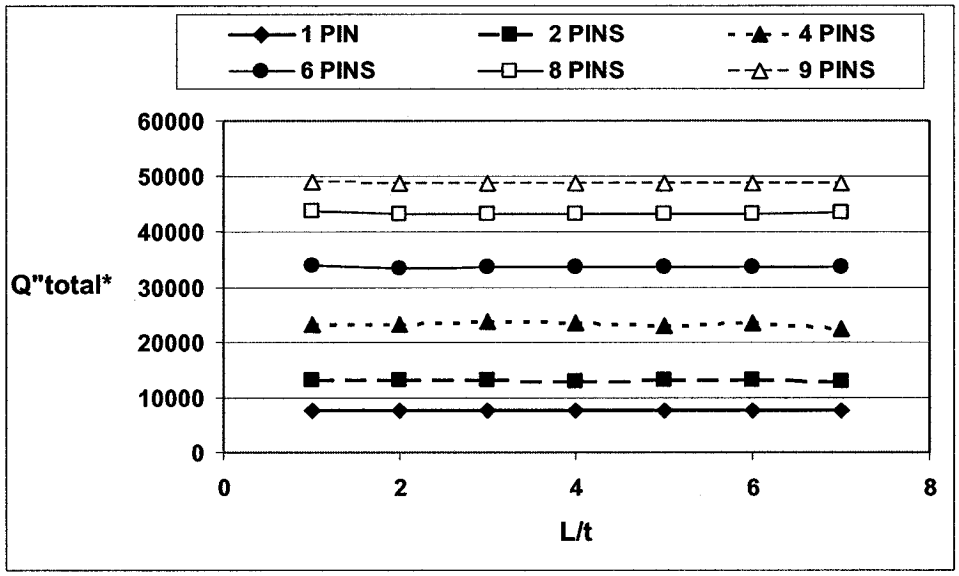

Figure 4-6. Total transferred thermal heat flux from the 25.4x25.4 mm² base of 60°C in different ratios of L/t and different number of the pins in contact with air (* The units are W/m²)

The above simulation results reveal that:

- By increasing the number of pins on the surface at any constant value for ratio of L/t the total amount of thermal heat flux from the surface is increasing.
- There is less than 5% variation on the total amount of transferred heat flux ($Q"_{total}$) at any ratio of L/t for all the number of pins on the base.
- By increasing the number of pins on the base the variation of the transferred heat is more significant at different ratios of L/t.

4.3. Simulation of a Pined Silicon Base for Different Ratios of Height of the Pin/ Edge of the Pin (*L/a*)

The results of previous part (4.1.2) can be used for the ratio of *height of the pin/ edge of the pin* (*L/a*) (figure 4-2) and compared under the same conditions. The relationship between the ratio (*L/a*) versus the total transferred heat is illustrated in figure 4-7.

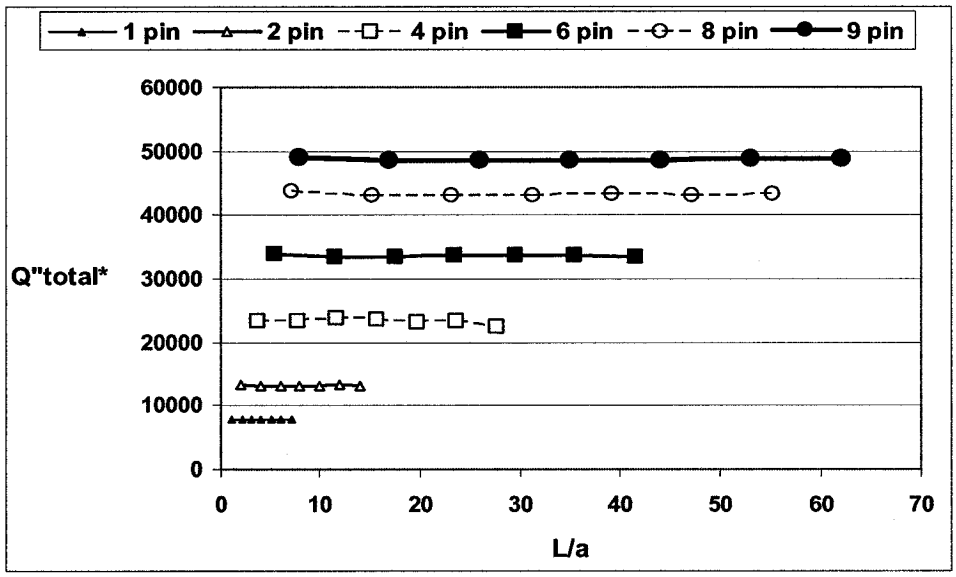

Figure 4-7. Total transferred thermal heat flux from the 25.4x25.4 mm² base of 60°C in different ratios of L/a and different number of the pins in contact with air (* The units are W/m²)

The above results reveal that:

- A larger number of pins produce an increase in the total amount of transferred heat flux.
- By increasing the *L/a* (*height of the pin/edge of the pin*) ratio the amount of transferred heat flux is increasing.
- By increasing the number of pins and consequently decreasing their hydraulic diameter, the amount of the transferred heat will increase.

In each design, one should be aware that there are limitations on choosing correct value for the L/a ratio. These limitations are directly related to the mechanical properties of the base material and the amount of applied mechanical stresses to the pins by the surrounding flowing fluid. The important aspect of the design is to choose the most applicable value for the L/a ratio, which is applicable with micro fabrication limitations. One of the limitations in fabrication is that in this design a height of 100 μm, which is a practical value for fabrication with available micro fabrication methods, is considered for the whole structure considering micro pins with 80 μm height and a practical and safe value for the edge of the pins to get enough safety factors in design. For this reason the value of L/a=16 is considered in this design, which has enough participation for most of the situations described in parts 4.2 and 4.3. As a consequence the proposed value for the edge of the pins (a) will be equal to 5 μm. This ratio is the starting point on the graphs of figure 4-7 in which the variations between the results for any specific value of the pins on a surface is more significant.

4.4. Proposed Optimized Topography of Pin Arrays

In this part the results of the optimized topography of pin arrays available in the open literature have been used in conjunction with the proposed square pin configuration and the results are presented below.

A. Zukauskas and R. Ulinkas [30] have carried out significant number of experimental investigations on heat transfer from the banks of circular tubes in cross flow with different fluids for both staggered and in-line banks and their conclusions are presented below:

- The amount of the transferred heat from the columns (poles) in the first row of the bank is lower than the inner rows. The cause of this fact is that at low *Re* numbers while the flow is reaching the first row, it is laminar and it further converts into slightly turbulent and the heat transfer increases in the following banks.
- For a specific column arrangement in the in-line banks, the heat transfer of an inner row at low *Re* numbers is even less than the heat transfer in the first row in view of shadowing.
- Starting with the third row of the banks, heat transfer in the following rows stabilizes and practically coincides with the heat transfer of the third row.
- Heat transfer in an inner row increases with decreasing of the longitudinal pitch of the banks.
- The in-line banks of poles with small longitudinal pitch are an exception, where a decrease in pitch can lead to a decrease in the heat transfer.
- In steady state flow heat transfer of a tube in a bank is significantly higher than heat transfer of a single pole. This fact is due to the small thickness of boundary layer on the surface of a tube in the bank and to the elevated turbulence of flow in the inter-tubular spacing.
- The staggered banks of tubes are more efficient in comparison with the in-line banks of tubes because of the relatively higher mean heat transfer coefficient as illustrated in figure 4-8.
- The staggered banks of columns are more recommended for the design options because of flexibility in changing the longitudinal pitch design.

From the above investigations, one can clearly conclude that the staggered array of pins performs better in comparison to the in-line array of pins and for the design of this project the staggered arrays are the priority.

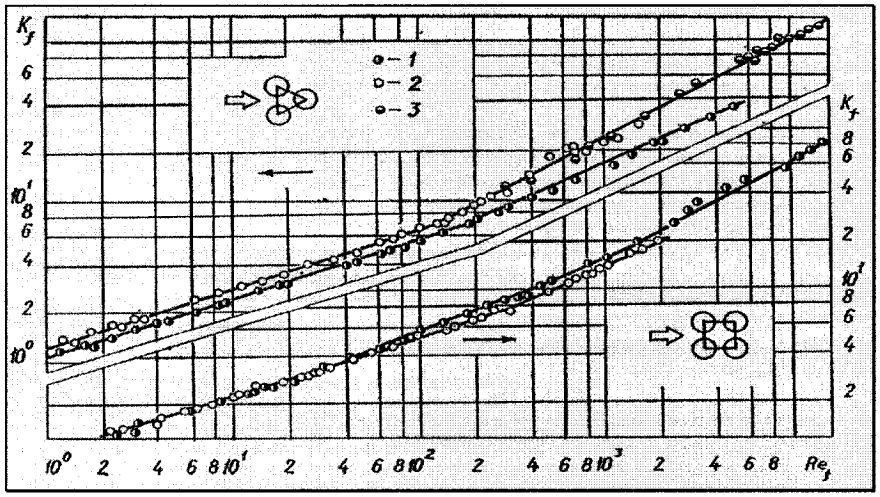

Figure 4-8. (Repeated figure 1-1) Mean heat transfer coefficient of tubes in different rows of staggered and in-line banks, 1) First row, 2) Forth row, 3) Third row. [30]

4.5. Modeling of the Proposed Configuration

Based on the above observations and taking into account the micro-fabrication constraints, a proposed design for the micro heat exchanger is illustrated in figure 4-9. This micro heat exchanger is made of a silicon chip with square base with the edge of E equal to 10000 μm (1cm) and base thickness of t=375 μm with staggered arrays of square silicon pins, which have the orientation angle of 45° with the direction of the flow, and the height of channel is equal to H=100 μm. It is assumed that on the top of the channel a glass layer is bonded, which behaves as an insulator in comparison with the silicon channel (figure 4-10) and has the role to protect the pins against contamination. The maximum thickness for the silicon wafers that would enable deep etching and standard manipulations during the process and after is about 475 μm, which by considering a

channel height of 100 μm the thickness of the wafer should be around 375 μm. The height of the pins is considered less than 100 μm to let the flowing fluid pass through the top of pins as well as their circumferential area.

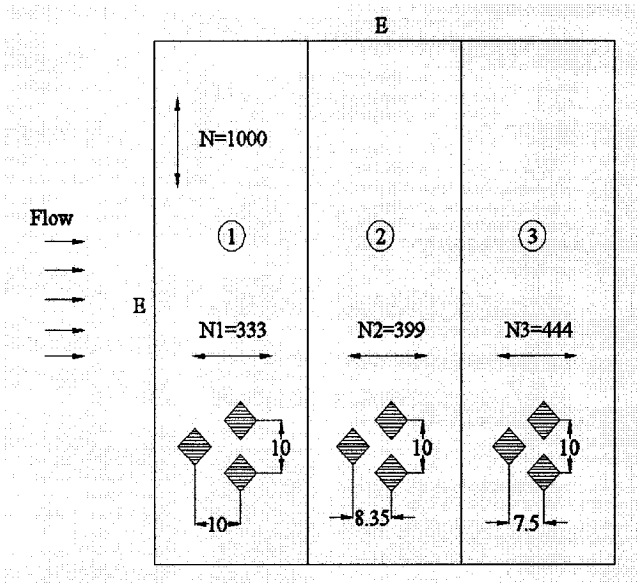

Figure 4-9.Top view of micro heat exchanger

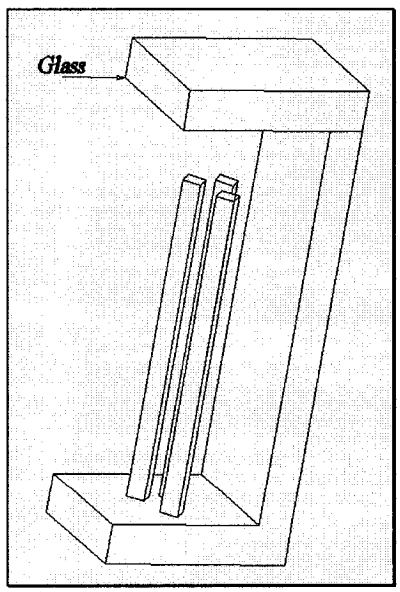

Figure 4-10. Schematic of glass layer on the top of micro heat exchanger

Each square pin has the length of L=80μm with the edge of d=5 μm (assumed the ratio L/a=16 as the recommended ratio for the design consideration).

The pin arrays are divided into three segments. The first segment, as it is shown on the left side of figure 4-9, is at the cooling fluid entrance in the channel with the pitch ratio of 2×2 (times of the edge d of the pin) in both the longitudinal and vertical directions of the flow. The first term of this ratio (2×2), is for the pitch ratio on the rows vertical to the flow direction and the second term is for the rows on the longitudinal direction. By considering this pitch ratio for this segment, the total estimated number of rows in the longitudinal direction will be equal to N_1=333.

The second region is on the middle of the channel with the pitch ratio of 2×1.75 respectively for the longitudinal and vertical directions. By considering this pitch ratio, the total number of rows in the longitudinal direction in this segment will be equal to N_2=399.

The third region is on the right side of the figure 4-9 with the pitch ratio of 2×1.5 correspondingly for the longitudinal and vertical directions and by considering this pitch ratio the total number of rows in the longitudinal direction will be equal to N_3=444.

The total number of rows vertical to the flow direction is equal to N=1000 for all the three segments.

The values of 2×2 and 2×1.5 for the pitch ratio are the maximum and minimum recommended values by A. Zukauskas and R. Ulinkas [30].

Some dimension limits are based on the static analysis that will be presented on part 4.6 and related micro fabrication processes.

4.6. Mechanical Analysis

The static analysis will be presented here to show what will be the mechanical performance of the pin dimensions against the flow and what the mechanical safety factor of this design is. The following assumptions have been made:

- The flowing fluid is air at temperature of 17°C as the most disadvantageous scenario encountered for the cooling fluid.
- The entrance velocity of the air into the channel is V=1m/s.
- Because of small sizes of the device the thermo physical properties of air can be assumed invariable through the length of it.
- The thermo physical properties of air at 17°C are [3], $\rho_f = 1.20806\,\text{Kg/m}^3$, $\mu_f = 179.6\times10^{-7}\,\text{N.s/m}^2$, $K_f = 25.5\times10^{-3}\,\text{W/m.K}$ and $\text{Pr}_f = 0.7096$.
- The Prandtl number (dimensionless number approximating the ratio of momentum diffusivity and thermal diffusivity) of air at different temperatures of 40°C, 50°C, 60°C and 70°C are respectively [3], $\text{Pr}_f(40) = 0.70518$, $\text{Pr}_f(50) = 0.70378$, $\text{Pr}_f(60) = 0.70238$ and $\text{Pr}_f(70) = 0.70098$ (will be further used in part 4.7).
- Constant mechanical properties for the silicon base ($S_y = 7\times10^9$ Pa) [36].
- Constant thermal conductivity for silicon ($K_{silicon} = 150$ W/m.k) [36].

The applied force on each specific pin by the flowing fluid can be found from equation 4-13.

$$F = \frac{\dot{m}(V_{max} - V)}{N} \tag{4-13}$$

In equation 4-13:

- $\dot{m}$ is the amount of fluid mass transfer per unit of second (Kg/s).
- V_{max} is the maximum velocity inside the channel, which is the velocity on the narrowest portion of the channel between corners of two neighbor pins (m/s).
- V is the entrance velocity (m/s).
- N is the number of rows vertical to the flow direction.

The following equation is used to find the $\dot{m}$ value.

$$\dot{m} = \rho \cdot V \cdot A = \rho \cdot V_{max} \cdot A_{min} \cdot N \tag{4-14}$$

In equation 4-14:

- ρ is the density of the flowing fluid (Kg/m^3).
- A_{min} is the smallest area that the fluid is passing through it (m^2).
- A is the entrance area of the channel (m^2).

By applying the chip dimensions described in part 4.5 and thermo physical properties into equation 4-14 the following values are resulted for $\dot{m}$ and V_{max} :

$$\dot{m} = 1.20806 \times 1 \times [(100 \times 10^{-6}) \times (10000 \times 10^{-6})] \Rightarrow \quad \dot{m} = 1.20806 \times 10^{-7}\ \text{Kg/s}$$

$$V_{max} = \frac{V \cdot A}{A_{min} \cdot N} \Rightarrow V_{max} = \frac{1 \times [(100 \times 10^{-6}) \times (10000 \times 10^{-6})]}{[(100 \times 10^{-6}) \times (2.93 \times 10^{-6})] \times 1000} \Rightarrow V_{max} = 3.4\ \text{m/s}$$

These values are entered into equation 4-13, to find the amount of applied force on one pin, which is equal to:

$$F_{static} = 2.899344 \times 10^{-10}\ \text{N}$$

To obtain more precise results along with the distribution of the flow and the force on the pin, some simulations have been performed with the Fluent software for the flowing fluid in the area between two neighbor pins to find the amount of local force on each pin. The applied boundary conditions in Fluent are; constant and uniform velocity of 1m/s in the inlet of the model, constant and uniform pressure of 1 atm at the outlet. The incompressible fluid was considered in the modeling accompanying with segregated solver, which is recommended by the software. The unstructured mesh (triangle) was considered as the meshing element. To achieve this outcome, the flow inside the channel between two neighbor pins was modeled inside the Gambit software area and meshed. Then the meshed model exported into the Fluent area and the exact boundary conditions (such as the entrance velocity of 1m/s) were applied to the flow. Then the amount of applied force on each pin was found from the simulation results. Contours of velocity and static pressure in this model are illustrated in figures 4-11 and 4-12. Also the velocity vectors are illustrated on figure 4-13.

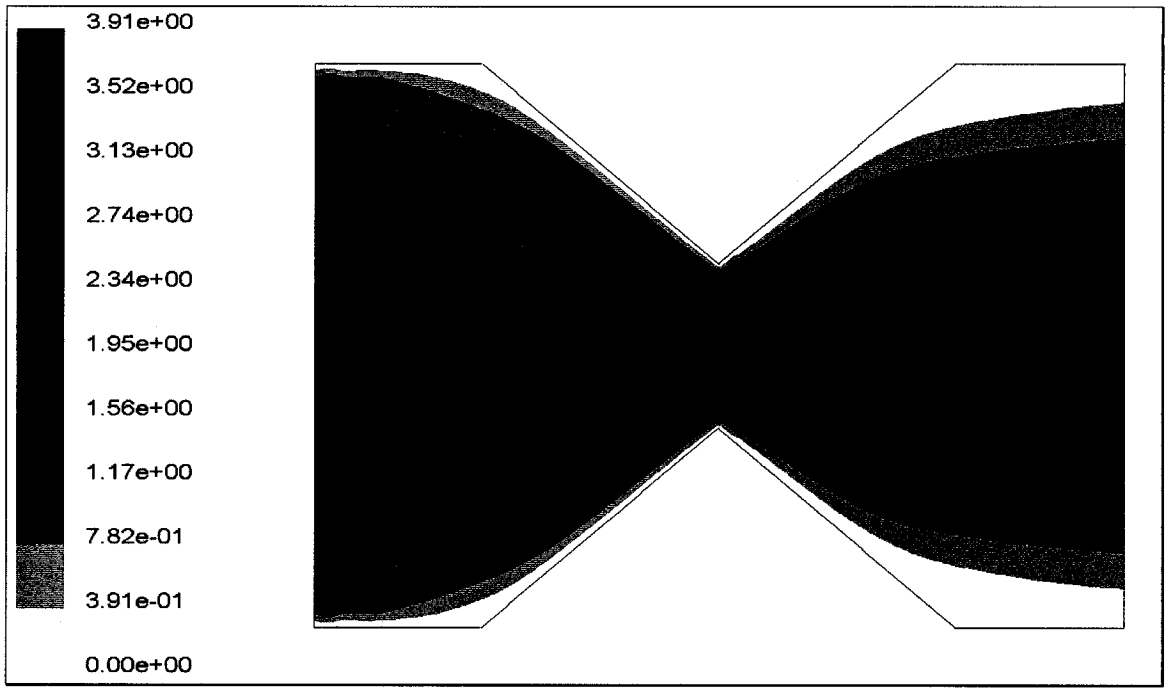

Figure 4-11. Velocity contours (m/s)

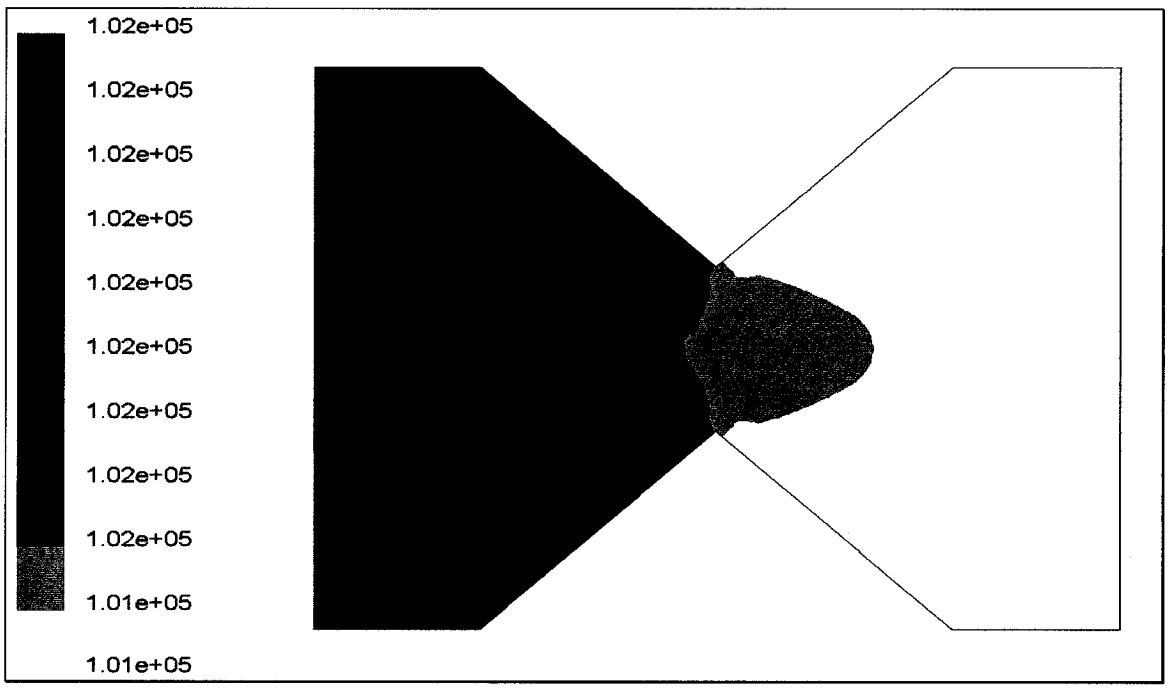

Figure 4-12. Static pressure contours (Pa)

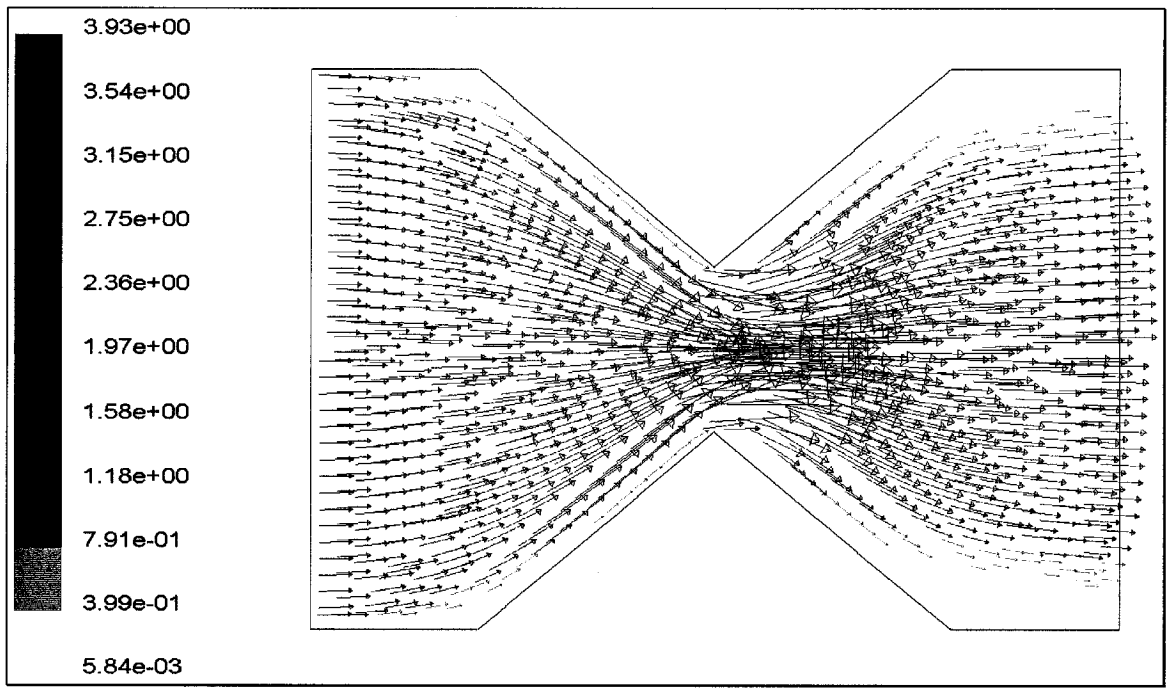

Figure 4-13.Velocity vectors (m/s)

The reported amount of the total applied force on one pin, according to the Fluent simulations, is equal to:

$$F_{simulation} = 3.42 \times 10^{-10} \text{ N}$$

In the subject of mechanical engineering design it is known that the amount of applied force and moment on the end of a square section cantilever beam with distributed force per unit length (illustrated in figure 4-14) can be found from equations 4-15 and 4-16 [35].

$$R = w \times l \tag{4-15}$$

$$M = \frac{-w \times l^2}{2} \tag{4-16}$$

In the above equations:

- w is the distributed force per unit length (N/m).
- l is the length of the beam (m).

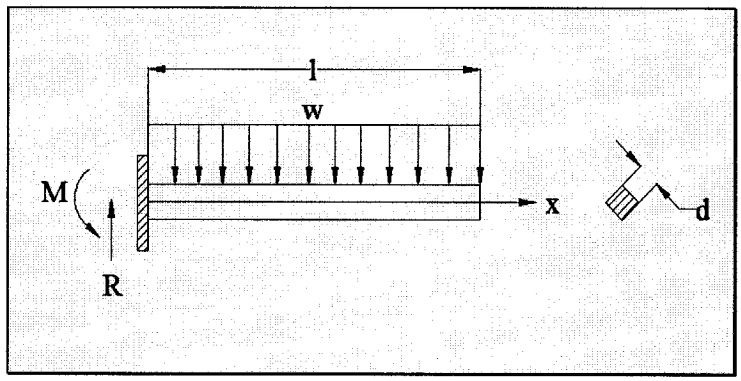

Figure 4-14. Cantilever beam with distributed force

This mechanical model is used to find the principal stresses on each individual pin. The estimated values for M and R from equations 4-15 and 4-16 are the maximum values for both moment and shear force inside the beam and the critical element is located on the top left end of the beam on figure 4-14. A schematic of this critical element is illustrated on figure 4-15.

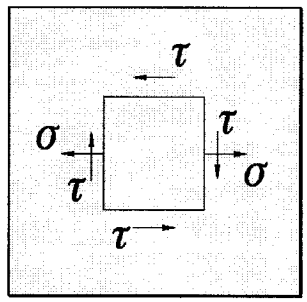

Figure 4-15. Critical element on the left bottom end of the beam

Both values of F_{static} and $F_{simulation}$ are used to find the safety factor based on Von Mises [35] criteria of design. The results are illustrated in table 4-1 for both the Fluent simulations and static equations.

Table 4-1. Fluent simulation and static results

	static	simulation
Rmax (N)	2.90E-10	3.42E-10
Mmax (N.m)	1.16E-14	1.37E-14
σ (N/m²)	7.88E+02	9.30E+02
τ (N/m²)	1.16E+01	1.37E+01
σ_1 (N/m²)	7.89E+02	9.30E+02
σ_2 (N/m²)	0	0
σ_3 (N/m²)	-1.71E-01	-2.01E-01
n	8930000	7520000

The values in table 4-1 are calculated based on equations 4-17 through 4-20.

$$\sigma = \frac{M_{\max} \times c}{I} \tag{4-17}$$

$$\tau = \frac{R_{\max}}{A_{section}} \tag{4-18}$$

$$\sigma_{1,3} = \frac{\sigma}{2} \pm \sqrt{(\frac{\sigma}{2})^2 + \tau^2} \qquad \sigma_1 > (\sigma_2 = 0) > \sigma_3 \tag{4-19}$$

$$2(\frac{S_y}{n})^2 = (\sigma_1 - \sigma_2)^2 + (\sigma_2 - \sigma_3)^2 + (\sigma_3 - \sigma_1)^2 \tag{4-20}$$

In the above equations:

- c (m) is the maximum distance that the critical element has from the center of beam, which in this problem is equal to $c = \frac{d \times \sqrt{2}}{2} = 3.535 \times 10^{-6} m$.

- I (m^4) is the area moment of inertia for the cross section of the beam, which is equal to $I = \frac{d^4}{12} = 5.2\times10^{-23} m^4$.
- σ_1, σ_2 and σ_3 (N/m^2) are the principal stresses.
- S_y (N/m^2) is the yielding strength of Silicon, which is equal to $S_y = 7\times10^9$ N/m^2.
- n is the safety factor.
- $A_{section}$ (m^2) is the sectional area of the beams, which is equal to $A_{section} = 2.5\times10^{-11}$ m^2.
- Equation 4-20 is the Von-Misses theoretical equation, which is normally used for both brittle and ductile materials [35].

According to the results on table 4-1, it can be concluded that this design is safe against the static pressure of the flowing fluid.

In the next part this design is used and modeled in ANSYS to obtain the thermal performance and find out the amount of the thermal flux, which is transferred through the pins from the base under a specific temperature.

4.7. ANSYS and Analytical Results

In this part the models, which are established in part 4.5, are modeled in ANSYS software. At the same time the analytical equations for the same models are introduced and used to estimate the amount of heat flux on each individual model at different temperatures for the base of the pins. Finally the results of both analytical and simulation are presented and compared together.

4.7.1. The Boundary Conditions in ANSYS

The following criteria are used in the ANSYS simulations to find the film coefficient as a boundary condition on the silicon pins [30]:

- The temperature of incoming fluid stream t_f as the determining temperature.
- The diameter of the pins d as the characteristic dimension.
- The velocity of the fluid in the minimum cross-sectional area between the pins $V_{\max}$ as the design velocity.

Equation 4-21 and 4-23 are used to find the values of Nu number for different Re numbers [30].

$$Nu_f = 1.04 \times \mathrm{Re}_f^{0.4} \times \mathrm{Pr}_f^{0.36} \times \left(\frac{\mathrm{Pr}_f}{\mathrm{Pr}_{hp}}\right)^{0.25} \qquad 1 \le \mathrm{Re}_f \le 40 \qquad (4\text{-}21)$$

$$Nu_f = 0.71 \times \mathrm{Re}_f^{0.4} \times \mathrm{Pr}_f^{0.36} \times \left(\frac{\mathrm{Pr}_f}{\mathrm{Pr}_{hp}}\right)^{0.25} \qquad 40 \le \mathrm{Re}_f \le 1.5 \times 10^3 \qquad (4\text{-}22)$$

$$\mathrm{Re}_f = \frac{\rho_f \times V_{\max} \times d}{\mu_f} \qquad (4\text{-}23)$$

In equations 4-21 through 4-23:

- Re_f is the Reynolds number at the temperature of incoming fluid stream t_f.
- Pr_f is the Prandtl number at the temperature of incoming fluid stream t_f.
- Pr_{hp} is the Prandtl number at the temperature of the base.

- ρ_f and μ_f are respectively the density and dynamic viscosity at the temperature of incoming fluid stream t_f.

By using equations 4-21 to 4-23 and the thermo physical properties of the air at $t_f = 17^\circ C$ for different temperatures for the base of the pin, which are described in part 4.6, it can be seen that the Reynolds number will be equal to $\mathrm{Re}_f = 1.15$.

The amount of film coefficient, which is applied as the boundary condition in the ANSYS simulations can be found from equation 4-24.

$$h_f = \frac{Nu_f \times K_f}{d} \tag{4-24}$$

The wall temperature on each edge of pins is determined to be uniform and equal to the film temperature t_{film}, which is calculated based on experimental results of chapter 2 and explanations on part 2.2.4. As a result the film temperature can be estimated from equation 2-8 by applying 0.5 for temperature coefficient factor at low *Re* numbers.

In the equation 4-24, K_f is the conductivity coefficient of the fluid at the temperature of the base (W/m.K). The estimated values for t_{film}, Nu_f and h_f for different temperatures of the base are presented on table 4-2.

Table 4-2. Boundary conditions at different temperatures for the base

T_{hp} (°C)	t_{film} (°C)	Nu_f (W/m.K)	h_f (W/m².K)
40	28.5	0.9735	4965
50	33.5	0.9740	4967
60	38.5	0.9745	4970
70	43.5	0.9750	4973

These values in table 4-2 are used as the boundary conditions on the ANSYS software for different conditions.

4.7.2. Heat Flux Analytical Equations

Donald Q. Kern and Allan D. Kraus [33] proposed the following equation for the amount of transferred heat from a base to the flowing fluid through a rectangular pin:

$$q = K_f a_1 a_2 m \theta_0 \tanh(ml) \tag{4-25}$$

In equation 4-25:

- a_1 and a_2 are the edges of the pin and l (m) is length of the pin (figure 4-16).

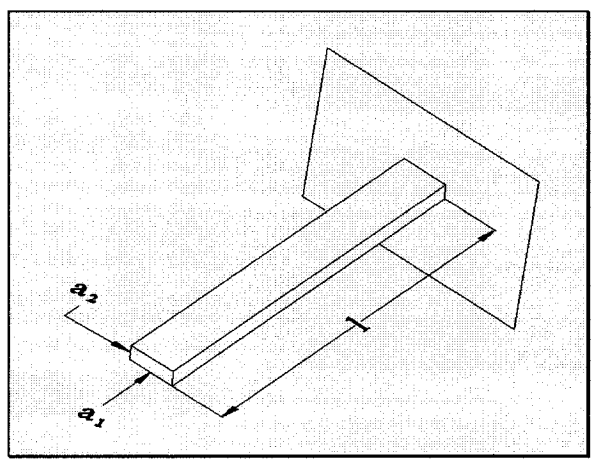

Figure 4-16. Model of a rectangular pin on a surface

- θ_0 (°C) is the difference between the base temperature (T_{hp}) and fluid temperature (t_f).
- K_f (W/m.K) is the conductivity coefficient of the fluid at the temperature of the base.

- m is a factor that can be find from equation 4-26.

$$m = \sqrt{\frac{h_f \times P}{K_f \times A}} \tag{4-26}$$

In equation 4-26, A (m^2) and P (m) are respectively the area section and the circumference of the rectangular pin, which are calculated from equation 4-27 and 4-28 and h_f ($W/m^2.K$) is the thermal heat transfer coefficient of the flowing fluid at the temperature t_f.

$$A = a_1 \times a_2 \tag{4-27}$$

$$P = 2 \times (a_1 + a_2) \tag{4-28}$$

As a consequence the amount of factor m for a square pin with edges of d can be found from equation 4-29.

$$m = \sqrt{\frac{4 \times h_f}{K_f \times d}} \tag{4-29}$$

The above equations are used to find the amount of transferred heat through one pin for three types of pin arrays, which was explained in part 4.5. The estimated amount of heat that is transferred through one pin to the flowing air is calculated from equation 4-23. Then for each type of pin array this amount will be divided by the total area, which is the total area under the bottom of each pin, and as a result the amount of transferred heat flux can be calculated for each pin array. The results of these estimations are shown in part 4.7.3.

4.7.3. Analytical and Simulation Results for 17°C Air as a Coolant

In this part 17°C air is used as a coolant fluid with the same conditions that was described in part 4.6. The analytical and simulation results are presented in figure 4-17. In this figure the horizontal axis represents the region number that was previously described in part 4.5. Further the total transferred heat and heat flux from each region are illustrated in table 4-3 through 4-6 for different values of T_{hp}.

From figure 4-17 it can be observed that;

- The ANSYS simulations results show a 5% increase in the amount of transferred heat flux by 33.3% increase in the number of pins at a surface and 2.5% increase by 20% increase in the number of pins at the same surface.
- According to the analytical results on tables 4-3 through 4-6, by 20% increase in the number of pins at a surface, there will result 19.7% increase in the amount of transferred heat flux and by 33.3% increase in the number of pins will yield 33.3% increase in the amount of transferred heat flux at the same surface.
- The above observations confirm that by increasing the dense of pins on a surface with a specific area, the amount of transferred heat flux is increasing.
- For the same geometry of the pins and same boundary conditions (same temperature for the hot plate and flowing fluid), the estimated values for the transferred heat flux by the ANSYS are 13 to 44% higher than analytical results.

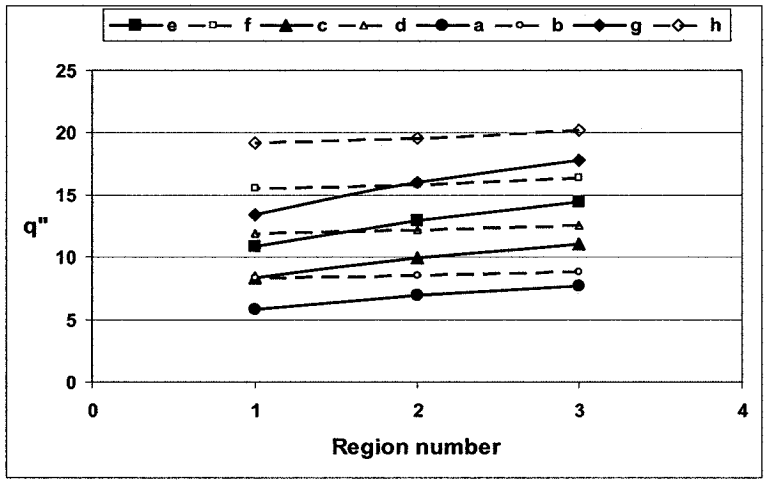

Note: Unit of q" is w/cm²

Figure 4-17. Analytical (filled lines) and simulation (dashed lines) results for 17°C air, (a) & (b) Thp=40°C, (c) & (d) Thp=50°C, (e) & (f) Thp=60°C, (g) & (h) Thp=70°C

Table 4-3. The amount of transferred heat and heat flux from every region to the air flow for Thp=40°C

Region	Transferred heat (W)	Transferred heat Flux (W/cm²)
1	1.929	5.787
2	2.310	6.93
3	2.572	7.716

Table 4-4. The amount of transferred heat and heat flux from every region to the air flow for Thp=50°C

Region	Transferred heat (W)	Transferred heat Flux (W/cm²)
1	2.768	8.305
2	3.316	9.947
3	3.691	11.074

Table 4-5. The amount of transferred heat and heat flux from every region to the air flow for Thp=60°C

Region	Transferred heat (W)	Transferred heat Flux (W/cm²)
1	3.608	10.824
2	4.321	12.963
3	4.811	14.432

Table 4-6. The amount of transferred heat and heat flux from every region to the air flow for Thp=70°C

Region	Transferred heat (W)	Transferred heat Flux (W/cm²)
1	4.449	13.346
2	5.328	15.983
3	5.931	17.794

4.8. Fabrication Methods in MEMS

This part covers the feasibility of anisotropic fabrication methods that can be applied to produce long and narrow square pins on a silicon wafer used in micro heat exchanger such as what was described on part 4.5. The principal theories that have been used in part 4.8.1 can be found in reference numbers [36], [41], [43] and any related source book in concern with physical structure of silicon.

4.8.1. Anisotropic Wet Etching of Silicon

Anisotropic etching of silicon is one of the principal methods, which is used to fabricate specific geometries such as channels, grooves, cantilever beams, etc. In this method a mask layer is protecting the silicon wafer except in areas where it has been patterned. Then an Anisotropic etchant is used to etch the silicon wafer on some specified points to fabricate a final geometry. Common anisotropic etchants for silicon are [43]:

- Alkali hydroxide solutions, specially KOH, NaOH, CsOH, and Tetra Methyl Ammonium Hydroxide (TMAH).
- EDP, a mixture of ethylenediamine ($NH_2(CH_2)_2NH_2$), pyrocatechol ($C_6H_4(OH)_2$) and water. There is more process flexibility when using EDP; however, the

handling of the etchant is more complicated since it is a toxic material and must be refluxed.

- Hydrazine, N_2H_4, mixed with water.

Anisotropic etchants, such as EDP and KOH, preferentially etch the {100} and {110} planes and stop on {111} planes.

A detailed investigation of exposed planes after etching silicon on 19% and 25% TMAH is presented on Appendix A. According to the results of this study, it can be seen that most of the times fabrication of square shape pins with high aspect ratios on a silicon wafer is not feasible by using TMAH as an etchant in both Si {100} and Si {110} wafers. There is only one miniature chance to fabricate square vertical pins with high aspect ratio (depends on the etching time) and a specific design for the mask on both Si {100} and Si {110} by using TMAH, but these pins do not have uniform vertical walls after all the processing time.

As a consequence, it can be said that fabrication of square pins with common anisotropic etchants for silicon is nearly unfeasible especially for some specific designs such as micro heat exchanger, which previously described in this chapter.

4.8.2. Fabrication of Square Shape Pins with LIGA Technology.

LIGA (an acronym from German words for lithography, electroplating, and molding) is a micromachining technology originated in the early 1980s at the Karlsruhe Nuclear Research Center and is a fabrication process for high aspect ratio microstructures [42]. This method includes these major process steps:

- Step1, as originally implemented, highly parallel x-rays from a synchrotron are incident on a mask patterned with high Z absorbers. The absorbers on the mask are thick enough to prevent the penetration of x-rays. In the open areas of the mask, the radiation passes through and exposes PMMA (poly methyl methacrylate) resist.
- Step 2, the resist is then developed to create a high aspect ratio, parallel wall model.
- Step 3, the resulting PMMA mold is used to produce a metal part by electroplating in the developed regions. The electroplating is either the final step in the process or the electroplated part is used as a mold for replication from another material such as plastic or ceramic.
- Step 4, the PMMA is dissolved leaving a three dimensional micro part. Individual micro parts can be separated from the base plate if desired.

By using the penetrating power of x-rays from a synchrotron, LIGA allows the fabrication of structures which have vertical dimensions from hundreds of microns to millimeters and horizontal dimensions which can be as small as microns. These are 3-D microstructures defined by 2-D lithographic patterns. The height-to-width ratio capability is relevant to the manufacturing of miniature components that can withstand high pressure and temperature, and can transfer useful forces or torques. The material flexibility also offers opportunities to fabricate miniature components using LIGA instead of precision machining approaches such as wire EDM. The feature definition, radius, and side wall texture using LIGA are superior to current precision machining techniques. The fabrication steps are illustrated on figure 4-18.

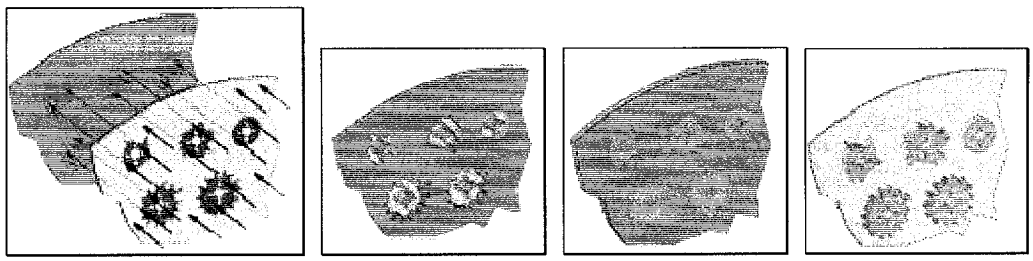

Figure 4-18. Fabrication steps in LIGA [42].

The LIGA method generally uses Nickel or Permalloy (NiFe) as the electro deposited material. Subsequent injection molding usually uses plastics.

A schematic of layers that can be used in fabrication with LIGA method are presented on figure 4-19.

The advantages of LIGA process are:

- Ability to fabricate arbitrary cross sectional shapes (figure 4-20).
- Ability to fabricate sub micro structural details.
- Ability to fabricate structures with extreme high aspect ratios.
- Ability to fabricate structures with vertical and smooth sidewalls.
- Wide variety of materials can be used in LIGA.

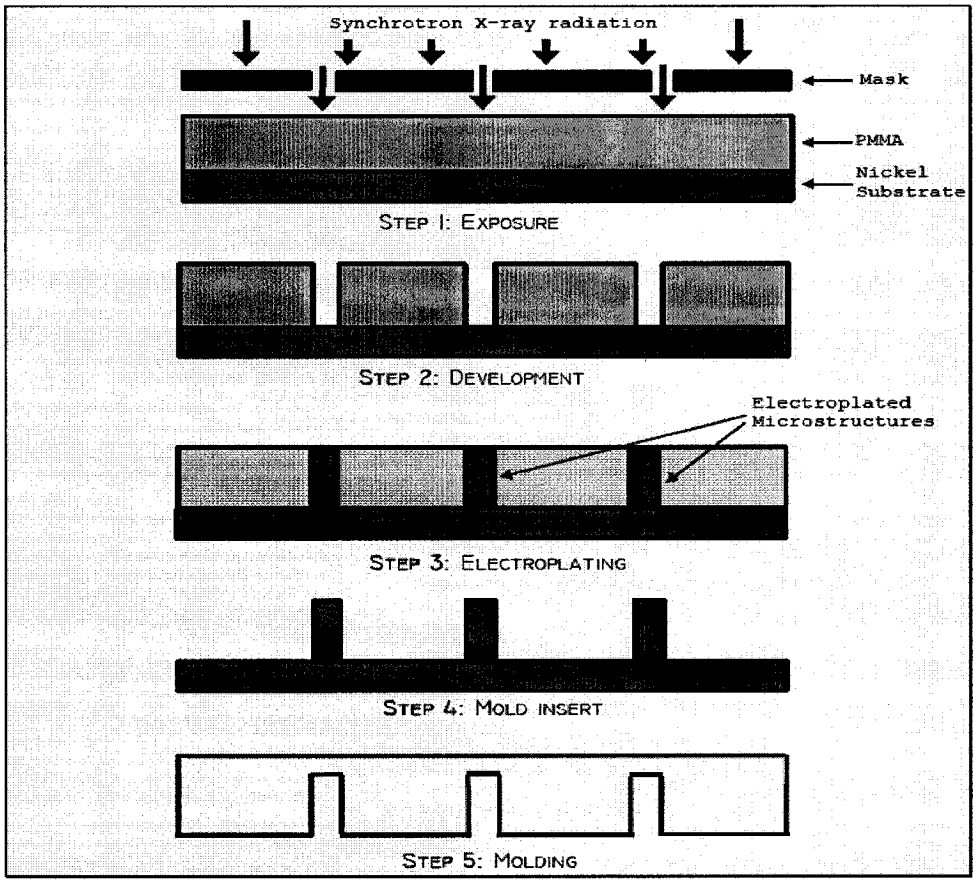

Figure 4-19. Layers used In LIGA Fabrication method [47].

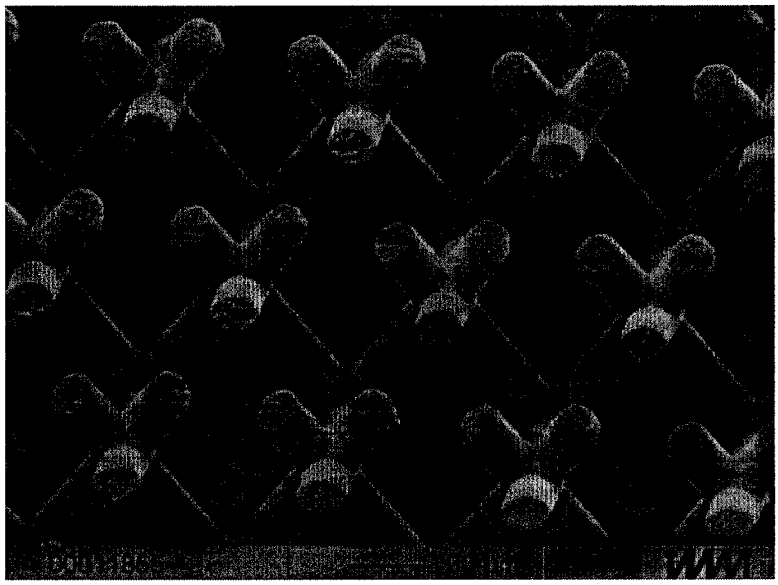

Figure 4-20. A fabricated structure by LIGA process [48].

4.8.3. Fabrication of Square Shape Pins with DRIE Technology

Bulk micromachining process technology is currently undergoing a revolution driven by the incorporation of deep reactive-ion-etching (DRIE) of silicon as a replacement for orientation-dependent (wet) etching. The traditional wet etches limit the range of structures, shapes, and minimum geometries because they rely on the crystallographic orientation of the wafer as described in part 4.8.1 and Appendix A. DRIE eliminates many of these restrictions, allowing 90-degree sidewall angles (which reduce device size) and randomly shaped linear geometries (figure 4-21). The DRIE process can also produce structures with high-aspect-ratios similar to those produced by LIGA.

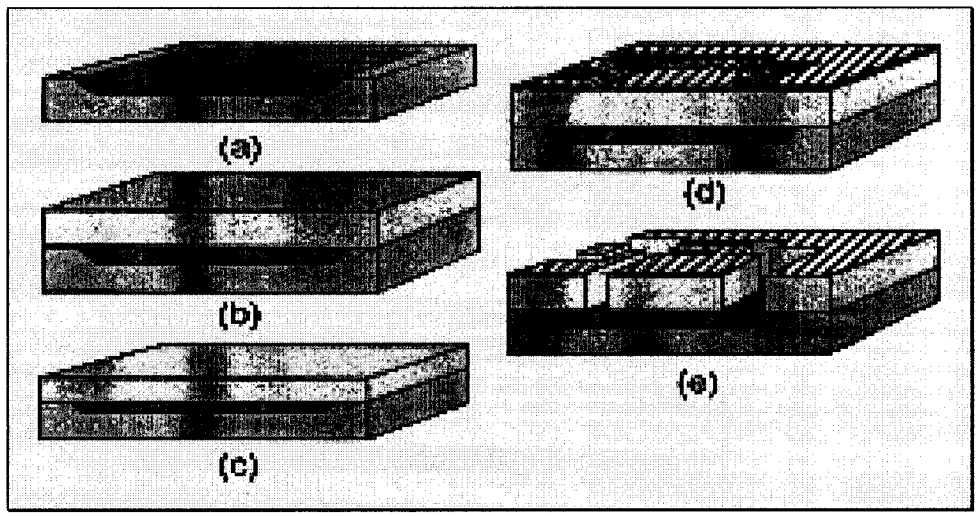

Figure 4-21. Generalized process flow for silicon fusion bonding and deep reactive-ion etching (DRIE). (a) A cavity is etched in the bottom wafer. (b) A second wafer is fusion bonded onto the bottom wafer, forming buried cavities. (c) The top wafer is polished down to the desired final thickness. (d) The metallization and patterning is done along with the DRIE masking and patterning. (e) The DRIE etch through the top wafer into the buried cavity releases the microstructures. [44]

DRIE bulk micromachining can be implemented in many ways, from single wafer, diaphragm, or structured devices, to more complex bonded wafer structures. This method

can also be used with other devices and wafer stacks to produce an entirely new class of bulk micromachined silicon devices.

There are two basic processes for DRIE; the Bosch process and the cryogenic process. The Bosch process is used when an isotropic process is required (figure 4-22 a) and the cryogenic process (figure 4-22 b), can be used when a sloped profile is required. Silicon nanostructure fabrication is also possible in conjunction with e-beam lithography.

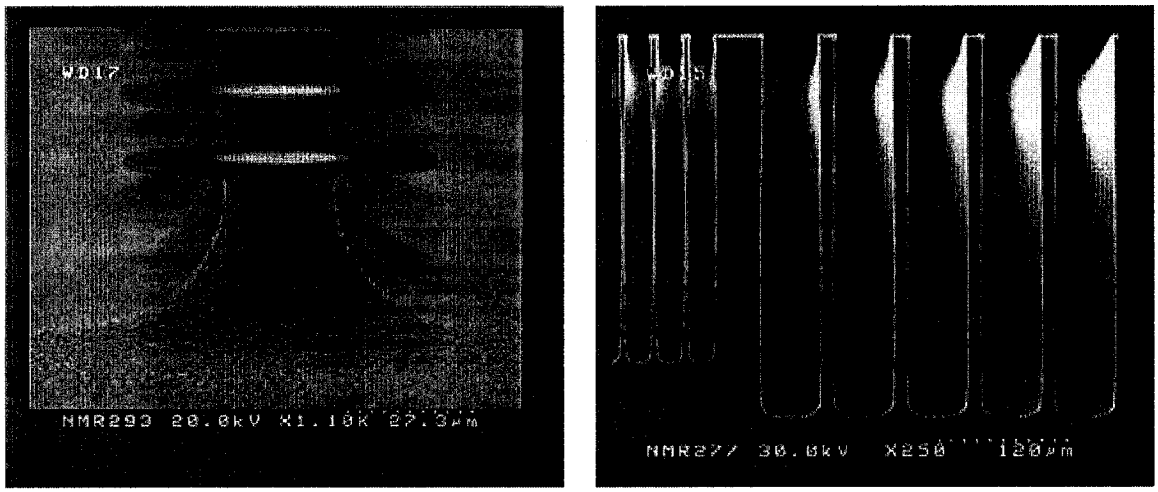

(a) (b)

Figure 4-22. (a) Isotropic etch of silicon using silicon dioxide as a mask (Bosch method), (b) High etch rate deep (3-400mm) etch of silicon (Cryogenic process) [45].

4.9. Summary

It can be concluded that:

- For two pins of the same material with different geometries (square and circular) and equal hydraulic diameter (D_h) and height (greater volumetric geometries for the square pins as a consequence), which are built on a surface in contact with the same flowing fluid the amount of transferred heat from the square pin to the flowing fluid is higher than the circular pin.

- Considering equal contact surface area between the heat source and the flowing fluid:
  - Increasing the number of pins on a surface at any L/t (*height of the pin/ thickness of the base*) increases the total amount of thermal heat flux from the surface (figure 4-6).
  - Increasing the number of pins for a specific value of *L/t* is followed by decreasing the dimension of the pins (hydraulic diameter) in contrast with their height (figure 4-6).
  - The amount of transferred heat flux is increasing by decreasing the longitudinal pitch between the pins, which is agreeable with the results of experimental investigations of A. Zukauskas and R. Ulinkas [30].
- Both simulation and analytical results show some increase in the amount of the transferred heat flux by increasing the number of pins on a surface (figure 4-17).
- In effective temperature of the fluid, this temperature is increasing from the entrance through the length of the heat exchanger chip and as a result, the amount of transferred thermal energy should decrease since it is proportional to the temperature difference between the base and the fluid (equation 2-1). However, due to increasing of the contact surface and the density of the pins through the length of the channel there will be a balance between these two phenomena and consequently, a uniform transformation of thermal energy and temperature distribution is expected inside the device. This is one the advantages of this design which enables compact structures for the electronic circuits with more homogeneous compactness.

- These results are in agreement with the expectation of *X. Yin and H. H. Bau (1995)* [12], to use non-uniform pin arrangement such that the cross sectional resistance increases by increasing the density of pins throughout the channel to minimize thermal resistance of heat exchanger.
- The staggered banks of pins are recommended for the design options because of flexibility in changing the longitudinal pitch.
- When air is used as a coolant fluid, the total transferred heat and heat flux from each region are at least 1.929W and 5.787W/cm^2, 2.768 W and 8.305W/cm^2, 3.608W and 10.824W/ cm^2 and 4.449W and 13.346W/ cm^2 for the base temperatures of 40°, 50°, 60° and 70° respectively.
- This design at least transfer 5.78 W/cm^2 heat flux by the conduction to the flowing air, which is 45% more than the experimental results of Christophe Marques and Kevin W. Kelly (4 W/cm^2)[46], when air is used as a coolant.
- Higher heat flux could be achieved by using another cooling fluid such as water and the fluid under the same design conditions can absorb higher amount of thermal energy from the silicon base.
- DRIE (cryogenic process) fabrication method can be used to fabricate these types of micro heat exchangers on silicon. Such process would enable fabrication of slightly tapered pylons that would be capable to face the pressure force induced by the flowing fluid.
- LIGA fabrication method can be used to fabricate the same design on metals, which have high thermal conductivities.
- The advantages of this design are:

- Transferring higher amount of thermal energy to the flowing fluid in comparison with previous works.
- Ability to absorb uniform amount of thermal energy through the length of the channel and consequently uniform temperature distribution on the base.
- Smaller volumetric size.
- Usage of a microelectronics compatible material for fabrication.

CHAPTER 5

Conclusion, Contributions and Suggestions for Future Works

5.1. Conclusion

The main conclusions of this thesis are summarized below:

- When air is used as the flowing fluid, the suggested values for the temperature as the boundary condition on the solid-fluid borders in the ANSYS area are:
    - The average value of the flowing fluid temperature and the base temperature for low Reynolds numbers ($Re \leq 5.6 \times 10^3$).
    - And for high Reynolds numbers ($Re \geq 5.6 \times 10^3$), it can be found from figures 2-14, 2-15 and 2-16 by using equation 2-8 in chapter 2.
    - By using the above suggestions for any convection heat transfer problem, one can get less than 10% variation between the ANSYS results and experiments.

- For two pins of the same material with different geometries (square and circular) and equal hydraulic diameter (D_h) and height (greater volumetric geometries for the square pins as a consequence), which are built on a surface in contact with the same flowing fluid, square pins are the recommended geometry to be used in heat transfer mechanisms versus circular pins (the amount of the transferred heat from the square pin to the flowing fluid is at least 27% higher than for the circular pin).

- The suggested orientation angle for the square pins in convection heat transfer is 45° (at the same boundary conditions, the amount of transferred heat is 2-10% higher in comparison to 0° orientation angle).
- The simulation process, which carried out in chapter 2 is suggested for designing heat exchangers based on forced convection mechanism.
- Decreasing the longitudinal pitch between the pins is another recommended subject for better performance of heat exchanger (the more decrease in the longitudinal pitch between the pins, the more heat will transfer).
- Decreasing longitudinal pitch between the pins is accompanied by increasing the number of pins on a surface with a specific area, which is another recommended factor for designing of the heat exchangers (thermal transferred heat flux is increasing by increasing the number of pins on a surface).
- The staggered banks of pins are recommended for the design options because of flexibility in changing the longitudinal pitch.
- Using liquids such as ordinary refrigerants is recommended for higher considered heat dissipations ($50W/cm^2$ or more).
- DRIE (cryogenic process) fabrication method is the recommended fabrication method for these types of micro heat exchangers on silicon (such process would enable fabrication of slightly tapered pylons that would be capable to face the pressure force induced by the flowing fluid).
- LIGA fabrication method is the recommended method to fabricate the same design on metals, which have high thermal conductivities.

5.2. Contributions

This work has the following contributions:

- Come up with concept of a micro heat exchanger based on the extended surface principle that could be used in applications that require high extraction and small area/ volume (micro system).
- Build a model that is capable to simulate the heat transfer phenomena under variable geometric and topographic configuration.
- Calibrate the simulation program based on experimental results.
- Carry out tests on simplified scaled up models to be used for calibration of the simulation programs.
- Elaborate an optimal configuration of a micro heat exchanger based on the simulation results as well as on the results presented in the open literature.
- Evaluate the performance of the proposed micro heat exchanger versus standard convective surfaces (Appendix B).
- Propose a method and algorithm based on the experimental data for clarification of the temperature boundary conditions for different ranges of the Reynolds number in a system.

5.3. Suggestions for Future Works

This thesis investigates the criteria of designing an efficient Micro Heat Exchanger that can be used as a subject to much further investigations for the near future. These subjects are:

- Multi-objective optimization based on the specific requirements of the heat exchanger.
- Fabrication of this design using LIGA on metals or DRIE on silicon.
- Apply new experimental techniques to the fabricated devices to check the efficiency and performances of the device and compare the results with the simulation and analytical results of this work.
- Carry out new investigations on the feasibility of using alternate fluids such as practical refrigerants and use them in this design as well as comparing the output results with previous experiments.
- Fabricate this type of heat exchanger as a heat pipe and evaluate the heat extraction performances.
- Evaluation of the effect of the contamination in this design and the future designs.

References

[1]. I. Hapke, H. Boye, J. Schmidt and Y. Staate, "Evaporation In Micro Heat Exchangers", J. of Chemical Engineering and Technology, V. 23, N. 6, pp. 496-500, 2000.

[2]. S. Kakac and H. Liu, "Heat Exchangers: Selection, Rating, and Thermal Design", second edition, Boca Raton: CRC Press, 2002.

[3]. F. P. Incropera and D. P. Dewitt, "Introduction to Heat Transfer ", New York: Wiley, 1995.

[4]. D. B. Tuckerman and R. F. W. Pease, IEEE Electron Dev. Lett. EDL-2, 126 (1981).

[5]. V. K. Samalam, "Convection Heat Transfer in Micro Channels", J. of Electronic Materials, Vol. 18, No. 5, 1989.

[6]. Y. Asako and M. Faghri, "Three Dimensional Heat Transfer Analysis of Array of Heated Square Blocks", Int. J. Heat Mass Transfer, Vol. 32, No. 2, pp. 395-405, 1989.

[7]. A. Weisberg, H. H. Bau and J. Zemel, "Micro Heat Exchangers", Microstructures, Sensors and Actuators, Winter Annual Meeting of the American Society of the Mechanical Engineers (ASME), 1990.

[8]. W. Bier, W. Keller, G. Linder, D. Seidel and K. Schubert, "Manufacturing and Testing of a Compact Micro Heat Exchanger with High Volumetric Heat Transfer Coefficients", ASME, Dynamic System and Control Division, v 19, pp. 189-197, Microstructures, Sensors and Actuators, Winter Annual Meeting of the ASME, 1990.

[9]. J. H. Wang, H. Y. Yeh and R. J. Shyu, "Thermal-Hydraulic Characteristic of Micro Heat Exchangers", DSC-Vol. 32, Micromechanical Sensors, Actuators, and Systems, Winter Annual Meeting of the ASME, 1991.

[10]. A. Bejan and A. M. Morega, "Optimal Arrays of Pin Fins and Plate Fins in Laminar Forced Convection", J. of Heat Transfer, Vol. 115, pp. 75-81, Feb. 1993.

[11]. C. R. Fredrich and S. D. Kang, "Micro Heat Exchangers Fabricated by Diamond Machining", Precision Engineering, Vol. 16, N. 1, January 1994.

[12]. X. Yin and H. H. Bau, " Micro Heat Exchangers Consisting of Pin Arrays", Cooling and Thermal Design of Electronic Systems, ASME International Mechanical Engineering Congress, HTD-Vol. 319/EEP-Vol. 15, pp. 59-66, 1995.

[13]. N. Kuan, "Experimental Evaluation of Micro Heat Exchangers Fabricated in Silicon", ASME National Heat Transfer Conference, Vol.9, pp. 131-136, 1996.

[14]. *B.* V. Antohe, J. L. Lage, D. C. Price and R. M. Weber, "Numerical Characterization of Micro Heat Exchangers Using Experimentally Tested Porous Aluminum Layers", Int. J. of Heat and Fluid Flow, Vol. 17, No. 6, December 1996.

[15]. http://www.knowledge.omron.com/, search for "E5CN Temperature Controller User Manual" © 2002 Omron Electronics LLC.

[16]. http://www.national.com/, search for products > Analog-Thermal-Management > Analog > LM35 > Download "LM35 Precision Centigrade Temperature Sensors", September 1997.

[17]. A. Bejan, A. D. Kraus, "Heat Transfer Handbook ", 2003.

[18]. S. Y. Yoo, J. H. Park, Chang Hwan Chung and Moon Ki Chung, "An Experimental Study on Heat/Mass Transfer from a Rectangular Cylinder", J. of Heat Transfer, Vol. 125, pp. 1163-1169, December 2003.

[19]. T. Igarashi, "Characteristics of The Flow around Rectangular Cylinders (The case of The Angle of Attack 0 deg) ", Bull. JSME, 28, pp. 1690-1696, 1985.

[20]. T. Igarashi, "Heat Transfer from a Square Prism to an Air Stream", Int. J. Heat Mass Transfer, 28, pp. 175-181, 1985.

[21]. T. Igarashi, "Local Heat Transfer from a Square Prism to an Air Stream", Int. J. Heat Mass Transfer, 29, pp. 774-784, 1986.

[22]. T. Igarashi, "Fluid Flow and Heat Transfer Around Rectangular Cylinders (The Case of Width/Height Ratio of a Section of 0.33-1.5) ", Int. J. Heat Mass Transfer, 30, pp. 893-901, 1987.

[23]. R. J. Goldstein, S. Y. Yoo and M. K. Chung, "Convective Mass Transfer from a Square Cylinder and Its Base Plate", Int. J. Heat Mass Transfer, 33, pp. 9-18, 1990.

[24]. R. J. Goldstein, S. Y. Yoo and M. K. Chung, "Effects of Angle of Attack on Mass Transfer from a Square Cylinder and its Base Plate", Int. J. Heat Mass Transfer, 36, pp. 371-381, 1993.

[25]. A. Zukauskas and j. Ziugzda, "Heat Transfer of a Cylinder in Cross flow", Hemisphere Publishing Co., 1985.

[26]. G.W.C. Kaye and T.H. Laby, "Tables of Physical and Chemical Constants", Longman, London, UK, 15th edition, 1993.

[27]. D. R. Lide, "Chemical Rubber Company Handbook of Chemistry and Physics", CRC Press, Boca Raton, Florida, USA, 79th edition, 1998.

[28]. J. A. Dean, "Lange's Handbook of Chemistry", McGraw-Hill, New York, `USA, 14th edition, 1992.

[29]. A. M. James and M.P. Lord, "Macmillan's Chemical and Physical Data", Macmillan, London, UK, 1992.

[30]. A. Zukauskas, R. Ulinkas, "Heat Transfer in Tube Banks in Cross flow", Hemisphere Publishing Corporation, United States of America, 1988.

[31]. A. P. Fraas, "Heat Exchanger Design", John Wiley & Sons Inc., United States of America, 1989.

[32]. J. E. Hesselgreaves, "Compact Heat Exchangers", Pergamon, UK, 2001.

[33]. D. Q. Kern and A. D. Kraus, "Extended Surface Heat Transfer", McGraw-Hill Inc., United States of America, 1972.

[34]. J. H. Seely and R.C. Chu, "Heat Transfer in Microelectronic Equipment", Marcel Dekker Inc., New York, 1972.

[35]. J. E. Shigley and Charles R. Mischke, "Mechanical Engineering Design", McGraw-Hill Inc., New York, 2001.

[36]. G. T. A. Kovacs, "Micromachined Transducers Sourcebook", McGraw-Hill Inc., New York, 1998.

[37]. M. Z. Elalamy, "Modeling of Anisotropic Etching of Silicon in Tetra-Methyl Ammonium Hydroxide: Anomalies Due to Facet Boundary Effects", A Thesis in the Department of Electrical and Computer Engineering at Concordia University, Montreal, Quebec, Canada, July 2002.

[38]. N. Tirole, D. Haudsen, P. Blind, M. Froelicher and L. Caudriot, "Three-Dimensional Silicon Electrostatic Linear Microstructure", Sensors and Actuators, A 48 (1995) 145-150.

[39]. S. M. Sze, "Semiconductor Sensors", 1994.

[40]. A. Pandy, "Experimental Investigation and Modeling of Anisotropic Etching of Silicon in Tetra Methyl Ammonium Hydroxide", A Thesis in the Department of Electrical and Computer Engineering at Concordia University, Montreal, Quebec, Canada, April 2002.

[41]. L. Landsberger, "Micro Transducers Technology", Course Book in Department of Electrical and Computer Engineering at Concordia University, Montreal, Quebec, Canada, 2002.

[42]. A. M. Morales, J. M. Hruby, T. Bennett, M. Bankert, D. R. Boehme, W. D. Bonivert, J. Hachman, S. Griffiths, R. H. Nilson, A. Ting, L. Domeier and P. Keifer, "LIGA", 4th International Conference on the Commercialization of Microsystems, Dortmund, Germany, July 10th, 1999 (Sandia National Laboratories, http://www.ca.sandia.gov/liga/process.html).

[43]. T. Fukunda and W. Menz, "Micro Mechanical Systems Principles and Technology", Hand Book of Sensors and Actuators, Volume 6, 1998.

[44]. Committee on Advanced Materials and Fabrication Methods for Microelectromechanical Systems, National Materials Advisory Board, Commission on Engineering and Technical Systems, National Research Council, "Microelectromechanical Systems: Advanced Materials and Fabrication Methods", NMAB-483, National Academy Press, Washington D.C., 1997 (Web site of National Academies Press www.nap.edu/openbook, Article Number 0309059801).

[45]. C. Hibert and J. O'Brien, "Shape Control in Deep Silicon Etching Using an STS_HRM Inductively Coupled Plasma Reactor", Annual Scientific Reports of NMRC Ireland's ICT research Institute, 2003 (www.nmrc.ie/publications).

[46]. C. Marques and K. W. Kelly, "Fabrication and Performance of a Pin Fin Micro Heat Exchanger", J. of Heat Transfer, Vol. 126, No. 3, pp. 434–444, June 2004©2004 ASME.

[47]. J. P. Tuma, "The Rapid Template Fabrication Process for Production a LIGA Heat Exchanger Bonded to a Mechanical Seal", A Thesis in the Department of Mechanical Engineering at Louisiana State University, August 2003.

[48]. G. Feiertag, W. Ehrfeld, H. Fremuth, H. Kolle, H. Lehr, M. Schmidt, M. M. Sigalas, C. M. Soukoulis, G. Kiriakidis, T. Pedersen, J. Kuhl and W. Koenig, "Fabrication of Photonic Crystals by Deep X-Ray Lithography", Appl. Phys. Lett. 71 (11), 15 September 1997.

[49]. M. J. Mudou, "Fundamental of Microfabrication", CRC Press, 1997 (ISBN 0-8493-9451-1).

[50]. T. R. Hsu, "MEMS and Microsystems, Design and Manufacture", McGraw-Hill Inc., Boston, 2002 (ISBN 0-07-239391-2).

Appendix A

Wet Etching Fabrication Methods in MEMS

This Chapter covers the wet etching fabrication methods that can be used to produce long and narrow square pins on a silicon wafer used in micro heat exchanger with square pins such as what was described on part 4.5 of chapter 4 and explains the limitations of simple fabrication methods such as etching methods using 19% and 25% Tetra Methyl Ammonium Hydroxide (TMAH) to produce these types of pins on silicon wafers.

One of the simplest and basic fabrication methods is An-isotropic Etching of silicon in TMAH. Section A.1 covers the feasibility study of fabrication of high aspect ratio square shape pins on Si {100} and Si {110} wafers, which are used on fabrication of Micro Heat Exchanger with non-uniform pin arrays. The basic theories of this part are related to theories of semiconductors and physical properties and behaviors of silicon crystal [41].

A.1. Fabrication Feasibility of Square Shape Pins on Si {100} and Si {110} wafers with 19% and 25% TMAH.

25% TMAH and 19% TMAH are used as the etchant liquids, which is one of the most useful wet etchants for silicon etching, to find out the shape of fabricated pins on different etching times. TMAH is a non toxic material and is relatively low cost and the important thing about it is that typical masking layers show excellent resistance to etching against it. For example silicon dioxide and silicon nitride films exhibit typical etch rates in the range of 0.05 to 0.25 nm/min [36].

Six different mask designs and orientations of the mask edge have been used to figure out the final fabricated shapes. These mask designs are described in the following paragraphs:

- Design 1 for Si {100} is a square mask with large beams on the corners illustrated in figure A-1 (a). The edges of the square part are parallel and perpendicular to the wafer flat and they have deviation angle of $\delta = 45^{\circ}$.
- Design 2 for Si {100} is a square mask with large beams on the corners illustrated in figure A-1 (b). The edges of the square part have orientation of 45° and 135° with respect to the wafer flat and they have deviation angle of $\delta = 0^{\circ}$.

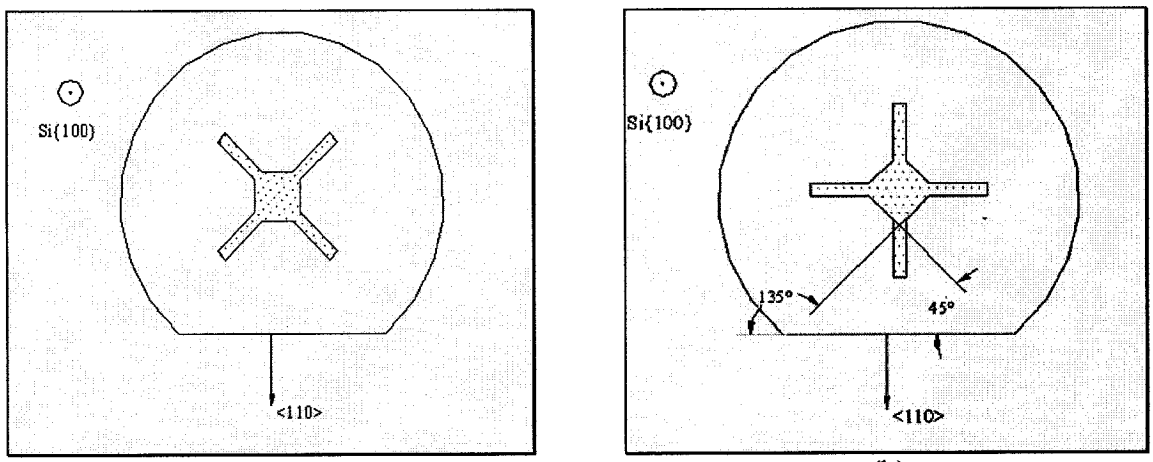

Figure A-1. Designs for Si {100}, (a) Design 1, (b) Design 2

- Design 3 for Si {110} is a square mask with large beams on the corners illustrated in figure A-2 (a). The edges of the square part are parallel and perpendicular to the wafer flat and they have deviation angle of $\delta = 35.26^{\circ}$.
- Design 4 for Si {110} is a parallelogram mask with large beams on the corners illustrated in figure A-2 (b). The edges of the parallelogram have deviation angle of $\delta = 54.74^{\circ}$ and all of them are in the direction of <111>.

- Design 5 for Si {110} is a square mask with large beams on the corners illustrated in figure A-2 (c). The edges of the square part have orientation of 45° and 135° with respect to the wafer flat and they have deviation angle of $\delta = 9.74^\circ$.
- Design 6 for Si {110} is a parallelogram mask with large beams on the corners illustrated in figure A-2 (d). The edges of the parallelograms are parallel with the {111} planes and they have deviation angle of $\delta = 54.76^\circ$.

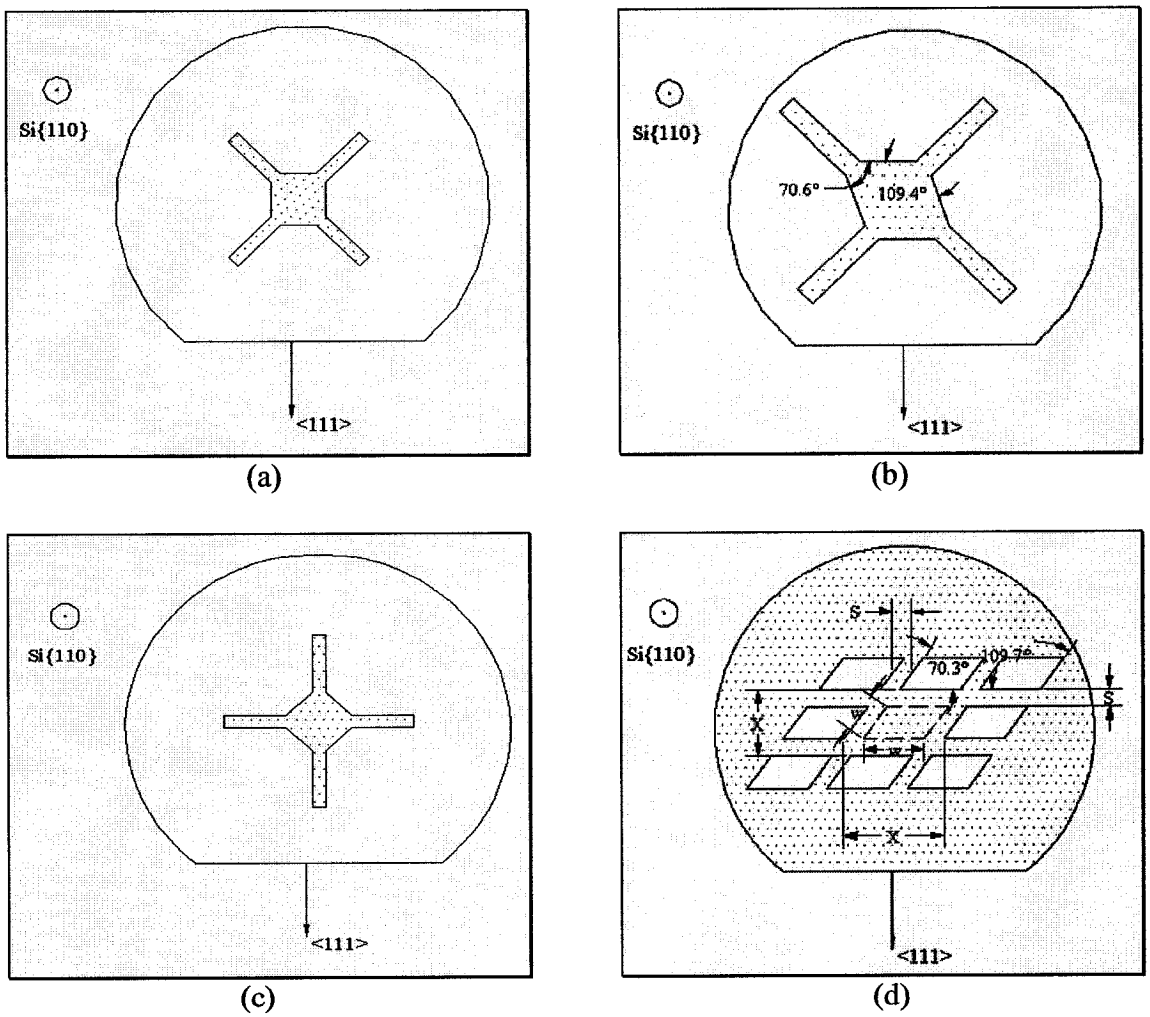

Figure A-2. Designs for Si {110}, (a) Design 3, (b) Design 4, (c) Design 5, (d) Design 6

The beams on the corners of square shape masks help to postpone etching of the fast etch planes on the convex corners. In the following part details of calculations for each mask

are presented and the results compared with experimental investigations of Moulay-Ziyad Elalamy [37] and Anand Pandy [40].

A.1.1. Design 1 for Si {100} on 25% TMAH

According to the experimental investigations of Moulay-Ziyad Elalamy [37] for etching of Si {100} in 25% TMAH, values of theoretical rotation angles θ versus mask edge deviation angle δ for Si {100} are equal to (figure A-3):

K-inclined: $$\theta_K = arctg(\frac{1}{\sqrt{2}\cdot tg\delta}) - 35.26 \quad 0 \le \delta \le 45^\circ \qquad \text{(A-1)}$$

P-inclined: $$\theta_P = 35.26 - arctg(\frac{tg\delta 1}{\sqrt{2}}) \quad 0 \le \delta \le 45^\circ \qquad \text{(A-2)}$$

$$\Rightarrow \quad \theta_K = 0 \quad \& \quad \theta_P = 0$$

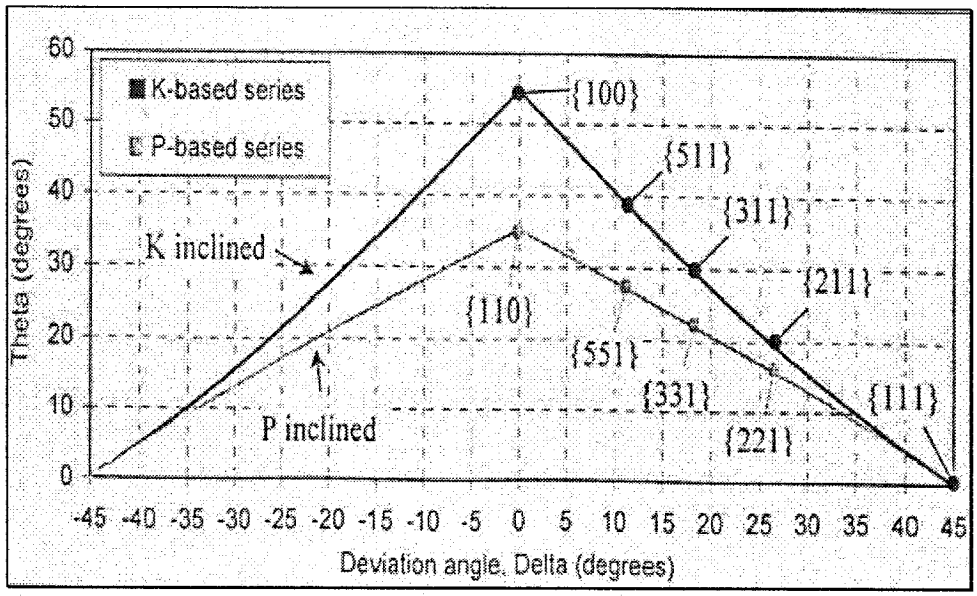

Figure A-3. Theoretical rotation angle (θ) versus mask edge deviation angle (δ) for Si {100} [37]

Also the theoretical inclination angles versus mask edge deviation angle can be calculated from figure A-4:

K-inclined: $$\alpha_K = arctg(\frac{1}{\sin\delta}) \quad 0 \le \delta \le 45^\circ \tag{A-3}$$

P-inclined: $$\alpha_P = arctg(\frac{1}{\cos\delta}) \quad 0 \le \delta \le 45^\circ \tag{A-4}$$

$$\Rightarrow \quad \alpha_K = 54.74^\circ \quad \& \quad \alpha_P = 54.74^\circ$$

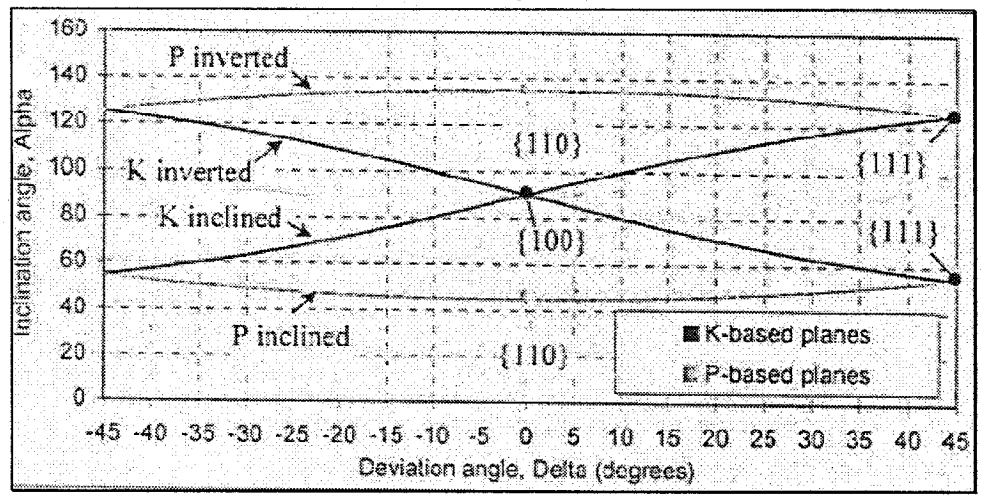

Figure A-4. Theoretical inclination angle (α) versus mask edge deviation angle (δ) for Si {100} [37]

Under etch rates of mask edges in $\delta = 45^\circ$ can be calculated using figure A-5:

$$UER_K = UER_P = 0\mu m / hr$$

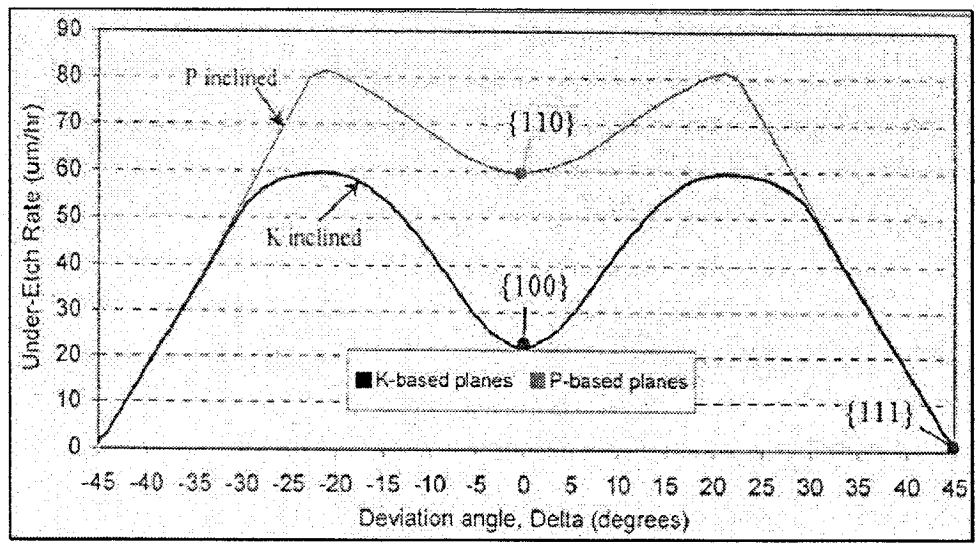

Figure A-5. Ideal under etch rates for P and K-based planes of Si {100} at 25% TMAH [37]

The last item, which is used to predict the fabricated facets after etching, is Etch Rate of the inclined planes (figure A-5). It can be seen that:

$$ER_K = ER_P = 0\mu m/hr \qquad \& \qquad ER_{\{100\}} = 22\mu m/hr$$

According to the above results, it can be seen that the shape of etched silicon in 25%TMAH using Design 1 for the mask will be a facet that has inclination angle of 54.74° as illustrated in figure A-6 and the length of the facet ($L1$) will be equal to:

$$L_1 \sin\alpha = D \Rightarrow \qquad L_1 = \frac{D}{\sin 54.74}$$

The depth of the etched wafer (D) after etching time (T) will be equal to [41]:

$$D = ER_{\{100\}} \cdot T \Rightarrow \qquad D = 22 \cdot T$$

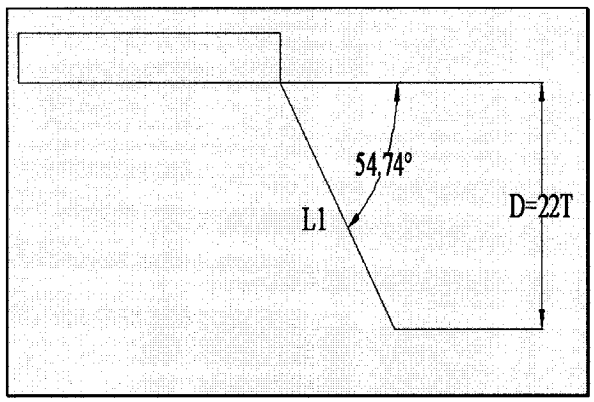

Figure A-6. Schematic of the facets for design 1 on Si {100} on 25% TMAH

By mixing the above equations, the relation between the length of the facet and etching time for this design is estimated from the following formula:

$$L_1 = 26.94 \cdot T$$

The exposed facets in this design are {111} family planes. Meanwhile fast etch planes start etching from the convex corners of the mask until thy reach {111} facets exposed

before on concave borders of the mask. In this case etching of fast etch planes will be stopped in their intersection with {111} planes reaching to concave area of the mask. If we put the wafer in 25% TMAH for a long time, the final shape of the pins will be a pyramid (figure A-7). For a limited etching time, we have that pyramid shape with some little facets of fast etch planes on the corners of the pyramid.

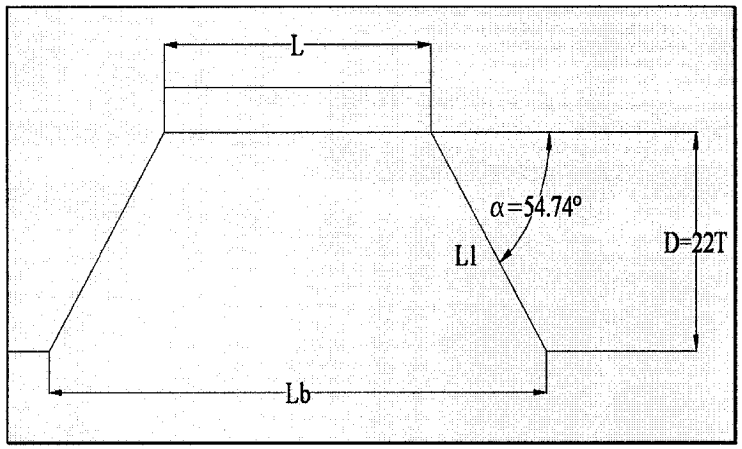

Figure A-7. Cross section of pins for design 1 on Si {100} on 25% TMAH

For this design the relation between the base-length (Lb) of the pins, which is the distance between each mask (distance between centers of the pins), with mask-length (L) is:

$$L_b = L + 2 \cdot L_1 \cdot \cos\alpha \Rightarrow \qquad L_b = L + 31.1 \cdot T$$

It can be seen that for $L = 50\mu m$ and T=5hr, L_b will be equal to $205.5\mu m$, which is a large value for the distance between the pins and as a consequence fabrication of more than nine pins in a space of 2mm (practical size for micro devices) is impossible. It means that for fabrication of more than 10 pins, which is the aim of this work, this mask design will not be a perfect choice.

A.1.2. Design 1 for Si {100} on 19% TMAH

According to the experimental investigations of Moulay-Ziyad Elalamy [37] for etching of Si {100} in 19% TMAH, all the analytical work is the same as part A.1.1 except for the etch rate of Si {100}. The estimated values are:

$\delta = 45^\circ$

K-inclined: $\theta_K = 0$ & $\alpha_K = 54.74^\circ$

P-inclined: $\theta_P = 0$ & $\alpha_P = 54.74^\circ$

Under Etch Rates can be found from figure A-8:

$$UER_K = UER_P = 0\mu m/hr \quad \& \quad ER_K = ER_P = 0\mu m/hr$$

Also the Etch Rate of Si {100}, which has rotation angle of 54.74° is equal to:

$$ER_{\{100\}} = 32\mu m/hr$$

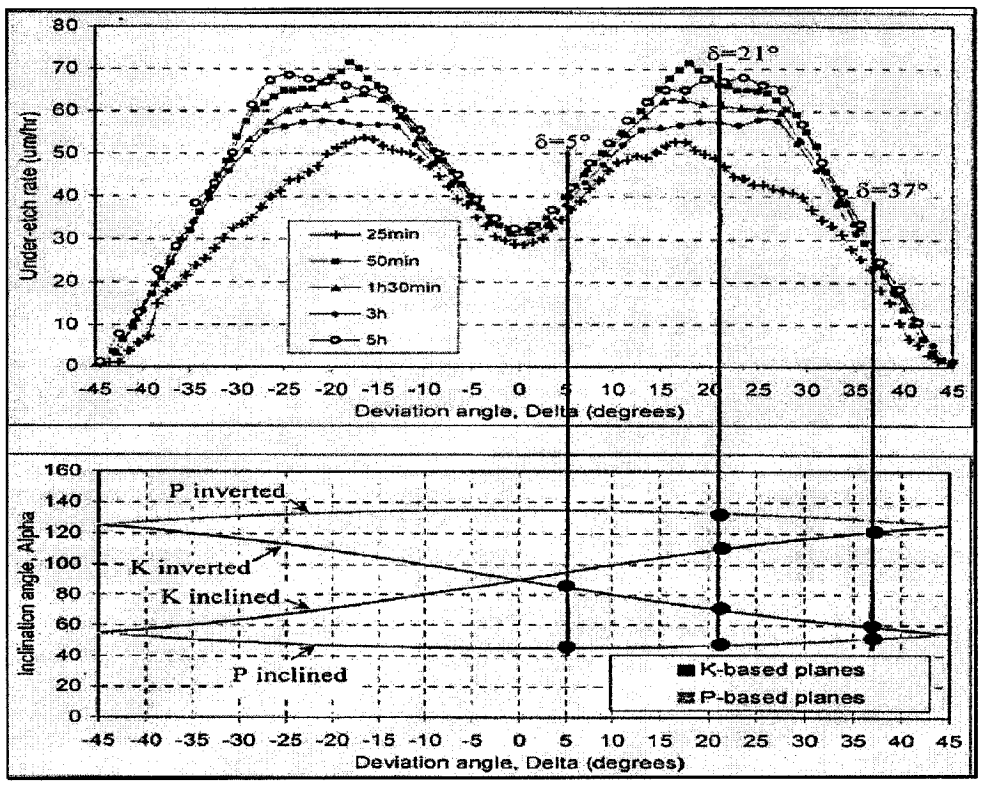

Figure A-8. Under etch rate evolution with time for Si {100} on 19% TMAH

According to the above results, it can be concluded that the shape of Si {100} after etching in 19%TMAH will be a facet that has inclination angle of 54.74° (figure A-9) and the length of the facet (L_1) will be equal to:

$$L_1 \sin\alpha = D \Rightarrow \qquad L_1 = \frac{D}{\sin 54.74}$$

The depth of the etched wafer (D) after etching time (T) will be equal to [41]:

$$D = ER_{\{100\}} \cdot T \Rightarrow \qquad D = 32 \cdot T$$

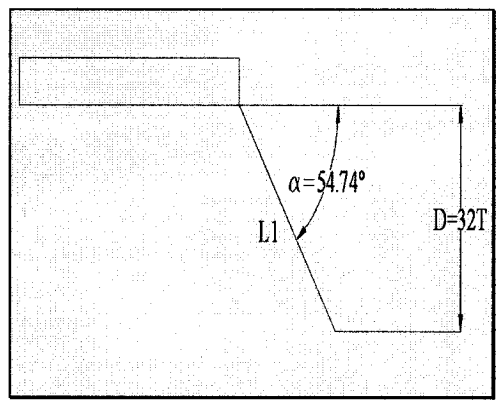

Figure A-9. Schematic of the facets for design 1 on Si {100} on 19% TMAH

By mixing the above equations, the relation between the length of the facet and etching time will be found as:

$$L_1 = 39.2 \cdot T$$

These facets that will be exposed in this situation are {111} family planes, meanwhile fast etch planes start etching from the convex corners of the mask until thy reach {111} facets that were exposed on concave borders of the mask. Then etching of fast etch planes will be stopped in their intersection with {111} planes because they reach to a concave area and the shape of the pins will be like pyramids, if the wafer stayed in 19% TMAH for a long time like what happened for 25% TMAH. For a limited etching time, we have

that pyramid shape with some little facets of fast etch planes on the corners of the pyramid. In this condition the relation between the base-length (Lb) of the pins with mask-length (L) is:

$$L_b = L + 2 \cdot L_1 \cdot \cos\alpha \Rightarrow \qquad L_b = L + 39.2 \cdot T$$

It can be seen that for $L = 50\mu m$ and T=5hr, L_b will be equal to $246\mu m$, which is a large value for the distance between the pins and as a consequence fabrication of more than seven pins in a space of 2mm (practical size for micro devices) is impossible. It means that for fabrication of more than 10 pins, which is the aim of this work, this mask design will not be a perfect choice.

A.1.3. Design 2 for Si {100} on 25% TMAH

The analytical results for deviation angle 0 are:

$\delta = 0^\circ$

K-inclined: $\theta_K = 54.74^\circ$ & $\alpha_K = 90^\circ$

P-inclined: $\theta_P = 35.26^\circ$ & $\alpha_P = 45^\circ$

$UER_K = 22\mu m/hr \;\&\; UER_P = 60\mu m/hr$

$ER_K = 22\mu m/hr \;\&\; ER_P = 45\mu m/hr$

Also the Etch Rate of Si {100}, with rotation angle of 54.74° in 25% TMAH is equal to:

$$ER_{\{100\}} = 22\mu m/hr$$

According to the above results, it can be concluded that the shape of facets after etching in 25% TMAH will be exposed like the schematic in figure A-10.

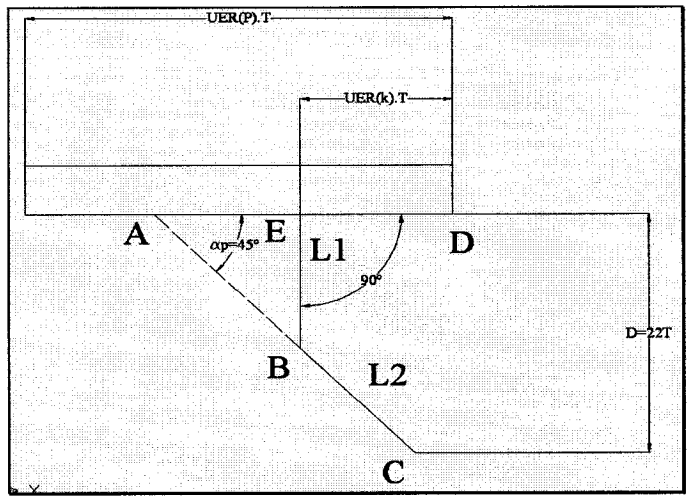

Figure A-10. Schematic of the facets for design 2 on Si {100} on 25% TMAH

From the geometry in figure 5-10 can conclude that:

$$D = L_1 + L_2 \sin\alpha_p$$

From $\Delta ABE \Rightarrow$ $\quad L_1 = (UER_P - UER_K) \cdot T \cdot tg\,\alpha_p$

$$Ac = \frac{D}{\sin\alpha_P} \Rightarrow AB + L_2 = \frac{D}{\sin\alpha_P} \Rightarrow \qquad L_2 = \frac{D}{\sin\alpha_P} - \frac{(UER_P - UER_k)\cdot T}{\cos\alpha_P}$$

By applying analytical results in the above equations, it can be seen that:

$$L_1 = 38 \cdot T \qquad \& \qquad L_2 = -16\sqrt{2 \cdot T}$$

Thus from the above results, it can be seen that in any etching time the K-inclined plane will be exposed before the other one and the second facet will be hidden under the etched Si {100} facet. The main reason is that $L_1 = 22 \cdot T$ is greater than D in any etching time. Also according to the investigations of Moulay-Ziyad Elalamy [37], for $\delta = 5^\circ$ in some specific etching times (50 minutes), two facets will be exposed after etching but mostly there is just one exposed vertical facet. This means that the above theoretical results are in agreement with the real results of experiments (figure A-11).

The exposed facets in this case are {100} family planes. Fast etch planes start exposing from the convex corners of the mask until they reach {100} facets that were exposed on concave borders of the mask. Then etching of fast etch planes will be blocked by {100} planes. Shape of the pins will be like a vertical square if we put the wafer in 25% TMAH for a long time. For a limited etching time, we have that square shape pins with two other facets of fast etch planes on the corners of the square pins as illustrated in figure A-12.

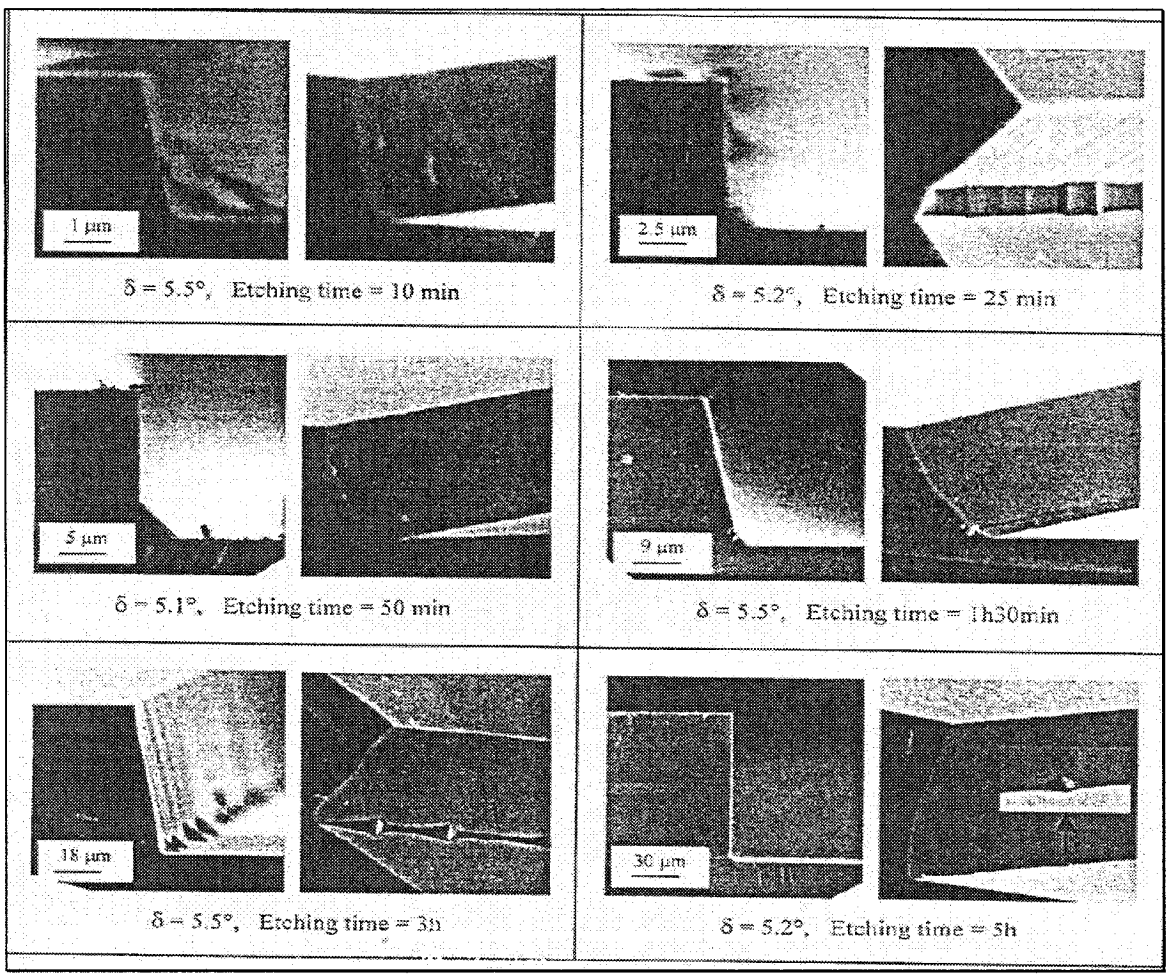

Figure A-11. Exposed facets for δ=5° for Si {100} on 25% TMAH [37]

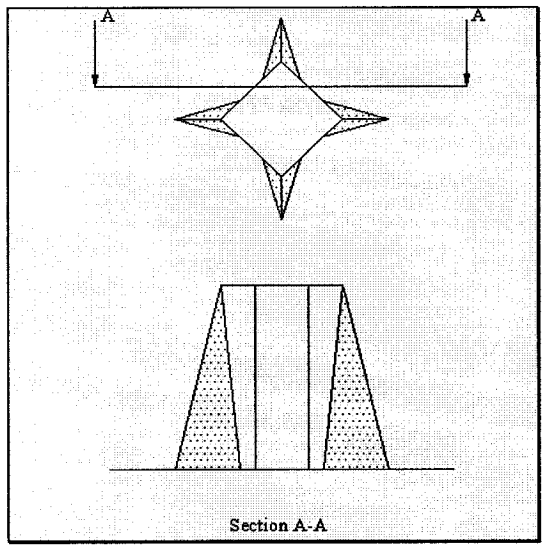

Figure A-12. Exposed facets for mask design 2 of Si {100} on 25% and 19% TMAH

A.1.4. Design 2 for Si {100} on 19% TMAH

Analytical results for this design at deviation angle 0 are:

$\delta = 0^\circ$

K-inclined: $\theta_K = 54.74^\circ$ & $\alpha_K = 90^\circ$

P-inclined: $\theta_P = 35.26^\circ$ & $\alpha_P = 45^\circ$

$$UER_K = UER_P = 32\mu m / hr$$

$$ER_K = 32\mu m / hr \;\&\; ER_P = 48\mu m / hr$$

In addition the Etch Rate of Si {100}, with rotation angle of 54.74° in 19% TMAH is equal to:

$$ER_{\{100\}} = 32\mu m / hr$$

From the above results, it can be concluded that the shape of facets ought to be like the schematic in figure A-13.

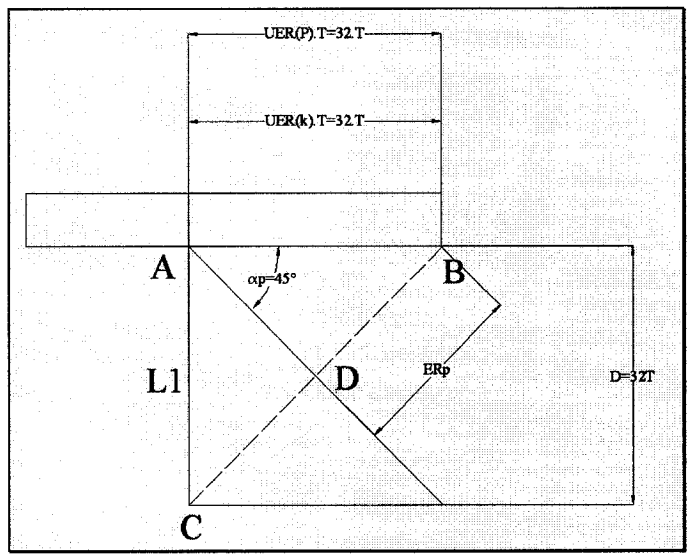

Figure A-13. Exposed facets for mask design 2 of Si {100} on 19% TMAH

According to this geometry, line AB is equal to under etch rate and etch rate of the vertical K-inclined facets along with under etch rate of 45° P-inclined facet. Line AC is the depth of etched Si {100}. It is expected that one of the facets must be hidden under others. To find this the length of BC is estimated and compared with ER_p which is equal to line BD in this geometry:

$$AB = AC = UER_K.T = ER_K.T = ER_{\{100\}}.T = 32.T$$

$$BC = \frac{AB}{COS(90-\alpha_P)} \Rightarrow BC = \frac{AB}{COS45°} = AB.\sqrt{2} \Rightarrow BC = 45.25T$$

$$BD = ER_P.T \Rightarrow BD = 48.T$$

Clearly BD is greater than BC and the real shape of exposed planes ought to be similar to schematic in figure A-14. As a consequence the 45° P-inclined facet will be hidden beneath the K-inclined facet and the depth of etched Silicon as well as the K-inclined facet will be equal to:

$$L1 = AE = D \Rightarrow L1 = 32.T$$

These exposed facets in this situation are {100} family planes, at the same time fast etch planes start etching from the convex corners of the mask until they reach {100} facets that were exposed on concave borders of the mask. Then etching of fast etch planes will be stopped in their meeting point with {100} planes because they reach to a concave area and the shape of the pins will be a like a vertical square if the wafer remains in 19% TMAH for a long time. For a limited etching time, square shape pins with two other facets of fast etch planes on the corners of the square pins will be exposed as it is shown in figure A-12.

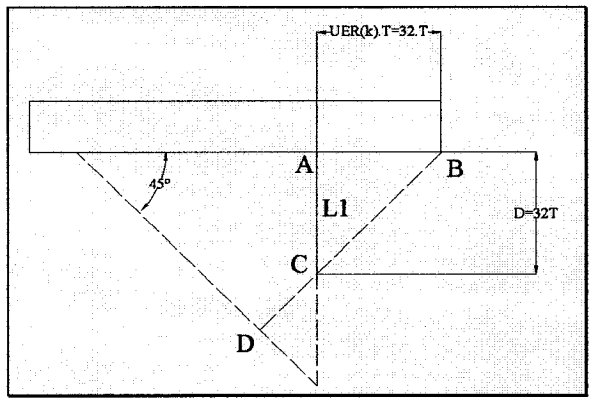

Figure A-14. Real exposed facets for mask design 2 of Si {100} on 19% TMAH

A.1.5. Design 3 for Si {110} on 25% TMAH

For this case, it can be seen that the edges of square shape mask have deviation angle of $\delta = 54.74$ and $\delta = 35.26$. In addition values of theoretical rotation angles θ versus mask edge deviation angle δ for Si {110} can be calculated from graphs on figure A-15. The inclination angles, versus mask edge deviation angle can be calculated from graphs on figure A-16 as well. UER (Under Etch Rate) of mask edges in $\delta = 54.74°$ and $\delta = 35.26$ can be found from graphs on figure A-17 and Etch Rate of the inclined planes can be calculated from figure A-18.

K1-inclined: $\theta_{K1} = \text{atan}\left(\tan\delta - \frac{1}{\sqrt{2}}\right) - 35.26°$ $54.74° \le \delta \le 90°$ (5)

K2-inclined: $\theta_{K2} = \text{atan}\left(\frac{1}{\sqrt{2}} + \tan\delta\right) - 35.26°$ $0 \le \delta \le 90°$ (6)

K-vertical: $\theta_{K} = 54.74° - \delta$ $0 \le \delta \le 54.74°$ (7)

P-inclined: $\theta_{P} = 35.26° - \text{atan}\left(\frac{1}{\sqrt{2}} - \tan\delta\right)$ $0 \le \delta \le 54.74°$ (8)

P-vertical: $\theta_{P} = \delta - 54.74°$ $54.74° \le \delta \le 90°$ (9)

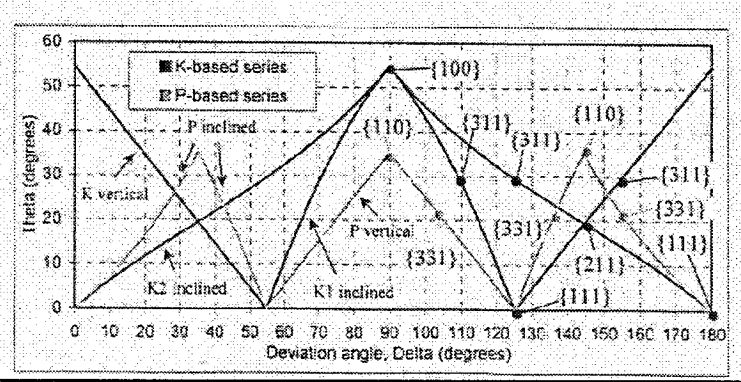

Figure A-15. Theoretical rotation angle (θ) versus deviation angle (δ) for Si {110} [37]

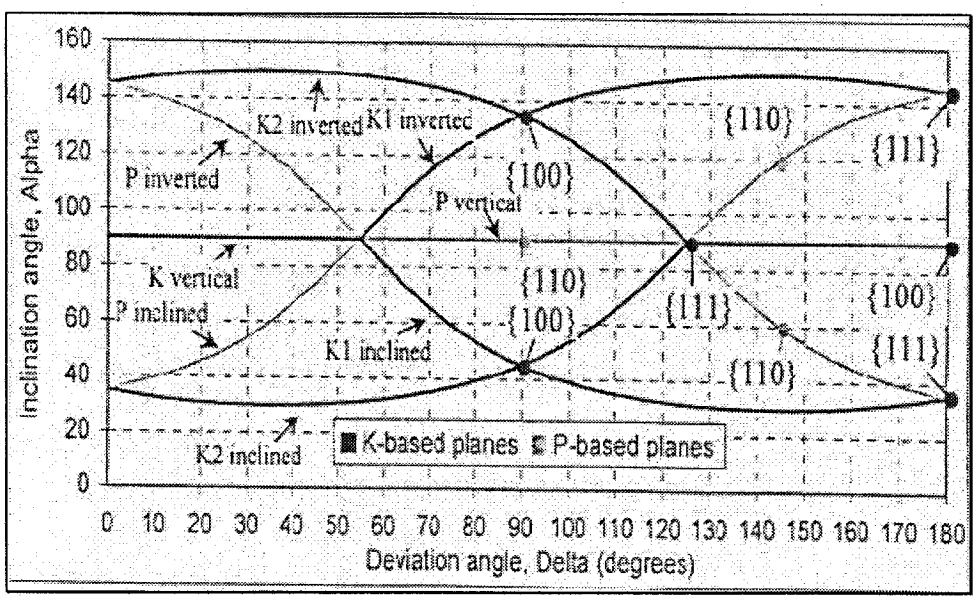

Figure A-16. Theoretical inclination angle (α) versus deviation angle (δ) for Si {110} [37]

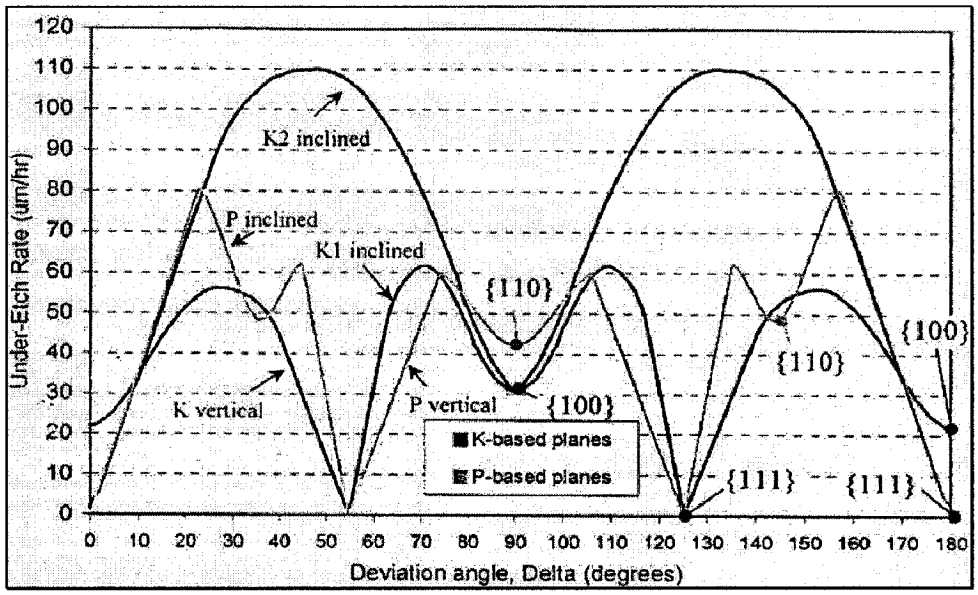

Figure A-17. Ideal under etch rates for Si {110} at 25% TMAH [37]

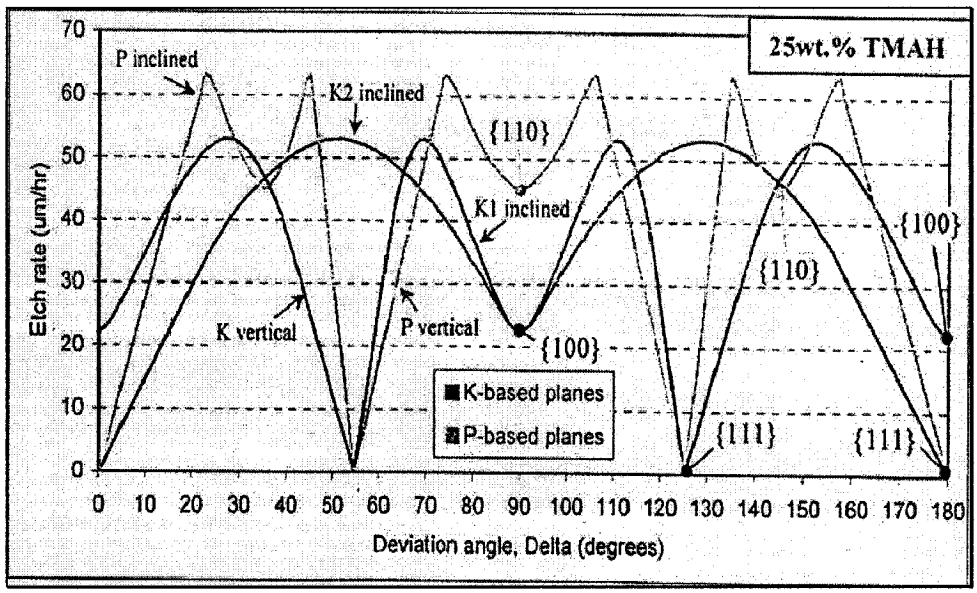

Figure A-18. Ideal etch rate construction for P-based and K-based series for Si {110} at 25% TMAH [37]

So for this particular case it can be seen that:

$\delta = 54.74 \Rightarrow$ K2-inclined and K-vertical: $\theta_K = 30°$

$\delta = 35.26 \Rightarrow$ K-inclined and K-vertical: $\theta_K = 20°$

P-inclined: $\theta_K = 35°$

$\delta = 54.74 \Rightarrow$ K2-inclined: $\alpha_K = 31°$

K-vertical: $\alpha_K = 90°$

$\delta = 35.26 \Rightarrow$ K2-inclined: $\alpha_K = 31°$

P-inclined: $\alpha_K = 60°$

K-vertical: $\alpha_K = 90°$

$\delta = 54.74 \Rightarrow$ $UER_{K2inclined} = 102\mu m/hr \;\&\; UER_{K\,vertical} = 0\mu m/hr$

$\delta = 35.26 \Rightarrow$ $UER_{pinclined} = 53\mu m/hr$

$UER_{K\,vertical} = 48\mu m/hr$

$UER_{K2inclined} = 90\mu m/hr$

$\delta = 54.74 \Rightarrow$ $ER_k = 48\mu m/hr$

$\delta = 35.26 \Rightarrow$ $ER_k = 47\mu m/hr$

$ER_p = 42\mu m/hr$

From the above results for the mask edges with deviation angle 54.74°, it can be concluded that the shape of facets ought to be like the schematic in figure A-19.

The depth of the etched wafer D, after etching time T will be equal to [41]:

$$D = ER_{\{110\}} \cdot T \Rightarrow \qquad D = 45 \cdot T$$

From the geometry in figure A-19, It can be seen that:

$$D = L_1 + L_2 \sin 31 \qquad \& \qquad L_1 = (UER_K) \cdot T \cdot tg31 = 63 \cdot T$$

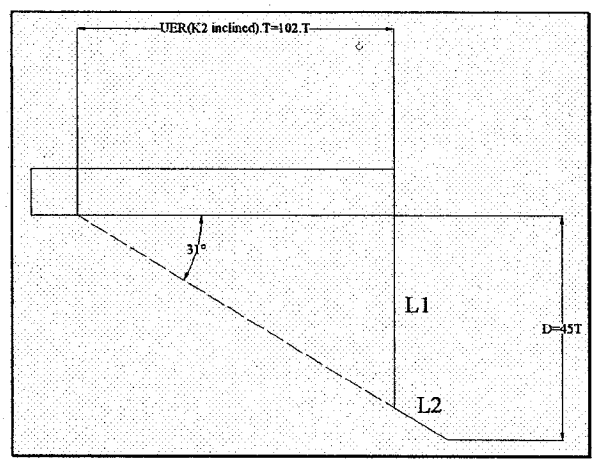

Figure A-19. Theoretical schematic of the facets for design 3 for Si {110} in 25% TMAH (δ=54.74°)

According the above results L_1 is greater than D and it can be concluded that at any etching time the K-vertical plane is the exposed plane and the second facet will be hidden under it. The final shape of the exposed facets for this design is illustrated in figure A-20.

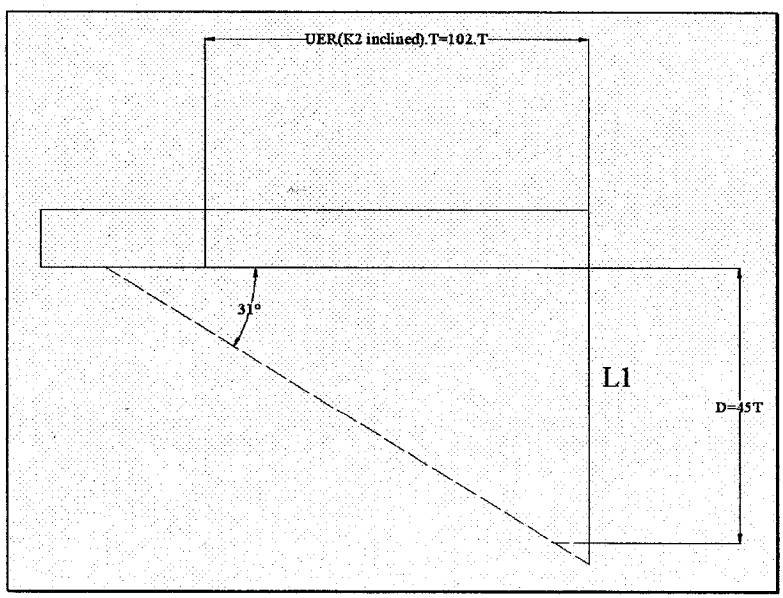

Figure A-20. Real schematic of the facets for design 3 and 4 for Si {110} in 25% TMAH (δ=54.74°)

For the mask edges with deviation angle 35.26°, it can be seen that three different facets are the results of final exposure (figure A-21).

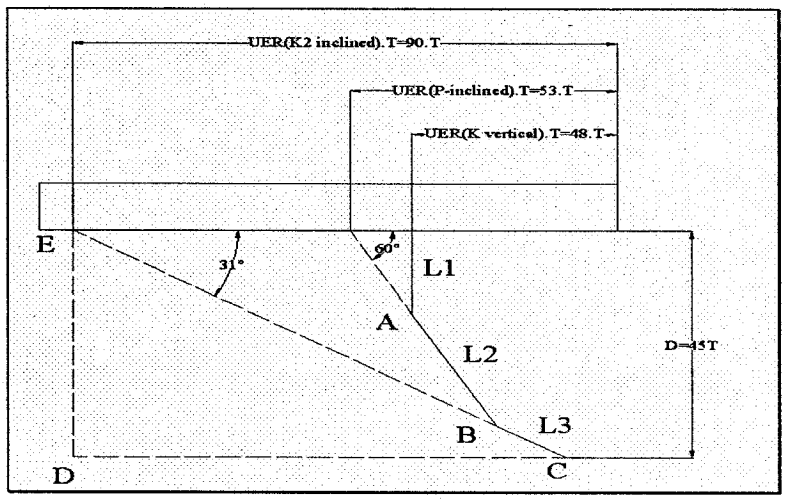

Figure A-21. Real schematic of the facets for design 3 for Si {110} in 25% TMAH (δ=35.26°)

A.1.6. Design 3 for Si {110} on 19% TMAH

For this design the edges of square shape mask have deviation angles of 54.74° and 35.26°. Using figures A-16, A-22 and A-23, the analytical results are:

$\delta = 54.74 \Rightarrow$ K2-inclined: $\theta_K = 30°$ & $\alpha = 36°$

$UER_{K2inclined} = 135 \mu m / hr$ & $ER_k = 70 \mu m / hr$

$\delta = 35.26 \Rightarrow$ K-inclined: $\theta_K = 20°$ & $\alpha = 30°$

$UER_{K2inclined} = 123 \mu m / hr$ & $ER_k = 60 \mu m / hr$

K-vertical: $\theta_K = 20°$ & $\alpha = 90°$

$UER_{K\,vertical} = 55 \mu m / hr$ & $ER_k = 48 \mu m / hr$

P-inclined: $\theta_p = 32°$ & $\alpha = 60°$

$UER_{P\,inclined} = 60 \mu m / hr$ & $ER_k = 60 \mu m / hr$

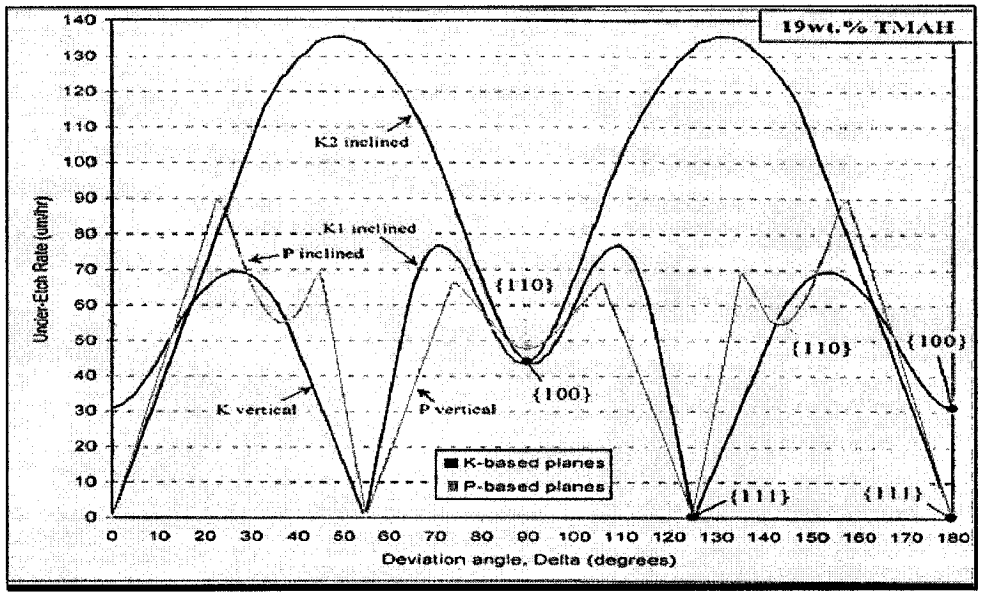

Figure A-22. Ideal under etch rate construction of P-based and K-based series for Si {110} in 19% TMAH [37]

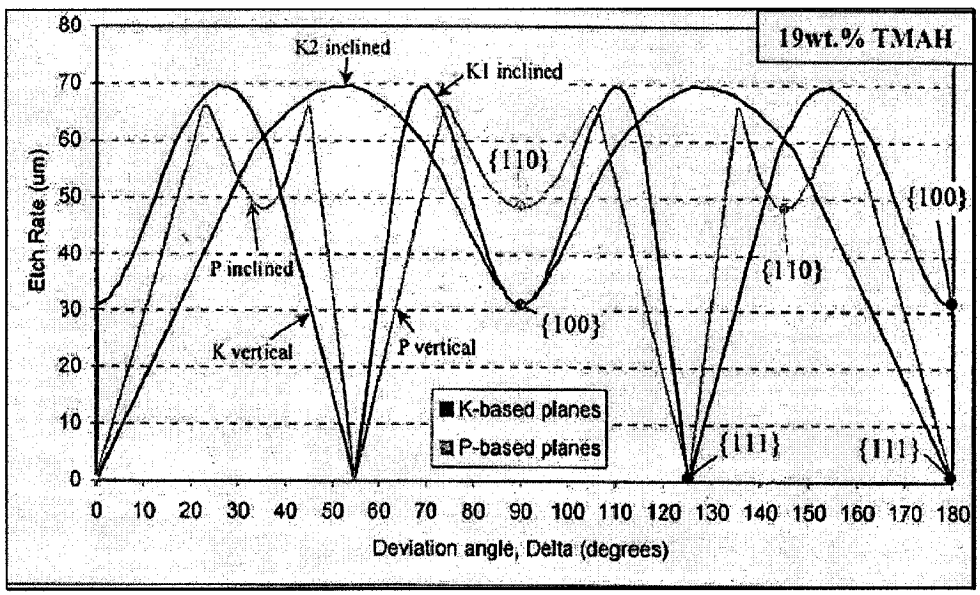

Figure A-23. Ideal etch rate construction of P-based and K-based series for Si {110} in 19% TMAH [37]

From the above analytical results, it can be seen that the exposed facets for this design after etching in 19%TMAH will be two facets as illustrated in figure A-24.

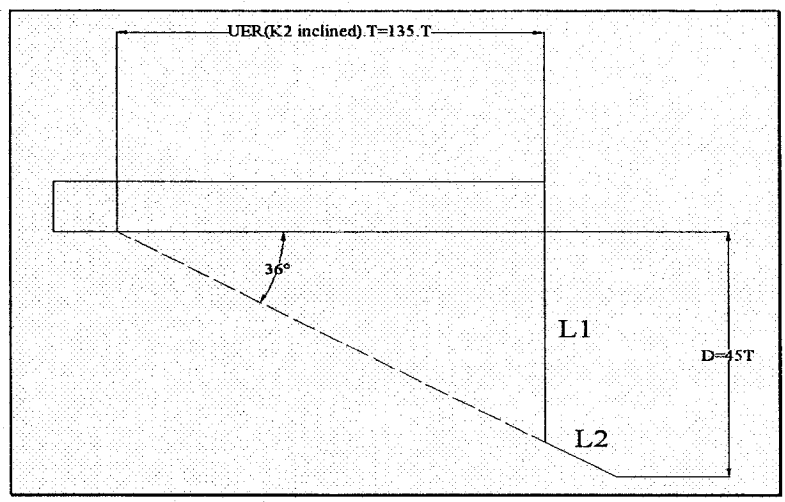

Figure A-24. Schematic of the facets for design 3 for Si {110} in 19% TMAH (δ=54.74°)

Theoretically the depth D of the etched Si $\{110\}$ wafer after etching time T is:

$$D = ER_{\{110\}} \cdot T \Rightarrow \qquad D = 45 \cdot T$$

From the geometry, it can be seen that:

$$D = L_1 + L_2 \sin 36 \qquad \& \qquad L_1 = (UER_K) \cdot T \cdot tg36 = 98 \cdot T$$

Therefore from the above results, it can be seen that $L1$ is greater than D in any etching time and the K-vertical plane will be exposed all the time and the second facet is hidden under it. The length of this facet is equal to the value of D. The final shape of the exposed facets for the mask edges with $\delta = 54.74$ is illustrated in figure A-25.

For the mask edges with $\delta = 35.26$, three facets are theoretically exposed. Two of them are hidden underneath the 60° P-inclined facet as illustrated in figure A-26.

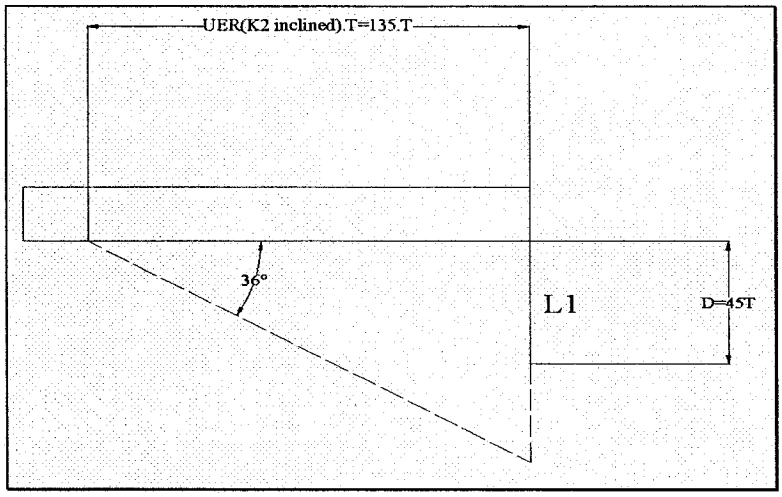

Figure A-25. Real schematic of the facets for design 3 and 4 for Si {110} in 19% TMAH (δ=54.74°)

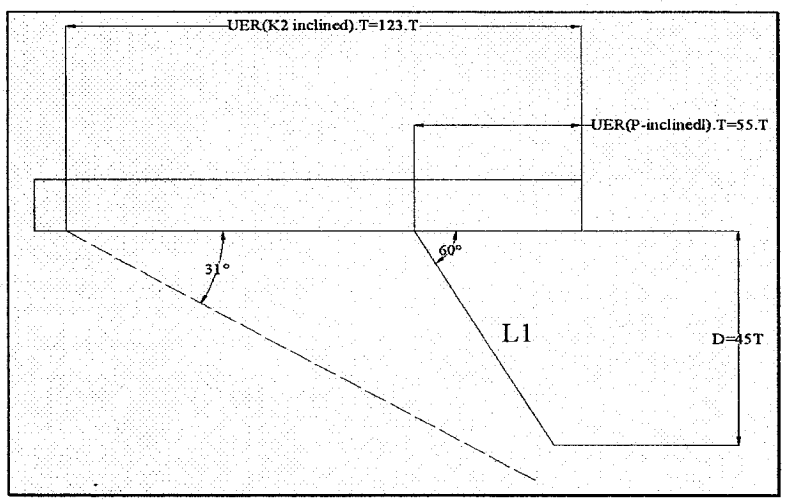

Figure A-26. Real schematic of the facets for design 3 for Si {110} in 19% TMAH (δ=35.26°)

But according to real experiments for δ=32.7, which is too close to δ=35.26 [37], all the three facets are exposed as illustrated in figure A-27.

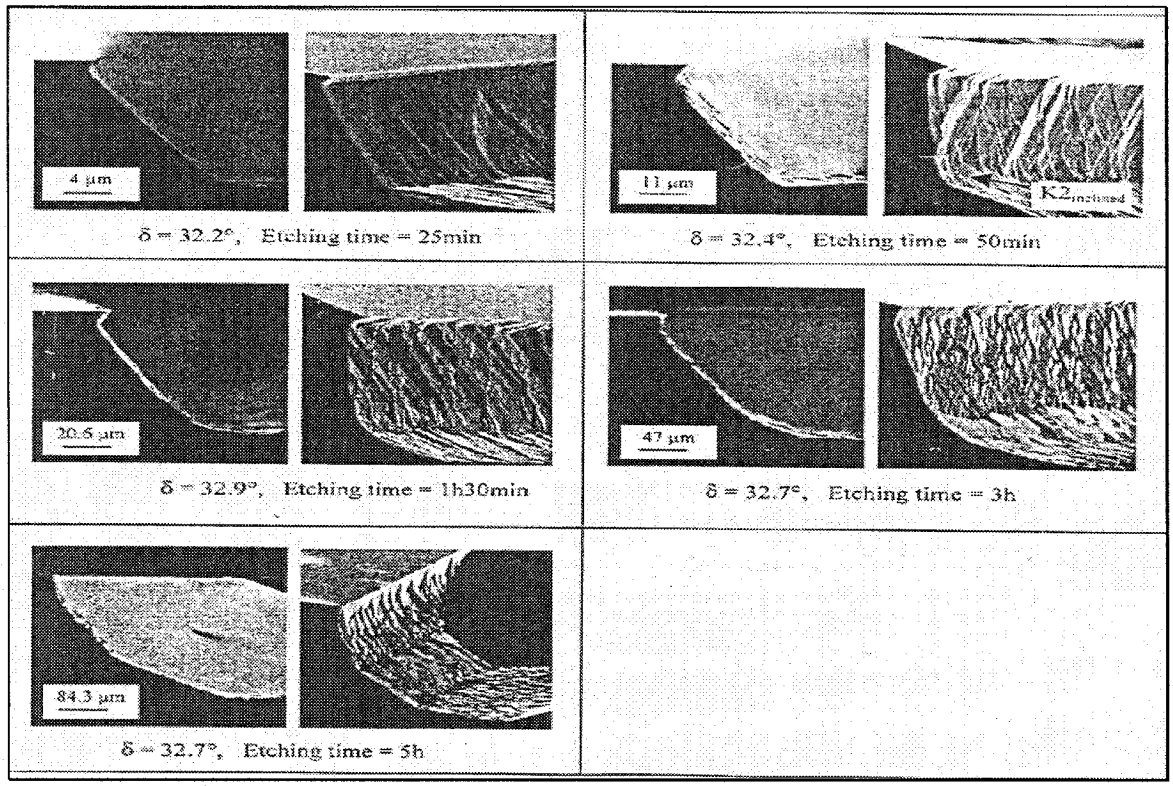

Figure A-27. Real schematic of the facets for design 3 for Si {110} in 19% TMAH (δ=32.7°) [37]

A.1.7. Design 4 for Si {110} on 25% TMAH

For this design the edges of square shape mask have deviation angles of 54.74°. Using figures A-15 through A-18, the analytical results are:

$\delta = 54.74 \Rightarrow$ K2-inclined and K-vertical: $\theta_K = 30°$

K2-inclined: $\alpha_K = 31°$

K-vertical: $\alpha_K = 90°$

$UER_{K2inclined} = 102\mu m/hr$ & $UER_{K vertical} = 0\mu m/hr$

$ER_k = 48\mu m/hr$

The depth D of the etched wafer after etching time T is:

$$D = ER_{\{110\}} \cdot T \Rightarrow \quad D = 45 \cdot T$$

From the above result, it can be seen that the exposed facets are similar to the exposed facets, which have been explained on part 5.1.5 (figure 5-20).

A.1.8. Design 4 for Si {110} on 19% TMAH

For this design the edges of square shape mask have deviation angles of 54.74°. Using figures 4-31, 4-37 and 4-38, the analytical results are:

$\delta = 54.74 \Rightarrow$ K2-inclined: $\theta_K = 30°$ & $\alpha = 36°$

$UER_{K2inclined} = 135 \mu m / hr$ & $ER_k = 70 \mu m / hr$

The depth D of the etched wafer after etching time T is:

$$D = ER_{\{110\}} \cdot T \Rightarrow \qquad D = 45 \cdot T$$

From the above result, it can be seen that the exposed facets are similar to the exposed facets, which have been explained on part A.1.6 (figure A-26).

A.1.9. Design 5 for Si {110} on 25% and 19% TMAH

For this design the edges of square shape mask have deviation angles of 9.74°. The analytical results are:

$\delta = 9.74 \Rightarrow$ K2-inclined: $\theta_K = 6.1°$ & $\alpha = 36°$

$UER_{K2inclined} = 36 \mu m / hr$ & $ER_k = 18 \mu m / hr$

K-vertical: $\theta_K = 44.74°$ & $\alpha = 90°$

$UER_{K vertical} = 36 \mu m / hr$

P-inclined: $\theta_p = 7.3°$ & $\alpha = 40°$

$UER_{pinclined} = 36 \mu m / hr$ & $ER_k = 22 \mu m / hr$

From the above results, it can be seen that the exposed facets are like the shape in figure A-28.

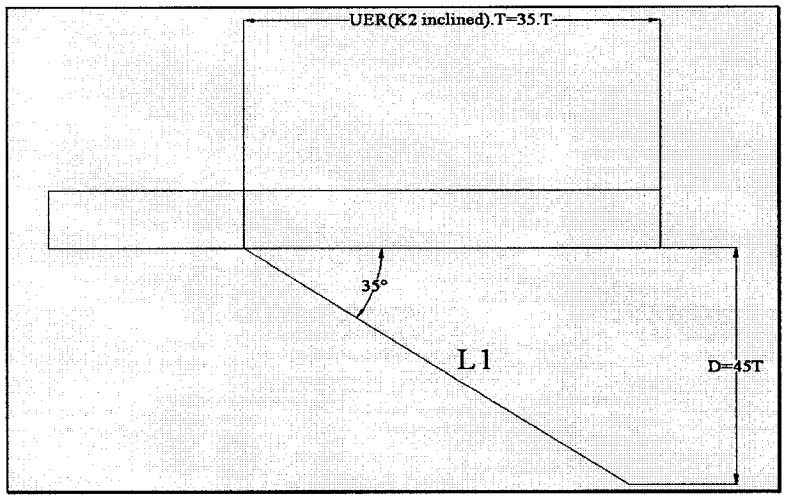

Figure A-28. Theoretical schematic of the facets for design 5 for Si {110} in 25% and 19% TMAH (d=9.74°)

The experimental results for d=12° on 25% TMAH [37] are shown in figure A-29. These results show that the exposed facets are the same as what have been expected with the analytical results for the first 30 minutes of etching time but after a long etching time the exposed facets from the left side of the mask reached to the right side and finally the exposed facets produce a groove shape. But the theoretical results are in good agreement with the experimental results.

From the above results, it can be seen that the exposed facets are like the shape in figure A-28.

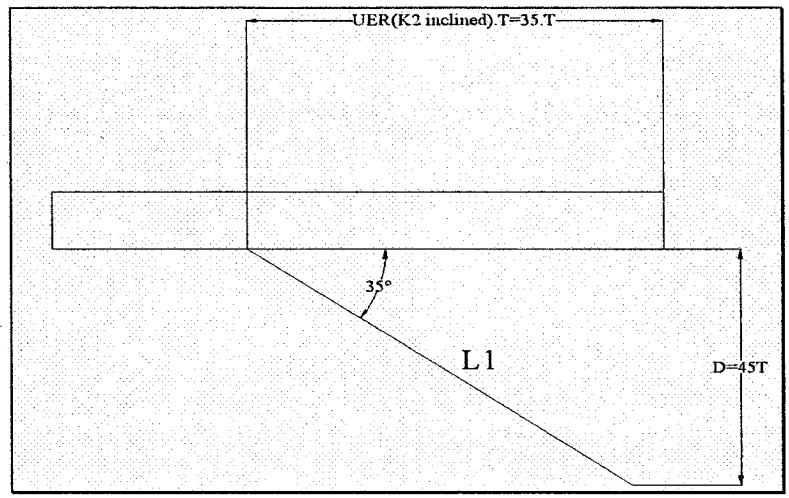

Figure A-28. Theoretical schematic of the facets for design 5 for Si {110} in 25% and 19% TMAH (δ=9.74°)

The experimental results for δ=12° on 25% TMAH [37] are shown in figure A-29. These results show that the exposed facets are the same as what have been expected with the analytical results for the first 30 minutes of etching time but after a long etching time the exposed facets from the left side of the mask reached to the right side and finally the exposed facets produce a groove shape. But the theoretical results are in good agreement with the experimental results.

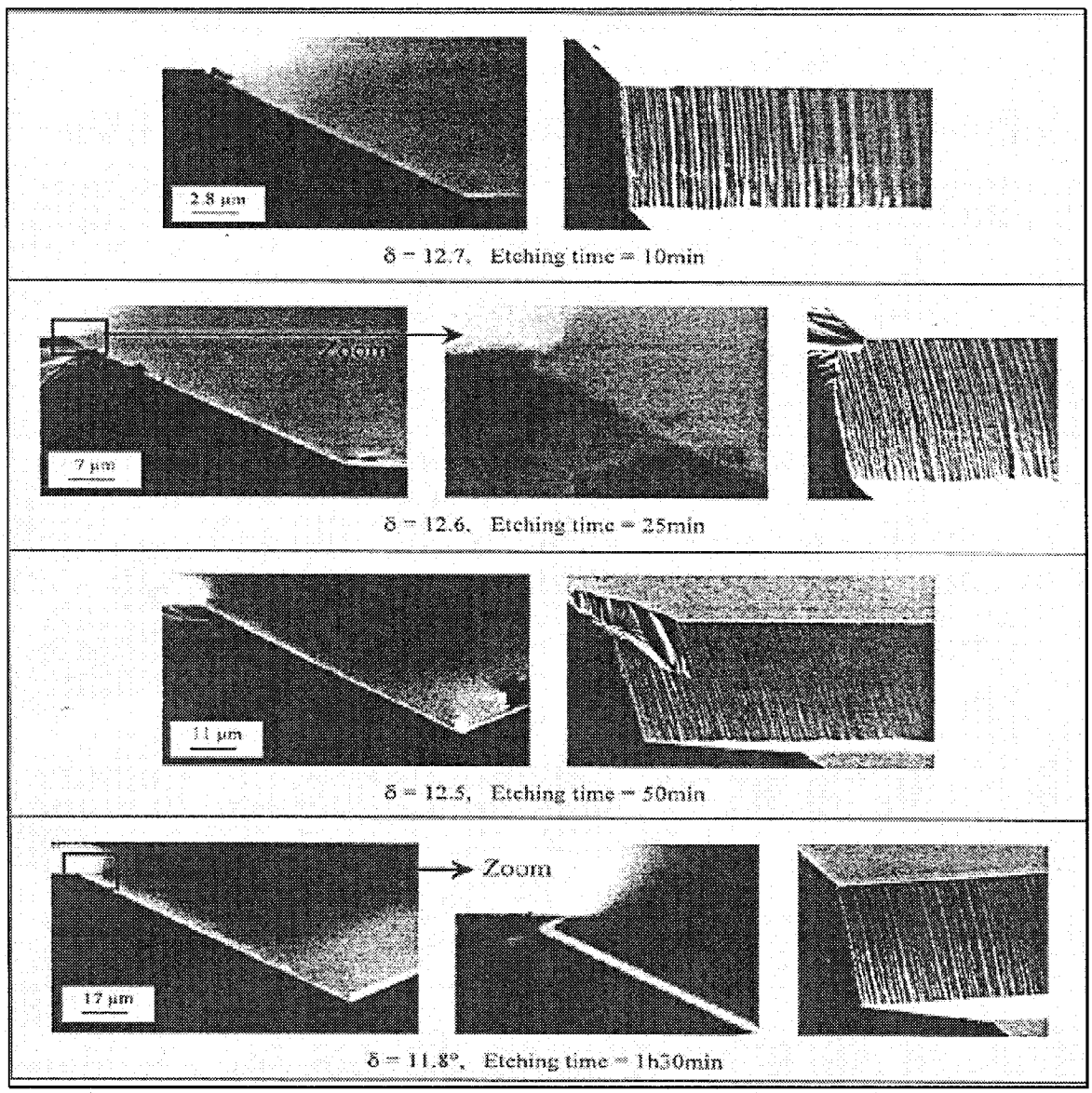

Figure A-29. Real schematic of the facets for one edge of design 5 for Si {110} in 25% TMAH (δ=12°) [37]

A.1.10. Design 6 for Si {110} on 25% and 19% TMAH

For this design the edges of square shape mask have deviation angles of 54.74°. The analytical results are similar to analytical results on part A.1.5 for 25% TMAH and A.1.6 for 19% TMAH.

The exposed facets for this design in 25%TMAH are similar to the situation that have been described before in part A.1.5 for δ=54.74° (figure A-20). From the theoretical results of this design it can be seen that on the edges of the mask, vertical facets should be exposed. But in accordance with the previous experimental works [38] [39] [40], on two corners of each rectangular cavity in the mask the35.26° inclined {111} family planes will be exposed at the same time with the vertical {111} family planes. This is because of geometrical considerations of concave shape masks that tend to expose slowest-etching planes [41], which for this situation the {111} family plane are the slowest-etching planes. The shape of these types of cavities is illustrated in figure A-30.

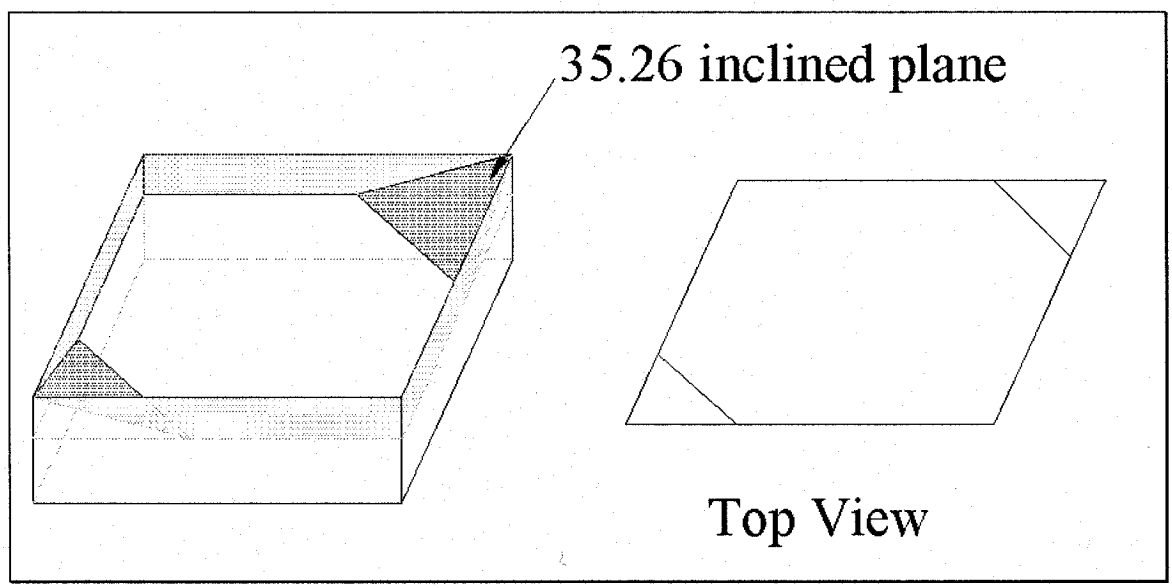

Figure A-30. Real schematic of the facets in each cavity for design 6 for Si {110} in 25% and 19% TMAH [37]

And the shape of each fabricated pin will be so complicated after etching in 25% and 19% TMAH. It means that except the vertical facets on the edges of the pins the35.26° inclined facets are exposed on the corners of the pins. For the gaps between the cavities on the mask the under-etching time of {111} planes is the important item to estimate the width of the gaps.

A.2. Summary

It can be concluded that:

- Designs 1, 3 and 5 are not an acceptable design, because vertical facets are not finally exposed.
- In design 2 and 4 fast etch planes are accompanying the vertical exposed facets, which are unnecessary facets and made it much difficult to fabricate a square pin.
- In design 6 is not an acceptable design, because of 35.26° inclined facets in each corner accompanying the vertical exposed facets in all sides of the mask.
- By using second design for Si {100} and the forth design for Si {110} on 25% and 19% TMAH there is a miniature ability to fabricate vertical pins with high aspect ratio (depends on the etching time) but these pins do not have uniform vertical walls after all the process.

Appendix B

Evaluation of the Performance of the Proposed Micro Heat Exchanger versus Standard Convective Surfaces

B.1. Evaluation

In this part the performance of the proposed micro heat exchanger is compared with the same surface without any pin arrays on it. This surface was modeled in ANSYS and same boundary conditions that were considered for the proposed design (table 4-2) were applied on this surface to see that how much would be the total transferred heat flux from this surface to the flowing fluid (17°C air).

Figure B-1 shows the amount of transferred heat flux for both pined surface and unpinned surface at different temperatures for the base.

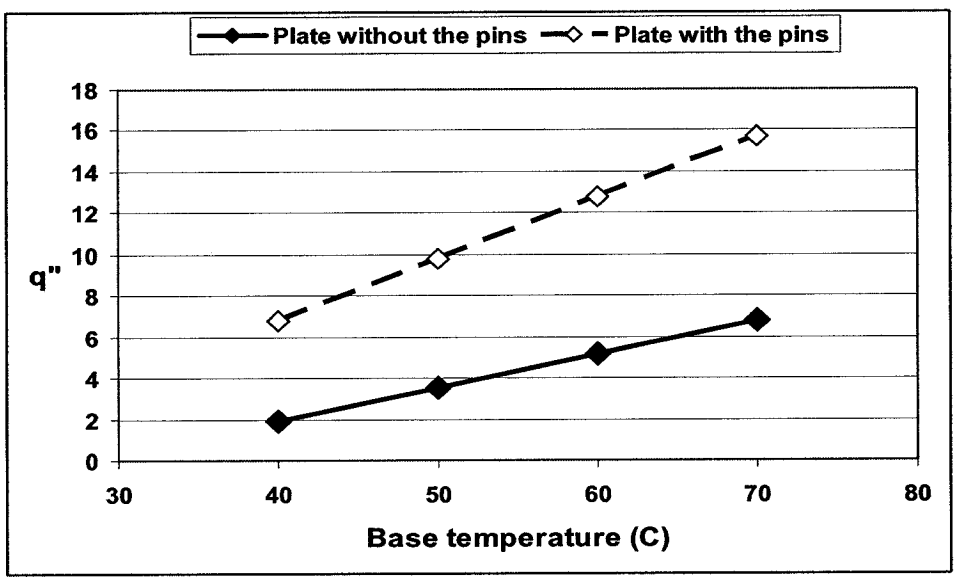

Figure B-1. The amount of total transferred heat flux from the pinned and unpinned surface for the proposed micro heat exchanger

Also figure B-2 shows the variation of the normalized heat flux ratio O versus different base temperatures. In this figure, O is defined by equation B-1:

$$\Omega = \frac{q''_{pined} - q''}{q''} \qquad \text{(B-1)}$$

In this equation, O is the normalized heat flux ratio, q''_{pined} (W/m²) is the total heat flux from the pined surface of the proposed design and q'' (W/ m²) is the total heat flux from the surface of the proposed design without the pins.

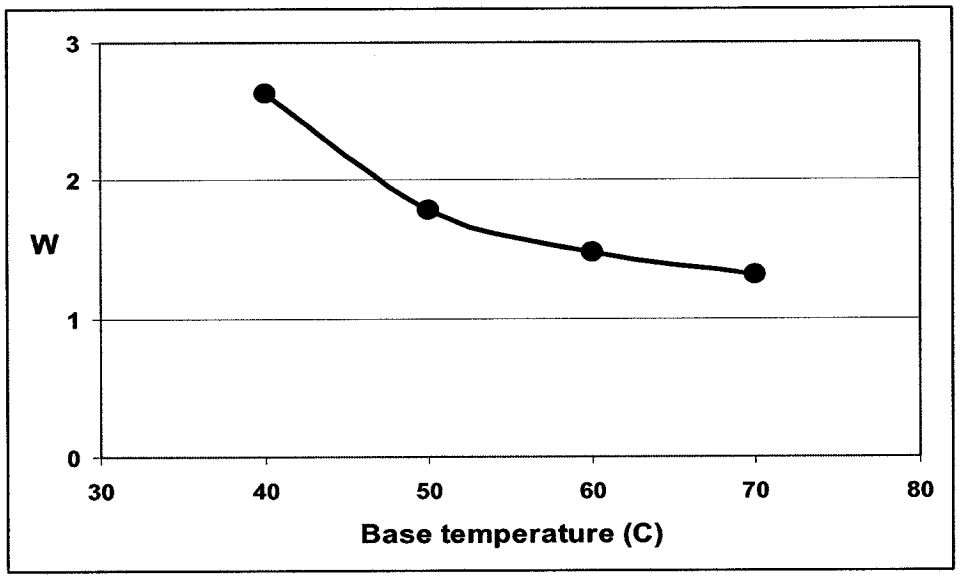

Figure B-2. The normalized heat flux ratio O versus base temperature

It is clearly seen that:

- The pinned surface has more heat flux transformation than the unpinned surface.
- By increasing the base temperature the amount of total heat flux is increasing for both pinned and unpinned surfaces.

- The amount of normalized heat flux ratio is decreasing by increasing the base temperature.
- The amount of transferred heat flux from the pinned surface is 30% to 150% larger than the unpinned surface.

B.2. Summary

It can be concluded that:

- The proposed micro heat exchanger has better performance versus standard convective surfaces and it can transfer 30% to 150% higher heat flux to the flowing fluid.

Appendix C

A Sample Modeling in ANSYS

```
/PREP7
RECTNG,-3.75e-6,3.75e-6,-5e-6,5e-6,                    (Building The Model)
K,5,-3.535e-6,0,0,
K,6,0,-3.535e-6,0,
K,7,3.535e-6,0,0,
K,8,0,3.535e-6,0,
FLST,2,4,3
FITEM,2,5
FITEM,2,6
FITEM,2,7
FITEM,2,8
A,P51X
/VIEW,1,1,2,3
/ANG,1
/REP,FAST
/VIEW,1,1,1,1
/ANG,1
/REP,FAST
VOFFST,1,-375e-6, ,
VOFFST,2,-80e-6, ,
VOFFST,2,8e-005, ,
```

```
VDELE,     2, , ,1
VPLOT
FLST,2,2,6,ORDE,2
FITEM,2,1
FITEM,2,3
VGLUE,P51X                                          (Gluing the Volumes)
/NOPR
/PMETH,OFF,0
KEYW,PR_SET,1
KEYW,PR_STRUC,0
KEYW,PR_THERM,1
KEYW,PR_FLUID,0
KEYW,PR_ELMAG,0
KEYW,MAGNOD,0
KEYW,MAGEDG,0
KEYW,MAGHFE,0
KEYW,MAGELC,0
KEYW,PR_MULTI,0
KEYW,PR_CFD,0
/GO
/COM,          /COM,Preferences for GUI filtering have been set to display:
/COM,  Thermal
ET,1,SOLID87                                        (Selecting Element Type)
```

```
TOFFST,273
MPTEMP,,,,,,,,
MPTEMP,1,0
MPDATA,KXX,1,,150          (Applying Thermal Conductivity of Silicon)
SMRT,6                     (Meshing the model)
MSHAPE,1,3D
MSHKEY,0
FLST,5,2,6,ORDE,2
FITEM,5,2
FITEM,5,4
CM,_Y,VOLU
VSEL, , , ,P51X
CM,_Y1,VOLU
CHKMSH,'VOLU'
CMSEL,S,_Y
VMESH,_Y1
CMDELE,_Y
CMDELE,_Y1
CMDELE,_Y2
FINISH
/SOL
FLST,2,1,5,ORDE,1
FITEM,2,3
```

```
/GO
DA,P51X,TEMP,40,1                    (Applying Boundary Conditions)
/DIST,1,0.729,1
/REP,FAST
/FOC,1,-0.3,,,1
/REP,FAST
/FOC,1,,-0.3,,1
/REP,FAST
/FOC,1,-0.3,,,1
/REP,FAST
/FOC,1,,-0.3,,1
/REP,FAST
/DIST,1,0.729,1
/REP,FAST
/VIEW,1,1,2,3
/ANG,1
/REP,FAST
/DIST,1,0.729,1
/REP,FAST
FLST,2,9,5,ORDE,2
FITEM,2,9
FITEM,2,-17
/GO
```

```
SFA,P51X, ,CONV,4965,28.5          (Applying Convection Boundary Conditions)
/STATUS,SOLU
SOLVE                              (Solving the problem)
/DIST,1,1.37174211248,1
/REP,FAST
/DIST,1,1.37174211248,1
/REP,FAST
/DIST,1,1.37174211248,1
/REP,FAST
/FOC,1,,0.3,,1
/REP,FAST
/DIST,1,1.37174211248,1
/REP,FAST
FINISH
/POST1
/EFACE,1
PLNSOL,TEMP, ,0,                   (Ploting the themperature distribution)
/VIEW,1,-1
/ANG,1
/REP,FAST
/VIEW,1,,-1
/ANG,1
/REP,FAST
```

```
/VIEW,1,-1
/ANG,1
/REP,FAST
/VIEW,1,,,-1
/ANG,1
/REP,FAST
/VIEW,1,,1
/ANG,1
/REP,FAST
/VIEW,1,1
/ANG,1
/REP,FAST
/DIST,1,0.729,1
/REP,FAST
/EFACE,1
PLNSOL,TF,Z,0,
/VIEW,1,1,2,3
/ANG,1
/REP,FAST
PATH,t,2,30,20,                    (Selecting A Path for Printing the results)
PPATH,1,0,0,0,-375e-6,0,
PPATH,2,0,0,0,80e-6,0,
PDEF,tfz,TF,Z,AVG
```

/PBC,PATH, ,0

PRPATH,TFZ (Showing the Results of Thermal heat flux through the model)